Universidad de Málaga

Escuela Técnica Superior de Ingeniería de Telecomunicación

E.T.S. DE INGENIERÍA DE
TELECOMUNICACIÓN
UNIVERSIDAD DE MÁLAGA

UNIVERSIDAD DE MÁLAGA

Programa de Doctorado en Ingeniería de Telecomunicación

TESIS DOCTORAL

Characterization techniques for microwave and millimeter-wave circuit design using additive manufacturing and multiconductor transmission lines

Autor:

Mario Pérez Escribano

Director:

Enrique Márquez Segura

Málaga, 2022

DECLARACIÓN DE AUTORÍA Y ORIGINALIDAD DE LA TESIS PRESENTADA PARA OBTENER EL TÍTULO DE DOCTOR

D./Dña MARIO PÉREZ ESCRIBANO

Estudiante del programa de doctorado EN INGENIERÍA DE TELECOMUNICACIÓN de la Universidad de Málaga, autor/a de la tesis, presentada para la obtención del título de doctor por la Universidad de Málaga, titulada: CHARACTERIZATION TECHNIQUES FOR MICROWAVE AND MILLIMETER-WAVE CIRCUIT DESIGN USING ADDITIVE MANUFACTURING AND MULTICONDUCTOR TRANSMISSION LINE.
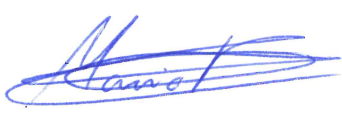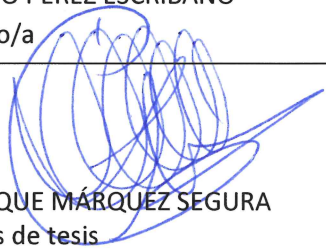
Realizada bajo la tutorización de ENRIQUE MÁRQUEZ SEGURA y dirección de ENRIQUE MÁRQUEZ SEGURA (si tuviera varios directores deberá hacer constar el nombre de todos)

DECLARO QUE:

La tesis presentada es una obra original que no infringe los derechos de propiedad intelectual ni los derechos de propiedad industrial u otros, conforme al ordenamiento jurídico vigente (Real Decreto Legislativo 1/1996, de 12 de abril, por el que se aprueba el texto refundido de la Ley de Propiedad Intelectual, regularizando, aclarando y armonizando las disposiciones legales vigentes sobre la materia), modificado por la Ley 2/2019, de 1 de marzo.

Igualmente asumo, ante a la Universidad de Málaga y ante cualquier otra instancia, la responsabilidad que pudiera derivarse en caso de plagio de contenidos en la tesis presentada, conforme al ordenamiento jurídico vigente.

En Málaga, a 4 de MARZO de 2022.

Fdo.: MARIO PÉREZ ESCRIBANO
Doctorando/a

Fdo.: ENRIQUE MÁRQUEZ SEGURA
Tutor/a

Fdo.: ENRIQUE MÁRQUEZ SEGURA
Director/es de tesis

Yo, Enrique Márquez Segura, con DNI 33380994J, tutor y director de la tesis titulada "Characterization techniques for microwave and millimeter-wave circuit design using additive manufacturing and multiconductor transmission lines", realizada por el estudiante del programa de doctorado en Ingeniería de Telecomunicación Mario Pérez Escribano, con DNI 26047015K, autorizo la lectura de dicha tesis doctoral.

De igual forma, confirmo que las publicaciones que avalan esta tesis, las cuales se pueden consultar en el Apéndice D de esta memoria, no han sido utilizadas en tesis anteriores.

En Málaga, a 4 de marzo de 2022.

Fdo. Enrique Márquez Segura
Director y tutor de tesis

EFQM AENOR

ISO 14001
BUREAU VERITAS
Certification

bq
bequal

Edificio Pabellón de Gobierno. Campus El Ejido. 29071
Tel.: 952 13 10 28 / 952 13 14 61 / 952 13 71 10
E-mail: doctorado@uma.es

To Elenita, Santi, María, and Pablito.
Thank you for trusting me,
for always supporting me,
and for helping me get here.
I love you.

Mario

Nobody said it was easy.

--- *The Scientist (Coldplay)*

Acknowledgements

First of all, my most sincere gratitude to my supervisor Enrique Márquez Segura for his considerable support, his attention from day one, and for trusting me. It would have been impossible to get here without his help. It has been an absolute pleasure to work with him and learn from him since the day we met, ten years ago.

I want to express my gratitude to Juan José Sánchez Martínez for his help in work related to Multiconductor Transmission Lines. In addition, I would like to thank Elena Abdo Sánchez, Javier Mata Contreras, Teresa Martín Guerrero, and Carlos Camacho Peñalosa for their availability to solve any questions that may arise. I want to thank also José Vicente Siles Pérez, my supervisor during my stay at Jet Propulsion Laboratory, for his kindness and good work. Finally, I would like to mention my cousin, Mar Vaquero, for her grammar corrections to articles written in English.

Last but not least, I would like to dedicate this paragraph to all my colleagues, especially those who have shared good times with me during our time in ETSIT: José Técnico, Alberto, Aarón, Pablo M., Fran, Lorena, Ana, Carlos, Luis, Juanlu, Joaquín, Carolina, Nuria, Pablo C., Pedro, among others. Furthermore, I would like to thank my family (and 'astros') for their help, patience, and love. Especially Elena, my better half, for being there every day. Thank you.

Abstract

In this Ph.D. thesis, transmission line characterization techniques have been studied. It is possible to estimate the propagation constant of transmission from 2-port S-parameters measurements of two different length transmission lines. An error analysis, which includes various error sources, is performed for these characterization techniques to study the causes that provoke inaccuracies in the estimation. Based on this analysis, several ways to improve the researched methods' performance and bandwidth are proposed. Subsequently, these methods are used for two purposes: on the one hand, to characterize the electromagnetic properties of materials made by additive manufacturing. On the other hand, to characterize the propagation constant of the even and odd modes of coupled microstrip lines, using pure-mode S-parameters. Finally, a particular case of coupled lines, such as multiconductor transmission lines with interconnected alternate lines, are used to synthesize dual-band and multi-band bandpass filter responses. All the circuits and methods proposed in this thesis have been validated by means of experimental work, which shows an excellent agreement between analytical expressions, simulations, and measurements. This fact proves the reliability of the presented work.

Contents

List of Acronyms

AM	Additive Manufacturing
ABS	Acrylonitrile Butadiene Styrene
BPF	Bandpass filter
BPFs	Bandpass filters
CPE	Copolyester
EM	Electromagnetic
FBW	Fractional Bandwidth
FDM	Fused Deposition Modeling
HIPS	High Impact Polystyrene
LMS	Least-Mean-Square
LS	Least-Square
LUT	Line Under Test
MIMO	Multiple-input Multiple-output
MTL	Multiconductor Transmission Line
MTLs	Multiconductor Transmission Lines
PETG	Polyethylene Terephthalate Glycol
PLA	Polylactic Acid
PMVNA	Pure-Mode Vector Network Analyzer
RF	Radio Frequency
SOLT	Short-Open-Load-Through
TEM	Transverse Electromagnetic
TL	Transmission Line

TLs	Transmission Lines
TPU	Thermoplastic Polyurethane
TRL	Through-Reflect-Line
UWB	Ultra Wide Band
VNA	Vector Network Analyzer
VNAs	Vector Network Analyzers

List of Figures

XVIII

XIX

Chapter 1

Introduction

The aim of this introductory chapter is to summarize the topic of this dissertation. Section 1.1 describes the contextual framework of the work. The origins that have led to starting this research are presented in Section 1.2. Later, the main objectives to be reached in this thesis are summarized in Section 1.3. Lastly, a brief overview of the structure, along with the main contributions of each of the chapters that make up this Ph.D. thesis, are described in Section 1.4.

1.1   Contextual framework

The world has been undergoing significant changes that have affected our lifestyle in recent years. The current trend in society is to bring all world places closer together, either physically or virtually connected. Thus, advances in mobility must be accompanied by advances in communication technologies. These communications must be accessible to everyone, regardless of the place or the economic status. For this reason, specific changes must be produced, mainly when they affect communication systems.

Beyond the globalization of communications, systems are becoming increasingly complex, and their requirements are growing exponentially. When the implementation of the so named fifth generation of mobile communications networks (5G) is still beginning, there are studies already paying attention to the needs of the sixth generation networks [1]. The main requirement of new networks is a considerable bit rate increase. It is expected that in 6G, rates of 1 Tb/s can be reached. In the field of Radio Frequency (RF), which is the central theme of this thesis, an increase in bit rate

turns into a considerable increase in bandwidth. There is no choice but to use higher frequencies to achieve these new limits. For example, 5G systems have applications in the E-band (60 GHz). Beyond, 6G systems are expected to use the THz bands (below 300 GHz), including mm-waves for mobile access. This is just an example of how communications systems, bandwidth, and specifications will exponentially grow in the near future.

These new requirements are accompanied by functionalities, such as low cost, broad bandwidths, lightweight, easiness of manufacture, or easy integration, that must be fulfilled by a system to be commercialized. In this sense, new materials and manufacturing techniques used in communication systems constantly arise. Facing the arrival of these new materials, it is fundamental to have a precise characterization of their properties to use them for implementing structures such as transmission lines, waveguides, filters, or antennas, among other communication subsystems in this new scenario.

One of the problems designers have to deal with is knowing the electromagnetic behavior of structures and substrates used to implement new devices. In this sense, characterization techniques are necessary for microwave circuit design with high demanding specifications, as broadband directional couplers and filters. That is why, since the 1960s, methods for the characterization of the propagation constant of Transmission Lines (TLs) have been proposed and improved. The first techniques were based on the use of reflectometers [2]. Later, in 1975, Bianco and Parodi proposed a method for the estimation of the propagation constant [3] based on the measurement of the reflection coefficient at the input of four equally terminated transmission lines of different lengths. This idea, as well as variations that include transmission measurements, have been used in numerous studies to characterize the propagation constant [4,5]. In addition, several statistical improvements have been proposed, which are usually based on increasing the number of lengths to be measured [6].

Returning to new materials and manufacturing techniques, in recent years, Additive Manufacturing (AM) techniques have stood out in many scientific fields. Concretely, in the microwave and mm-wave areas, devices such as TLs [7] or antennas [8] have been manufactured using 3D printing technologies. One of the significant advantages is the possibility of synthesizing different relative permittivities using the same material, just varying the printing infill, which will determine the amount of air that remains inside the printed structure [9]. However, these materials are not specifically designed for implementing RF devices. For this reason, it is necessary to look for accurate

characterization techniques that allow obtaining the Electromagnetic (EM) material parameters in broadband. One possible option is to carry out a direct measurement of the materials, such as the one proposed in [10]. Another option is the use of indirect measures that make use of Vector Network Analyzers (VNAs), like the one in [11].

Another option to focus on to improve the performance of the devices is to increase the number of conductors. With this configuration, much more selective responses, greater bandwidths, or differential devices [12] can be achieved. However, it is essential to accurately characterize the modes that propagate through a coupled line structure. That is why characterization methods have also been used to obtain the propagation constants and impedances of a pair of coupled lines [13]. When using more than two lines, the structure is usually called Multiconductor Transmission Lines (MTLs). Using this topology, the design feasibility increases. In [14], authors proposed a Multiconductor Transmission Line (MTL) with interconnected alternate lines, used to eliminate undesired resonances in the traditional interdigital capacitor. Authors called it wire-bonded interdigital capacitor. An analytical model of that circuit, for an even number of lines, was presented in [15], whereas a generalized model was analyzed in [16]. In this sense, authors demonstrated that MTLs are suitable for designing or improving the performance of microwave circuits, since a great range of coupling factors and impedances can be achieved, and there is an analytical model that allows manipulating the structure even without EM simulations. Using MTLs with interconnected alternate lines, devices such as phase shifters [17], baluns [18], stubs [19] or quasi-elliptic filters [20] were proposed by J. J. Sánchez-Martínez and E. Márquez-Segura.

1.2   Genesis

The core of this Ph.D. thesis emerged in the context of a research project whose main objective was to explore new manufacturing techniques for microwave and millimeter-wave devices. In this sense, our research laboratory is equipped with 2D (Fujifilm Dimatix DMP-2850) and 3D (Ultimaker 3) additive manufacturing capabilities. However, little prior research had been carried out, so one of the starting points was to get the manufacturing equipment up and running.

When the first devices began to be developed, we realized that the first step should be knowing and characterizing the EM properties of the materials that we had available in the laboratory. That is why research began on methods for estimating the propagation constant that would allow us to characterize the fabricated structures. Therefore, it

was decided to choose methods based on the one proposed by Bianco and Parodi [3] since our research group had previous experience in this kind of methods.

On the other hand, based on the excellent results obtained in the Ph.D. thesis of J. J. Sánchez-Martínez, the use of MTLs with alternate interconnected lines for the realization of microwave circuits was proposed. That is why it was also decided to follow this research line, developing new devices that use the analytical models previously created in the research group. The idea is that, in the future, MTL devices can be manufactured using additive manufacturing technologies.

1.3   Objectives

As described in the previous sections, characterization of the propagation constant is extremely important for the design of microwave and mm-wave devices. Furthermore, this characterization is essential when the properties of the substrates used are unknown since these properties must be used to perform EM simulations. Considering the robustness of the methods for estimating the propagation constant, it will be the starting point of this Ph.D. thesis.

In this context, the first goal of this work is to study and compare several methods and possible random error sources and propose improvements that allow achieving more accuracy when applying those methods. Subsequently, these methods will be used to characterize novel materials made by AM and MTL structures. Finally, these MTLs will be the structure provided to develop new filter topologies for synthesizing dual-band and multi-band responses, always providing a model that allows performing analytical designs without any optimization. All the presented theories will be assessed with experimental work.

1.4   Thesis outline and contributions

This section explains the thesis outline, including a brief description that highlights the main contributions of each chapter.

Chapter 2 begins with a description of three methods traditionally used to characterize the propagation constant of TLs. These methods are based on the one proposed by Bianco and Parodi in [3], taking 2-port S-parameters measurements of two lines with different lengths. An error analysis is applied to these methods, which includes

four possible sources of random errors: Vector Network Analyzer (VNA), line length, connector repeatability, and substrate non-homogeneity. Subsequently, a statistical improvement based on a Least-Mean-Square (LMS) estimator is proposed, consisting of increasing the number of lines to be measured. Using this improvement, it is possible to reduce the variance of the obtained propagation constant. The main contribution of this chapter is the demonstration that the eigenvalue-based strategy is the least affected by random errors.

Once the methods have been presented, in **Chapter 3**, they are applied to a microstrip line loaded with a piece of some AM materials. Subsequently, an estimation of the propagation constant of the complete structure is obtained. In this case, that constant will be affected by the EM properties (relative permittivity and loss tangent) of the top substrate. However, knowing the height of both substrates and the lower relative permittivity, it is possible to get an indirect fairly accurate approximation of the properties of the upper material. Several material samples are fabricated to validate the presented modified method. The main contribution of this chapter is proposing HIPS as an excellent material to build structures such as circuits or antennas.

In **Chapter 4**, the proposed improved method is applied to a pair of symmetrical coupled microstrip lines. In this case, instead of measuring S-parameters in single-ended mode, they are measured in pure-mode, creating two virtual common and differential ports. Using this type of measurement, it is possible to separately excite the even and odd modes of the structure and extract the S-parameters corresponding to each mode. Later, these matrices are considered as an equivalent 2-port Transmission Line (TL), to which the proposed method will be applied. The main contribution of this chapter is having demonstrated that reducing the angle of the bends in the feeding lines is a simple way to improve the estimation of the propagation constant considerably since bend radiation strongly limits the bandwidth of the obtained attenuation and phase constants.

Chapter 5 introduces three different topologies to effortlessly design dual-band and multi-band Bandpass filters (BPFs), using short-circuited wire-bonded MTLs and shunt open stubs. Using the first two configurations, it is possible to synthesize Chebyshev filtering functions to obtain narrow and moderate broad bandwidths. The third one consists of increasing the number of stubs to achieve multi-band bandpass responses. Results of the manufactured prototypes show an excellent agreement with the proposed analytical model. Therefore, the main contribution of this chapter is having proposed a novel topology and its analytical model to design multi-band BPFs without any

optimization or EM simulation performed, just using the proposed set of closed-form design equations.

Finally, **Chapter 6** summarizes the main results and highlights the most important contributions achieved in every chapter of this Ph.D. thesis. It concludes with the proposal for guidelines to carry on with this work in the future.

In addition, three appendices are included to expand provided contents. Appendix A shows the influence of conductivity in the proposed methods for the estimation of the propagation constant. The effect is demonstrated to be similar to the one provoked by line length errors. Appendix B shows the mathematical development carried out to obtain the filtering functions of the first prototype of Chapter 5. Appendix C describes the analytical solution to a general quartic equation and then applies it to the filtering function of the second filter prototype presented in Chapter 5. The publications derived from this thesis are enumerated in Appendix D. Lastly, Appendix E contains a summary of this Ph.D. thesis in Spanish.

Chapter 2

Characterization of the Propagation Constant Using 2-Port Measurements and Its Error Sources

In this chapter, a comparison between three broadband methods used to estimate the propagation constant (γ) of planar TLs is presented. The objective is to use these methods for the future characterization of materials. This comparison aims to study how possible random measurement errors can affect the use of the aforementioned methods commonly used since under ideal conditions, the same solution is obtained from all of them. For this purpose, a sensitivity analysis is carried out to study the similarities and differences and how errors in measured S-parameters, line lengths, connector repeatability, and substrate non-homogeneity affect the attenuation (α) and the phase (β) constant obtained from each method. Subsequently, a minimization approach that consists of a Least-Square (LS) estimation using a criterion to choose the optimal line lengths is proposed to minimize measurement errors. Finally, two experiments have been designed, manufactured using microstrip TLs, and measured to validate the developed theory. Results corroborate the proposed idea and show an excellent agreement with EM simulations, therefore assessing the suitability of the proposed error analysis. Furthermore, higher accuracy is obtained when using the same pair of connectors, considerably reducing the attenuation constant ripple, which shows that it is an appropriate procedure to reduce the uncertainty of the final estimation significantly.

2.1   Introduction

The experimental determination of the propagation constant ($\gamma = \alpha + j\beta$) of planar TLs is crucial in the design of microwave and millimeter-wave circuits. In recent years, the imminent arrival of new materials, such as printed materials used to manufacture microwave circuits, several studies have been based on the measurement of the propagation constant to extract the EM properties of these materials [10, 21, 22]. The methods available to obtain the propagation constant can be classified into several categories depending on the sort of measurements considered [23]. The first possible classification distinguishes between broadband [3] and resonant methods [24]. On the one hand, the former methods characterize the propagation constant in a wide range of frequency points measured. Their main drawback can be the accuracy, which depends on the precision of the measurements, showing a worse behavior, precisely, at resonances. On the other hand, resonant methods allow an accurate estimation of the propagation constant in a discrete set of frequency points, those where a resonance on the test structure occurs. However, they cannot be useful when broadband characterization is required. From another point of view, another classification distinguishes between 1-port [25], and 2-port [26, 27] measurements.

This chapter deals precisely with 2-port measurement methods for general TLs. The propagation constant can be obtained, e.g., as a result of a Through-Reflect-Line (TRL) calibration using two lines or more lines of different lengths [4, 28, 29]. Nevertheless, resonances due to those length differences can degrade the obtained results. In this sense, several works have proposed improvements by increasing the number of lines, as in [30]. This strategy was used to define the multiline TRL calibration [29]. For this reason, an overdetermination based on applying traditional methods and increasing the number of lines, and properly choosing the length of the TLs is proposed in this chapter.

As the aforementioned TRL method, there are different techniques based on invariant two-port [4, 31] that, in a first look, bear a strong resemblance between them. These several techniques for measuring the propagation constant have been examined, showing that ideally, they are similar, but their behavior is entirely different in the presence of measurement errors. In this chapter, the interface between the VNA and the outer is a coaxial port, so some fixture between that terminal and the Line Under Test (LUT) must be included. The fixture produces a discontinuity in the signal path that strongly affects the measurement. The concept of algebraic invariant of networks in linear embedding

is a standard tool in the theory of linear active and non-reciprocal networks [32]. The use of a mathematical invariant allows the extraction of the effects of the test fixture from the parameter estimated. This fact means that, in general, no VNA calibration is necessary when using at least two TLs measurements. This chapter deals with three different formulations for broadband methods using 2-port S-parameters. The main focus is on methods that use the invariant properties of similar matrix transformations. These methods avoid the systematic errors of other measurement techniques due to mismatching between the characteristic impedance of the VNA and the LUT using mathematical invariants. However, this behavior strongly differs from the ideal case in the presence of random errors.

Methods based on the invariant concept [32] assume that the transition is the same in all measurements. However, this statement is not entirely true since connector repeatability is not wholly assured in a real setting. In this sense, in [5], authors demonstrated that results could be significantly better if special attention is paid to the repeatability of the launcher, as they used a destructive method that cut the TLs but kept the same connectors throughout the whole characterization process. In [33], authors identified that half-wavelength errors in TL calibrations are, in part, due to fixture inconsistencies. Regarding connector repeatability, stochastic models can be used to study their behavior [34--37], modeling each possible perturbation as an equivalent two-port circuit. Repeatability tends to have more variance at high frequencies and affects phase notably, more than the magnitude of the measured S-parameters.

A study on how random errors affect broadband methods for the characterization of the propagation constant of TLs has been carried out. It is based on two-port measurements of TLs, and it is required the use of a two-port VNA with no need of calibration. In this chapter, four error sources will be considered. They can be classified into three groups: VNA and line lengths errors, connector repeatability errors, and errors due to non-homogeneity of the structure, mainly due to conductivity. The first two groups will be studied in this chapter, while the last one will be reviewed in Appendix A.

This chapter is structured as follows. The three methods to be analyzed are described in Section 2.2. To study how random errors affect each of the methods, a sensitivity analysis has been performed, and the results are summarized in Section 2.3. Section 2.4 shows a technique to minimize errors, based on the overdetermination of the methods using a LS estimation. Connector repeatability errors are deeply studied in Section 2.5 The developed theory is corroborated through real measurements in Section 2.6. Finally,

conclusions are given in Section 2.7.

2.2   Description of the methods
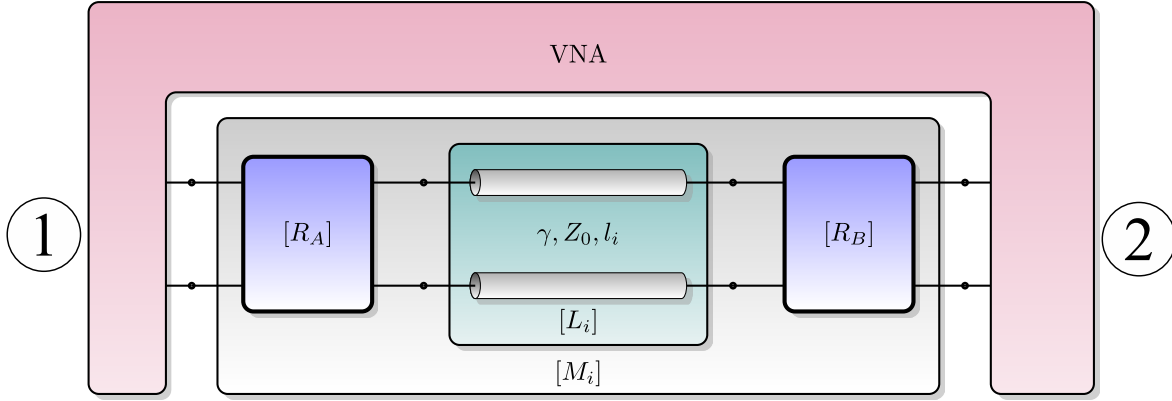
Figure 2.1: Cascade connection diagram of different two-port circuits involved in the transmission line T-parameters measurement using a Vector Network Analyzer.

The methods treated in this chapter use a measurement setup as shown in Fig. 2.1. The two-port S-parameters of two lines with different lengths are measured, and the transmission parameters matrices, $[M_1]$ and $[M_2]$, are calculated. The transmission matrices can be obtained easily from the measured S-parameters using the following expressions [38]:

$$
\begin{aligned}
T_{11} &= \frac{1}{S_{21}} & T_{12} &= -\frac{S_{22}}{S_{21}} \\
T_{21} &= \frac{S_{11}}{S_{21}} & T_{22} &= \frac{S_{12}S_{21} - S_{11}S_{22}}{S_{21}}.
\end{aligned}
\tag{2.1}
$$

According to Fig. 2.1, the measured cascade matrices of the two lines of different lengths can be written as $[M_1] = [R_A][L_1][R_B]$ and $[M_2] = [R_A][L_2][R_B]$. The matrices $[L_1]$ and $[L_2]$ are the transmission matrix of the lines measured excluding the transition between ports and the LUT, whose effects are considered in matrices R_A and R_B. The L_i matrices for every line measured are given by

$$
[L_i] = \begin{bmatrix} e^{+\gamma l_i} & 0 \\ 0 & e^{-\gamma l_i} \end{bmatrix}.
\tag{2.2}
$$

2.2.1 Method 1

The measured matrices can be combined in the following way

$$[M_1][M_2]^{-1} = [R_A][L_1][L_2]^{-1}[R_A]^{-1}. \tag{2.3}$$

Equation (2.3) is an eigenvalue equation that can be rewritten as $[M] = [R_A][L][R_A]^{-1}$, where $[M] = [M_1][M_2]^{-1}$ and $[L] = [L_1][L_2]^{-1}$. $[M]$ and $[L]$ are similar matrices and, in consequence, their eigenvalues, traces and determinants coincide. As $[L]$ is a diagonal matrix, $[L] = \text{diag}(e^{+\gamma \Delta l}, e^{-\gamma \Delta l})$, its eigenvalues are $e^{-\gamma \Delta l}$ and $e^{+\gamma \Delta l}$, respectively, and its trace is $e^{-\gamma \Delta l} + e^{+\gamma \Delta l}$. These values are the same for $[M]$. In order to obtain the propagation constant, the invariants mentioned above can be used. At this point, the three methods that will be used to obtain the propagation constant must be defined. Due to that trace does not change under a similarity transformation, the following equality holds

$$\text{trace}([L]) = \text{trace}([M]) = e^{-\gamma \Delta l} + e^{+\gamma \Delta l}, \tag{2.4}$$

being $\Delta l = l_2 - l_1$. Therefore, the propagation constant can be calculated as

$$\gamma = \frac{1}{\Delta l} \cosh^{-1} \left(\frac{\text{trace}\left([M_1][M_2]^{-1}\right)}{2} \right). \tag{2.5}$$

2.2.2 Method 2

The eigenvalues of $[M]$ are identical to the eigenvalues of $[L]$. Therefore, if λ_1 and λ_2 are the eigenvalues of $[M]$, they must be equals to $e^{-\gamma \Delta l}$ and $e^{+\gamma \Delta l}$, respectively [39]. Solving these equations for γ, it is obtained

$$\gamma = \frac{1}{\Delta l} \ln \left(\frac{1}{\lambda_1} \right) = \frac{1}{\Delta l} \ln (\lambda_2). \tag{2.6}$$

In this case, two different values can be obtained for the propagation constant, and an average of the eigenvalues of $[M]$, $1/2 (1/\lambda_1 + \lambda_2)$, can be used to calculate γ, that is

$$\gamma = \frac{1}{\Delta l} \ln \left(\frac{1/\lambda_1 + \lambda_2}{2} \right). \tag{2.7}$$

The averaging is used because it is assumed that the structure is reciprocal, so that the errors will affect T_{11} and T_{22} equally.

2.2.3 Method 3

Starting again in a different way [31], the sum of the measured matrices, $[M_{1+2}] = [M_1] + [M_2]$, instead of the product, can be considered and expressed as

$$[M_{1+2}] = R_A \begin{pmatrix} e^{+\gamma l_1}\left(1 + e^{+\gamma \Delta l}\right) & 0 \\ 0 & e^{-\gamma l_1}\left(1 + e^{-\gamma \Delta l}\right) \end{pmatrix} R_B. \tag{2.8}$$

Taking the determinant of the resulting matrix in Eq. (2.8) and dividing it by the determinant of $[M_1]$, the result is

$$\begin{aligned} \frac{\det\left([M_{1+2}]\right)}{\det\left([M_1]\right)} &= \left(1 + e^{+\gamma \Delta l}\right)\left(1 + e^{-\gamma \Delta l}\right) \\ &= 1 + e^{+\gamma \Delta l} + e^{-\gamma \Delta l} + 1 = 2 + 2\cosh(\gamma \Delta l). \end{aligned} \tag{2.9}$$

From Eq. (2.9), the complex propagation constant can be obtained as

$$\gamma = \frac{1}{\Delta l} \cosh^{-1}\left(\frac{\det\left([M_{1+2}]\right)}{2\det\left([M_1]\right)} - 1\right). \tag{2.10}$$

2.2.4 Simplified equations using S-parameters

As seen in the developed equations, port effects (R_A and R_B) have been removed from the formulas. For this reason, the methods will work in the same way with or without VNA calibration. All these mathematical expressions can be rewritten as a function of the measured S-Parameters instead of T-parameters to fulfill the later sensitivity analysis. Taking $\delta^{(n)}$ as $S_{12}^{(n)}S_{21}^{(n)} - S_{11}^{(n)}S_{22}^{(n)}$ and $\chi = \delta^{(1)} + \delta^{(2)} + S_{11}^{(1)}S_{22}^{(2)} + S_{11}^{(2)}S_{22}^{(1)}$, being $S^{(n)}$ the S-parameter matrix of line n, these mathematical expressions are given by:

1. Method 1:

$$\gamma = \frac{1}{\Delta l}\cosh^{-1}\left(\frac{\chi}{2S_{21}^{(1)}S_{12}^{(2)}}\right). \tag{2.11}$$

2. Method 2:

$$\gamma = \frac{1}{\Delta l} \ln \left(\frac{\chi - \sqrt{\chi^2 + 4\left(S_{22}^{(2)} - S_{22}^{(1)}\right)\left(\delta^{(2)}S_{11}^{(1)} - \delta^{(1)}S_{11}^{(2)}\right)}}{4S_{21}^{(1)}S_{12}^{(2)}} + \right.$$
$$\left. + \frac{S_{21}^{(1)}S_{12}^{(2)}}{\chi + \sqrt{\chi^2 + 4\left(S_{22}^{(2)} - S_{22}^{(1)}\right)\left(\delta^{(2)}S_{11}^{(1)} - \delta^{(1)}S_{11}^{(2)}\right)}} \right). \tag{2.12}$$

3. Method 3:

$$\gamma = \frac{1}{\Delta l} \cosh^{-1} \left(\frac{\left(S_{21}^{(2)} + S_{21}^{(1)}\right)\left(\delta^{(1)}S_{21}^{(2)} + \delta^{(2)}S_{21}^{(1)}\right) +}{2\left(S_{21}^{(2)}\right)^2 S_{12}^{(1)}S_{21}^{(1)}} \right.$$
$$\left. + \frac{\left(S_{11}^{(1)}S_{21}^{(2)} + S_{11}^{(2)}S_{21}^{(1)}\right)\left(S_{22}^{(1)}S_{21}^{(2)} + S_{22}^{(2)}S_{21}^{(1)}\right) - 2\left(S_{21}^{(2)}\right)^2 S_{12}^{(1)}S_{21}^{(1)}}{2\left(S_{21}^{(2)}\right)^2 S_{12}^{(1)}S_{21}^{(1)}} \right). \tag{2.13}$$

However, these complex equations can be quite simplified in case $Z_0 = Z_c$, being Z_0 the port impedance and Z_c the characteristic impedance of the transmission line. This is because $S_{11}^{(n)}$ and $S_{22}^{(n)}$ can be taken as 0. Furthermore, as the lines are reciprocal devices, it must be fulfilled that $S_{21}^{(n)} = S_{12}^{(n)}$. Under these ideal conditions, Eqs. (2.11)-(2.13) can be reduced to:

1. Method 1:

$$\gamma = \frac{1}{\Delta l} \cosh^{-1} \left(\frac{\left(S_{21}^{(1)}\right)^2 + \left(S_{21}^{(2)}\right)^2}{2S_{21}^{(1)}S_{21}^{(2)}} \right). \tag{2.14}$$

2. Method 2:

$$\gamma = \frac{1}{\Delta l} \ln \left(\frac{S_{21}^{(2)}}{S_{21}^{(1)}} \right). \tag{2.15}$$

3. Method 3:

$$\gamma = \frac{1}{\Delta l} \cosh^{-1} \left(\frac{\left(S_{21}^{(1)} + S_{21}^{(2)}\right)^2}{2S_{21}^{(1)}S_{21}^{(2)}} - 1 \right). \tag{2.16}$$

These simplified expressions are more practical than general case equations. They will be used in the sensibility analysis to extract the variances of α and β as a function of the S-parameters variances.

In order to evaluate the behavior of these methods, a simulation of two lines using Rogers 4350B substrate has been performed, with 30 mil thickness, $\varepsilon_r = 3.66$ including its dispersive response [40], $\tan \delta = 0.0031$, and 17.5 μm thick copper metallization. The line width is set to 1.65 mm, to get a 50 Ω characteristic impedance, whereas the lengths are 10 and 35 mm respectively. Figure 2.2 shows the real and imaginary part of z_i, being z_i the argument of $\cosh^{-1}$ or ln of the proposed methods ($i = 1, 2, 3$ indicates the method). As it is seen, Methods 1 and 3 works in a similar way, as (2.14) and (2.16) are exactly the same if operated in the ideal case, whereas imaginary part of the argument of Method 2 is completely different.
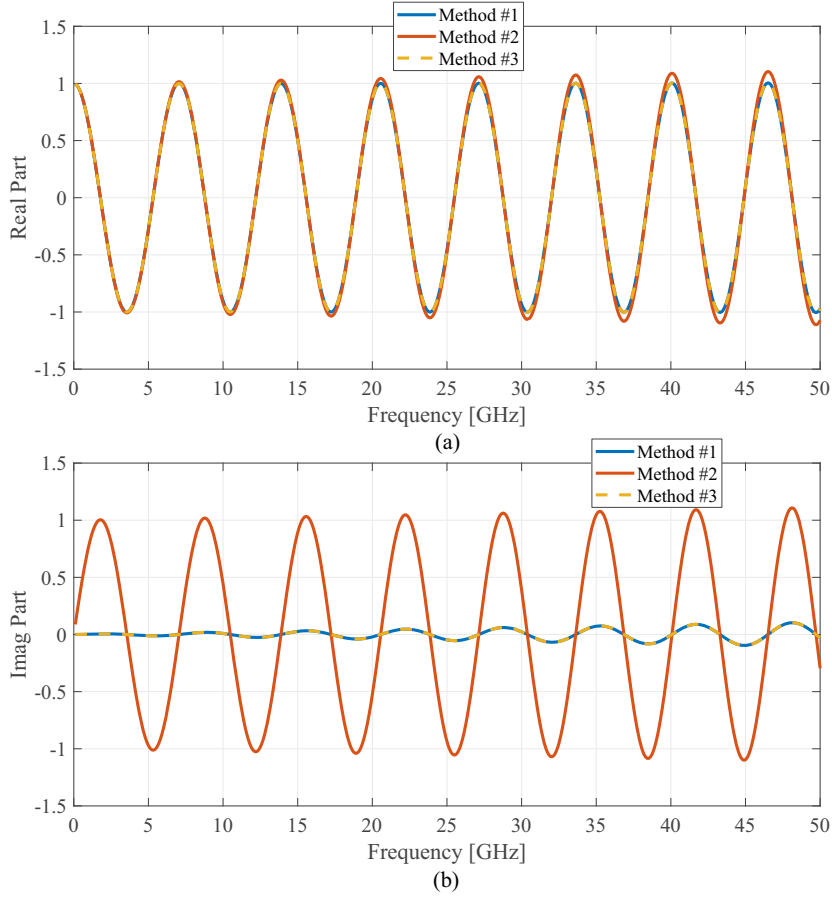
Figure 2.2: Real (a) and imaginary (b) parts of the argument of method functions.

It is important to consider that z_i, the argument of method functions, is a complex number defined as $z_i = r_i e^{j\theta_i}$. Function $\cosh^{-1}$ can be rewritten as a logarithmic function given by

$$\cosh^{-1}(z_i) = \ln(z_i + \sqrt{z_i - 1}\sqrt{z_i + 1}). \tag{2.17}$$

Therefore, for every method, the propagation constant can always be expressed as a

logarithmic function given by

$$\gamma = \frac{1}{\Delta l} \left[\ln(r_i) + j(\theta_i + 2n\pi) \right],$$ (2.18)

being

$$\alpha = \frac{1}{\Delta l} \ln(r_i),$$
$$\beta = \frac{1}{\Delta l}(\theta_i + 2n\pi).$$ (2.19)

In the context of a TL, r_i and θ_i are the attenuation and the electrical length of a line section of length Δl. At this point, it is essential to mention that the attenuation information depends exclusively on the absolute value of r_i, whereas β information is on θ_i. These expressions will be the starting point of the sensitivity analysis of the next section to know how random errors affect the propagation constant. It is noteworthy that α has a unique solution as $r \in R$ whereas β has an infinite number of solutions. This fact will play an important role in implementing the methods using numerical algorithms.

2.3   Sensitivity analysis to vector network analyzer and line lengths errors

For the first sensitivity analysis, two error sources are considered. They are errors in line lengths and in the argument of method functions. For this purpose, and looking for the covariance of α and β, the derivatives of (2.19) with respect to r, θ and Δl can

be expressed as

$$
\begin{aligned}
\frac{\partial \alpha}{\partial r} &= \frac{1}{r\Delta l} \\
\frac{\partial \alpha}{\partial \theta} &= 0 \\
\frac{\partial \alpha}{\partial \Delta l} &= -\frac{\ln(r)}{\Delta l^2} = -\frac{\alpha}{\Delta l} \\
\frac{\partial \beta}{\partial r} &= 0 \\
\frac{\partial \beta}{\partial \theta} &= \frac{1}{\Delta l} \\
\frac{\partial \beta}{\partial \Delta l} &= -\frac{\theta}{\Delta l^2}.
\end{aligned}
\tag{2.20}
$$

From these expressions, and assuming that there is no covariance between errors in the argument of method functions and the line lengths, the variances of the attenuation and phase constants are given by

$$
\begin{aligned}
\sigma_\alpha^2 &= \left|\frac{\partial \alpha}{\partial \Delta l}\right|^2 \sigma_{\Delta l}^2 + \left|\frac{\partial \alpha}{\partial r}\right|^2 \sigma_r^2 \\
&= \left|\frac{\alpha}{\Delta l}\right|^2 \sigma_{\Delta l}^2 + \left|\frac{1}{r\Delta l}\right|^2 \sigma_r^2,
\end{aligned}
\tag{2.21}
$$

$$
\begin{aligned}
\sigma_\beta^2 &= \left|\frac{\partial \beta}{\partial \Delta l}\right|^2 \sigma_{\Delta l}^2 + \left|\frac{\partial \beta}{\partial \theta}\right|^2 \sigma_\theta^2 \\
&= \left|\frac{\theta}{\Delta l^2}\right|^2 \sigma_{\Delta l}^2 + \left|\frac{1}{\Delta l}\right|^2 \sigma_\theta^2,
\end{aligned}
\tag{2.22}
$$

respectively.

As seen in the developed expressions, choosing a bigger Δl is the simplest way of reducing α and β variances. However, r and θ are just the absolute value and the phase of the argument of method functions. What can be measured is the magnitude ($\sigma_{|S_{21}|}^2$) and phase ($\sigma_{\phi S_{21}}^2$) variances of the S-parameters, that are a characteristic of each VNA. Due to the complexity of the equations obtained, it is impractical to obtain an analytical solution for the variances in Eqs. (2.21), (2.22) as a function of $\sigma_{|S_{21}|}^2$ and phase $\sigma_{\phi S_{21}}^2$. However, for the ideal case of Method 2 shown in Eq. (2.15), σ_α^2 and the phase σ_β^2 can be expressed as

$$\sigma_\alpha^2 = \left| \frac{\alpha}{\Delta l} \right|^2 \sigma_{\Delta l}^2 + 2 \left| \frac{1}{S_{21} \Delta l} \right|^2 \sigma_{|S_{21}|}^2, \tag{2.23}$$

$$\sigma_\beta^2 = \left| \frac{\theta}{\Delta l^2} \right|^2 \sigma_{\Delta l}^2 + 2 \left| \frac{1}{\Delta l} \right|^2 \sigma_{\phi S_{21}}^2. \tag{2.24}$$

These equations have been calculated by taking Eq. (2.15) and following the same procedure made in Eq. (2.20).
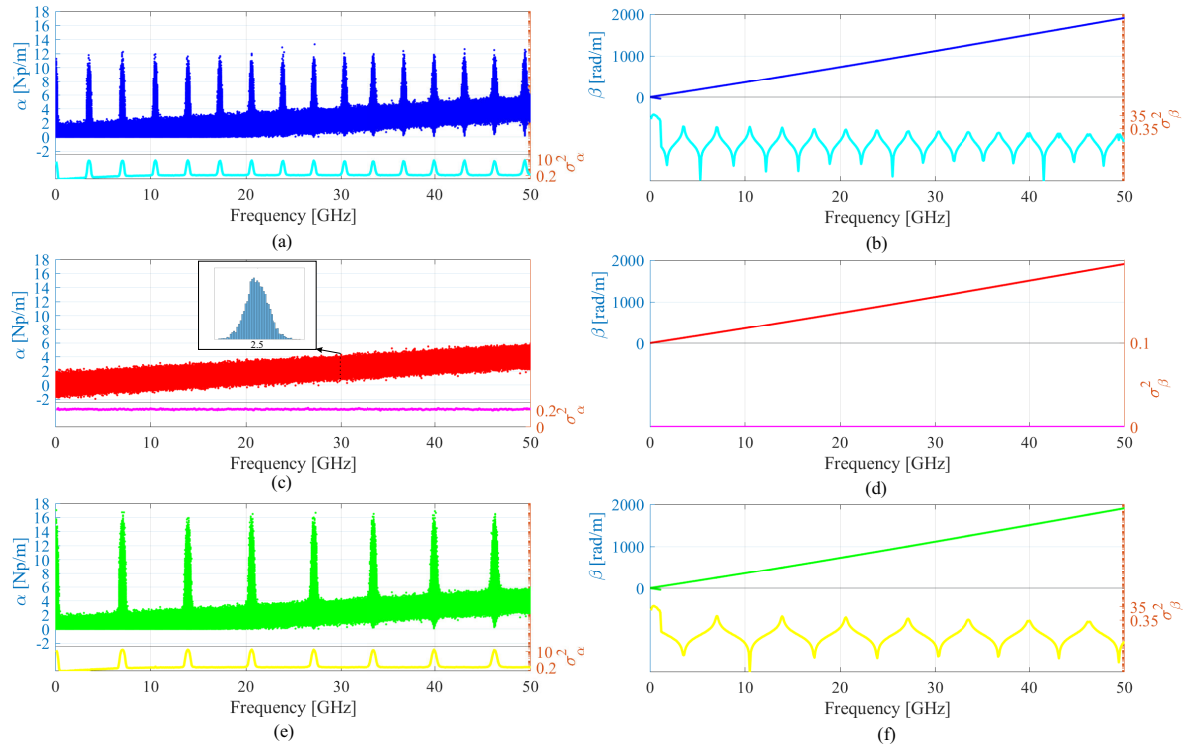
Figure 2.3: Attenuation and phase constants and their variances obtained by using $\sigma_{|S|} = 0.1$ dB through Method 1: (a), (b), Method 2: (c), (d), Method 3: (e), (f).

A Monte Carlo simulation has been performed to cover all cases, using S-parameters and line length errors. The lines defined in the previous section, of length 10 and 35 mm respectively, were used. The standard deviations were set to $\sigma_{|S|} = 0.1$ dB, $\sigma_{\phi S} = 5°$ and $\sigma_{\Delta l} = 0.02$ mm and errors were generated using a Gaussian distribution [41]. Figures 2.3 and 2.4 show the influence of the magnitude and phase error for each of the methods. As seen, there is a resonant behavior in Methods 1 and 3. The resonances in Method 1 are located at the points $(n-1)\lambda = \Delta l$, while in Method 3 are located at $\left(\frac{n-1}{2} \right) \lambda = \Delta l$, for $n = 1,2,3...$ However, there is a greater variance in Method 3 than in Method 1. On the other hand, Method 2 works in a completely different way because σ_α^2 is constant in frequency with the magnitude error and 0 with the phase error, as
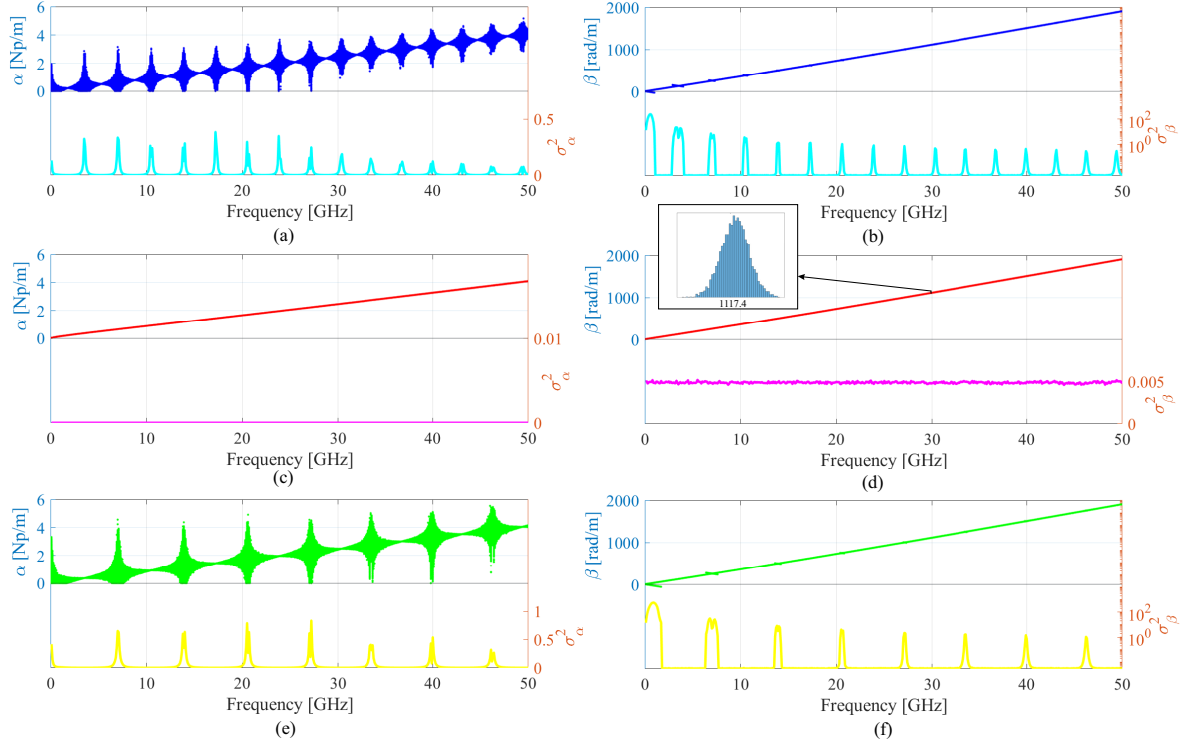
Figure 2.4: Attenuation and phase constants and their variances obtained by using $\sigma_{\phi S} = 5°$ through Method 1: (a), (b), Method 2: (c), (d), Method 3: (e), (f).

expected in the ideal case shown in Eq. (2.23). Furthermore, the variance obtained using Eq. (2.23) is similar to the one shown in Figs. 2.3 and 2.4. It is also relevant to mention that this is the only method that allows negative solutions for the attenuation constant if only the positive square root solutions in Eq. (2.17) are considered.

Regarding the phase constant, Figs. 2.3 and 2.4 depicts how magnitude and phase error affects it. As seen, the effect produced is quite similar to the one of the attenuation constant. Note that what is plotted is not the phase constant itself but the unwrapped one. This is because mathematical software usually takes just the principal value (first solution for $n = 0$) in Eq. (2.19). That solution is between $\beta = \pm\pi/\Delta l$ and have no physical meaning, as β increases with frequency. For this reason, a phase unwrap of $\beta \cdot \Delta l$ must be performed to obtain the estimated value of β. The unwrap function works great when there are no errors. However, when random errors are introduced, the algorithm may pick an incorrect solution. This effect is more significant at very low frequencies when the value of the phase constant is lower.

Finally, Fig. 2.5 shows the influence of line length error. Only Method 1 results are plotted, as they are equal to those obtained through Methods 2 and 3. As expected in Eqs. (2.21) and (2.22), this error results in a bias in the solution, and the variance
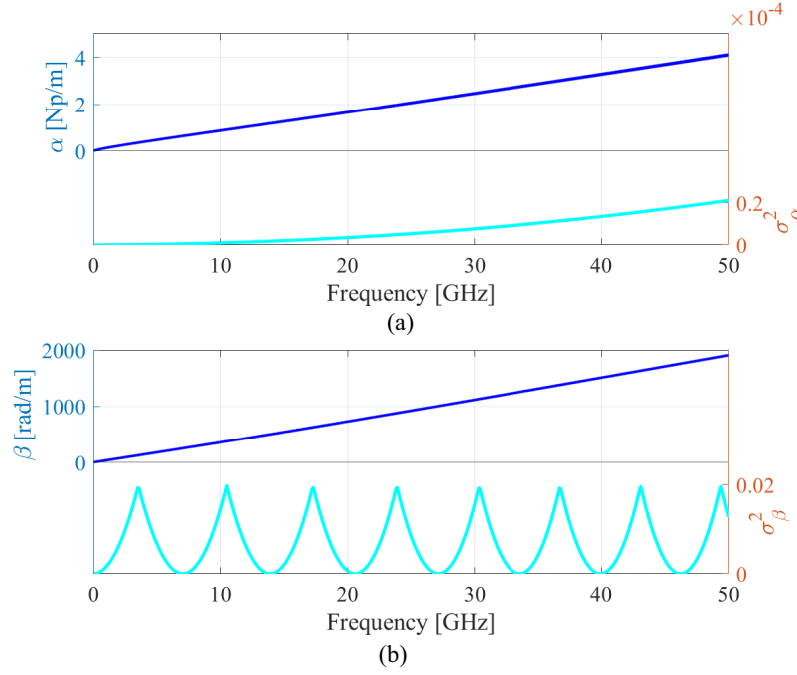
Figure 2.5: Attenuation (a) and phase (b) constants and their variances obtained by using a line length variance $\sigma_{\Delta l} = 0.02$ mm through Method 1.

increased with α^2 and θ^2. However, it must be taken into account that, because of the unwrap behavior previously mentioned, the maximum and minimum values of θ are $\pm\pi/\Delta l$ respectively, so the value of σ_β^2 will be limited. The performance of the sensitivity analysis has been validated through T-tests, showing that the attenuation and phase constants have a Gaussian distribution. In addition, and to show them, two histograms have been depicted in Figs. 2.3 and 2.4.

2.4 Minimization approach

2.4.1 Overdetermination of the methods

The presence of random errors means that it is impossible to determine the propagation constant's exact value. Hence, the objective is to achieve the best estimation from available measurements. In the previous section, it has been demonstrated how these errors affect the different methods examined in this chapter. To improve the accuracy of the methods, it is proposed to increase the number of lines to be measured and to use a LS estimation. Thereby, the effects produced by random errors in measurements are minimized as the LMS is the maximum likelihood estimator for a Gaussian distribution. The propagation constants can be obtained by solving the equations:

1. Method 1:

$$\min_{\alpha,\beta} \frac{1}{2} \sum_{n=1}^{N} \left| \text{trace}([M]) - \left(e^{+\gamma\Delta l} + e^{-\gamma\Delta l} \right) \right|^2, \qquad (2.25)$$

2. Method 2:

$$\min_{\alpha,\beta} \frac{1}{2} \sum_{n=1}^{N} \left| \left(\frac{1/\lambda_1 + \lambda_2}{2} \right) - e^{+\gamma\Delta l} \right|^2, \qquad (2.26)$$

3. Method 3:

$$\min_{\alpha,\beta} \frac{1}{2} \sum_{n=1}^{N} \left| \left(\frac{\det\left([M_{1+2}]\right)}{\det\left([M_1]\right)} - 2 \right) - \left(e^{+\gamma\Delta l} + e^{-\gamma\Delta l} \right) \right|^2, \qquad (2.27)$$

where N is the number of possible combinations between all the k lines, taken two by two. The measurements of S-parameters of N lines, $N > 2$, get to M simultaneous non-linear complex equations. The value of M is given by the combinations of N lines taken two by two: $M = 1/2 \cdot N(N-1)$. Increasing the number of lines, the total number of combinations increases rapidly, so the number of estimations of the propagation constant is also increased. In the experiment that has been carried out, seven lines has been used, providing 21 combinations of lines taken two by two. Increasing N is, therefore, a reasonable way to reduce uncertainty, but this increment should be accompanied by different Δl values to achieve better results. Optimal line lengths selection will be explored in the next section.

2.4.2   Optimal line lengths

One of the most essential parts to reduce random errors is the choice of the employed line lengths. The length distribution must be chosen so that the differences between the increments in the length of the lines should be as small as possible. In addition, the bigger the increments, the better. Constant increments in length between different TLs concentrate resonances in a discrete number of frequency points. Slight deviations from that pattern spread the resonances through the band of interest. The selected lengths can follow a quasi-linear distribution

$$l_i = l_0 + \Delta L \left(\frac{i-1}{N-1} \right)^q, i = 1, 2, ...N, \qquad (2.28)$$

or a logarithmic one

$$l_i = l_0 + \Delta L \frac{\log \left(l_0 + \frac{i-1}{N-1}\Delta L\right) - \log\left(l_0\right)}{\log\left(l_N\right) - \log\left(l_0\right)}, i = 1, 2, ...N, \tag{2.29}$$

where l_0 is the shortest line length, l_N is the longest, and $\Delta L = l_N - l_0$. In the quasi-linear one, the factor q just need to be adjust to a value different of 1 (that is the linear distribution). The frequencies where the phase difference of measured S_{21} is zero can be easily obtained from

$$f_n = \frac{n \cdot c}{\Delta l \sqrt{\varepsilon_{\text{r,eff}}}}, \quad n = 1, 2, 3... \quad . \tag{2.30}$$

Figure 2.6 compares histograms of the aggregation of frequencies where the phase difference between measured S_{21} appears. As seen, $q = 1.2$ and the logarithmic one are the most homogeneous distributions through the frequency band, whereas $q = 1$ still shows a resonant behavior. Furthermore, as the resulting covariance improves with larger length increments, the quasi-linear distribution has those increments. It will be chosen to perform the experimental validation of the methods. The choice of this strategy, spreading resonances over frequency, allows better results as a LS procedure is used.
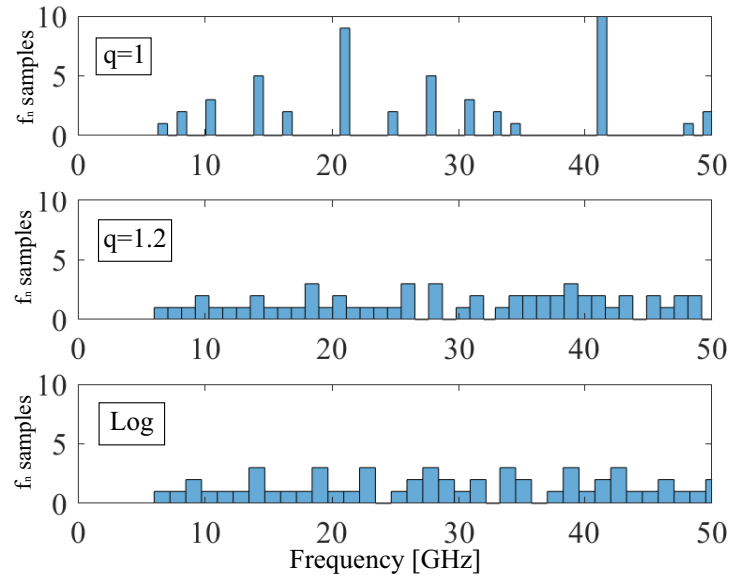
Figure 2.6: Histograms of f_n for different line length distributions.

2.4.3   Results

To assess how overdetermination affects random errors, the experiment shown in Section 2.3 has been repeated using seven lines instead of two. To choose the line lengths, the three distributions set out in Fig. 2.6 were used. The minimum (l_0) and maximum (l_N) line lengths are set to 10 and 35 mm, respectively. All line lengths are depicted in Table 2.1.

Table 2.1: Line lengths using different cutting stragegies.

Length strategy	l_1 (mm)	l_2 (mm)	l_3 (mm)	l_4 (mm)	l_5 (mm)	l_6 (mm)	l_7 (mm)
Linear	10	14.16	18.33	22.50	26.66	30.83	35
Quasi-linear ($q = 1.2$)	10	12.91	16.69	20.88	25.37	30.09	35
Logarithmic	10	16.95	22.09	26.18	29.57	32.47	35
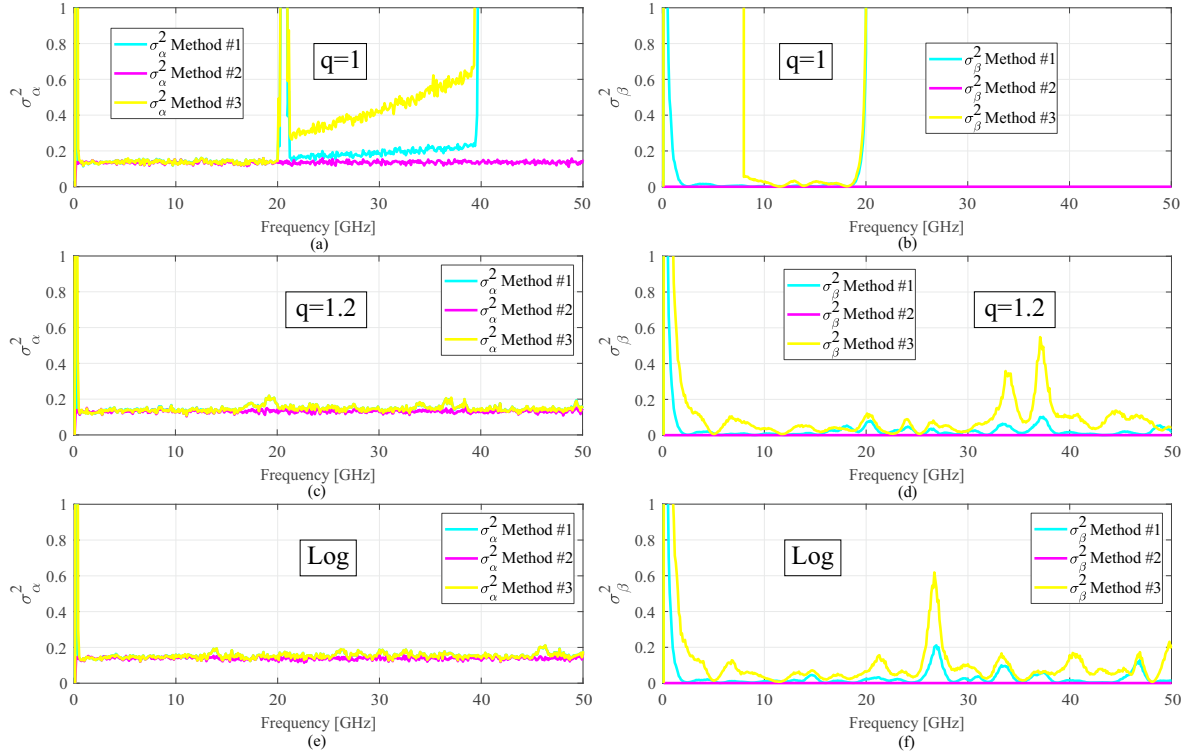
Figure 2.7: Attenuation and phase constants variances obtained for $\sigma_{|S|} = 0.1$ dB and the three proposed methods using a linear criteria (a), (b), quasi-linear criteria (c), (d) and logarithmic criteria (e), (f).

Figures 2.7 and 2.8 show the variances of the attenuation (σ_α^2) and the phase (σ_β^2) constants respectively for the aforementioned length strategies and the three proposed methods. In these figures, the standard deviations were set to realistic values of $\sigma_{|S|} = 0.1$ dB and $\sigma_{\phi S} = 5°$, the same values used in Section 2.3, in order to evaluate the improvements produced by the overdetermination of the methods. As seen, increasing
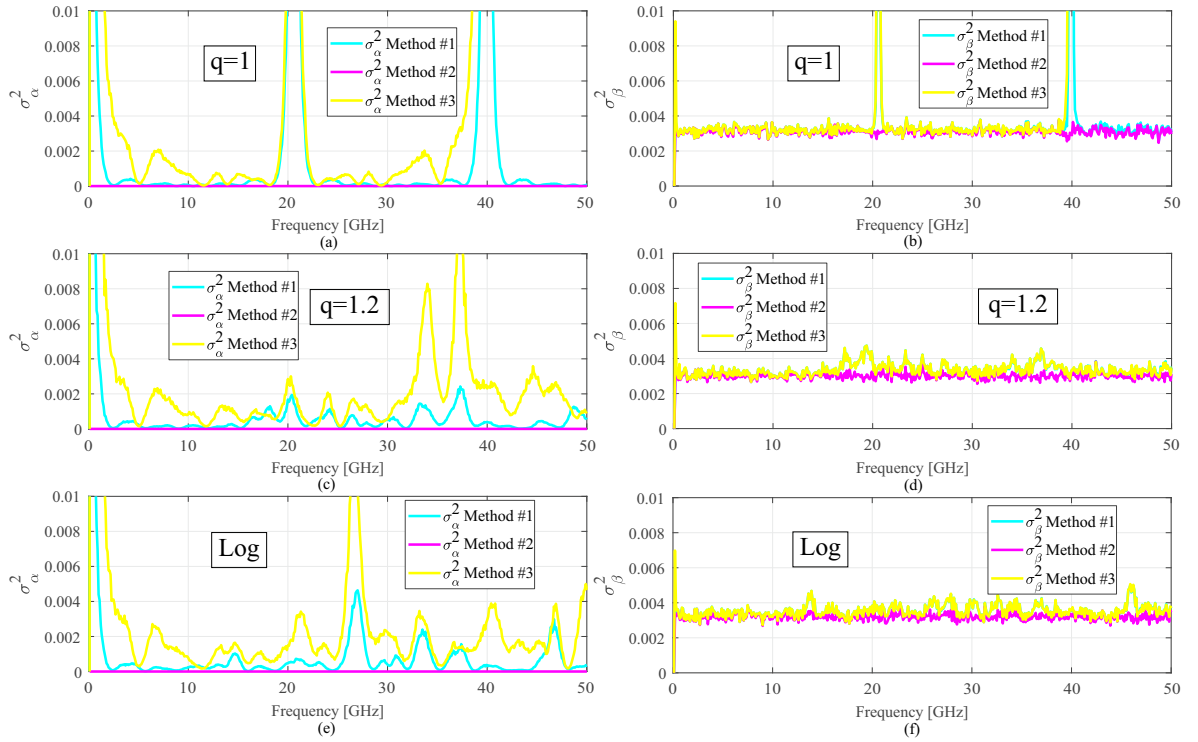
Figure 2.8: Attenuation and phase constants variances obtained for $\sigma_{\phi S} = 5°$ and the three proposed methods using a linear criteria (a), (b), quasi-linear criteria (c), (d) and logarithmic criteria (e), (f).

the number of lines significantly reduces errors in the propagation constant. On the one hand, the values of σ_α^2 and σ_β^2 are less than the ones using 2 lines. On the other hand, the resonant behavior has practically disappeared when the two non-linear length strategies are employed. Using these strategies, the results of Methods 1 and 3 are considerably improved and can be comparable to the ones of Method 2. Furthermore, and as expected, quasi-linear and logarithmic strategies work similarly.

Regarding the length error, Fig. 2.9 shows the resultant variance of the propagation constant after applying the proposed overdetermination of the methods to the afore-mentioned seven lines. For this plot, the standard deviation of the length has been set again $\sigma_{\Delta l} = 0.02$ mm. The results are considerably better than the ones in Fig. 2.5, when the methods were applied to 2 lines. Furthermore, it is noteworthy that, again, the linear distribution maintains a resonant behavior, whereas the quasi-linear and the logarithmic ones work similarly.
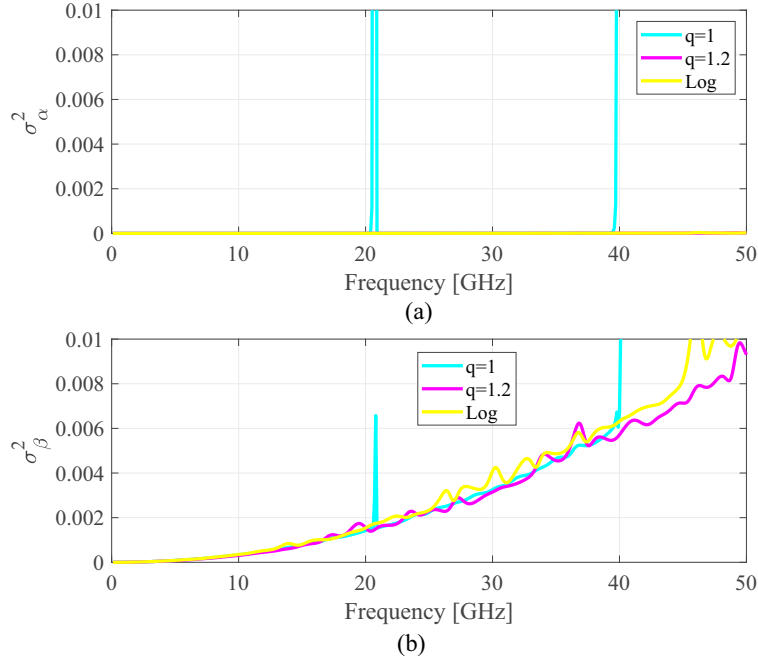
Figure 2.9: Attenuation (a) and phase constants (b) variances obtained for $\sigma_{\Delta l} = 0.02$ mm and the three proposed methods.

2.5 End-launcher repeatability errors

2.5.1 Experiment description

To study how connector repeatability errors affect the proposed methods, the starting point will be the initial diagram of this chapter, shown in Fig. 2.1. In this scheme, matrices $[R_A]$ and $[R_B]$ include launcher effects, whereas $[L_i]$ includes each TL effects. Measured matrix $[M_i]$ can be expressed as $[M_i] = [R_A][L_i][R_B]$. All methods considered assume that transitions and, therefore, matrices $[R_A]$ and $[R_B]$ are the same in every measurement. However, this fact is not entirely true since real connector repeatability is not considered. For this reason, what is proposed is to analyze the standard deviation of $[R_A]$ and $[R_B]$ in a set of measurements. They can be considered as error boxes in a TRL calibration. For this purpose, a multiline TRL kit [29, 42, 43] is manufactured and measured to isolate the effects of the transitions in the whole frequency band of interest. Substrate Rogers RO4350B, with 20 mil thickness, $\varepsilon = 3.66$, $\tan \delta = 0.0031$, and 17.5 μm thick copper metallization was used, whereas the lines were ended with 1.85 mm Southwest 1892-03A-6 end launchers connectors (dielectric diameter of 39 mils, pin diameter of 7 mils). As seen in [44], the frequency response of connectors slightly deteriorates at higher frequencies, but the invariant nature of the methods allows the

connectors to be used up to 67GHz. The microstrip line width was set to 1.095 mm, to get a 50 Ω characteristic impedance, Z_0. Measurements were taken using the VNA Agilent PNA-X (N5247A), between 0.01 and 67 GHz, the whole range of the available instrumentation.
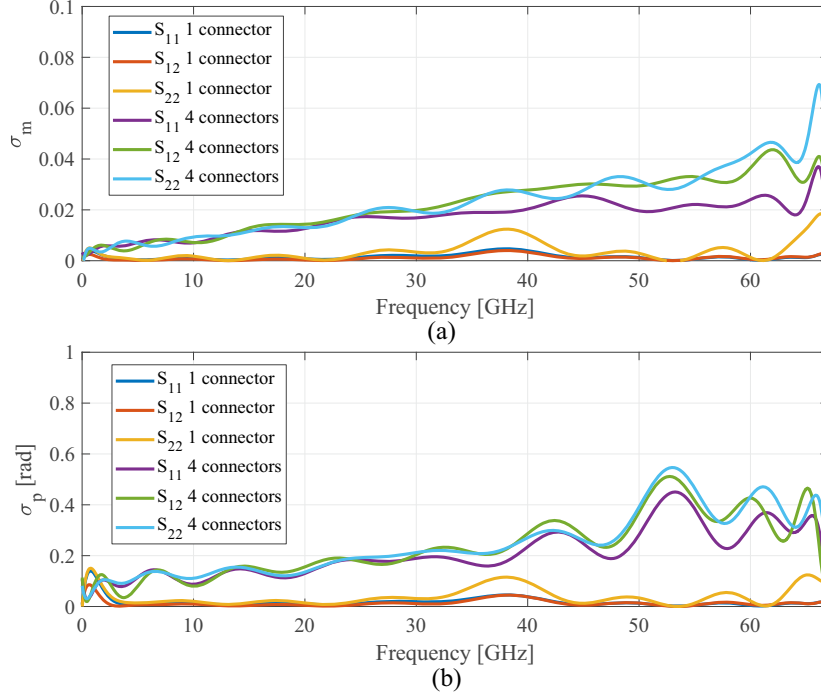
Figure 2.10: Standard deviation in magnitude (a) and phase (b) of transition S-parameters obtained after measuring sixteen 1.85 mm connectors, using 1 and 4 different connector kits.

The experiment was carried out in two ways. On the one hand, sixteen measurements were taken for each port, always using the same connector kit, which is disconnected and disassembled after every measurement to simply introduce actual random errors. On the other hand, four different connectors were used in each port, taking four measurements with each connector and disconnecting and disassembling them after each measurement. Later, a de-embedding process was performed to obtain the error boxes of each set of measurements. Finally, the standard deviation of these error boxes' real and imaginary parts was calculated and represented in terms of in-phase/quadrature covariance-matrix [45]. Figure 2.10 depicts the magnitude (σ_m) and phase (σ_p) standard deviations, calculated from the in-phase/quadrature covariance-matrix. As seen, the standard deviation is higher when using different connectors, which will influence on how the methods work, as the transitions are different. Furthermore, it is important to evaluate the probability distribution of the estimated transition S-parameters. For this purpose, what is proposed is to carry out an Anderson-Darling test [46] that

validates whether the transition S-parameters follow a Gaussian distribution or not. This hypothesis is valid for the distribution in magnitude and phase of all the obtained transition parameters, both for a connector and for the joint distribution of different connectors, at 5% significance level. In Fig. 2.11 a probability plot of the transition S_{12} at 10.5 GHz, 33.5 GHz and 62.5 GHz is shown for two different connectors. As seen, data fits a normal distribution. This result is significant, ensuring that the distribution of errors is appropriate for the subsequent analysis.
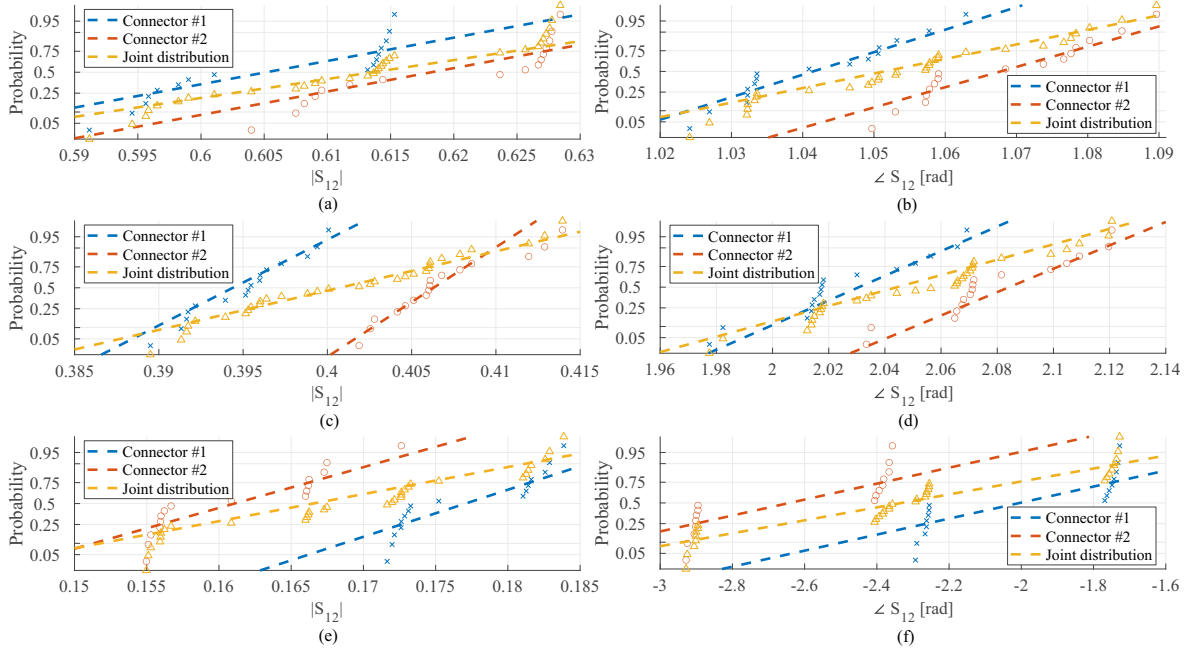
Figure 2.11: Probability plot of transitions S_{12} in magnitude and phase at 10.5 GHz (a)(b), 33.5 GHz (c)(d) and 62.5 GHz (e)(f) using 1 and 2 different connectors.

2.5.2 Method susceptibility to repeatability errors in transitions

The main objective is to study how several approaches traditionally used to obtain the propagation constant behave with respect to connector repeatability. To carry out the study, standard deviations plotted in Fig. 2.10 are the starting point of a Monte Carlo simulation that takes $[R_A]$ and $[R_B]$ as two random matrices, generated using a normal distribution (hypothesis validated in the previous section) as

$$\begin{bmatrix} (\delta + \sigma_{m_{S11}})e^{j\sigma_{p_{S11}}} & (1 + \sigma_{m_{S12}})e^{j\sigma_{p_{S12}}} \\ (1 + \sigma_{m_{S12}})e^{j\sigma_{p_{S12}}} & (\delta + \sigma_{m_{S22}})e^{j\sigma_{p_{S22}}} \end{bmatrix}, \tag{2.31}$$

Figure 2.12: Attenuation (a) and phase (b) constants and their standard deviation obtained by using 1 and 4 connector kits through Method 2.

and then transforming it to T-parameters. The parameter δ is introduced to ensure that S_{11} and S_{22} are non-zero terms in case the magnitude error is 0. A value of $\delta = 0.0001$ is used. The value of $[R]$ T-parameters would not affect if there were no errors since all the methods eliminate the effects of the transitions if they are the same in each measurement. $[L_i]$ matrices are generated from an EM simulation using ANSYS HFSS [47], considering two lines of lengths 11.31 and 52.59 mm, respectively, without taking into account any VNA error. Figure 2.12 depicts the results of the Monte Carlo simulation. In this case, and unlike random errors of the VNA, the three considered methods work in the same way concerning connector repeatability errors. For this reason, only results of Method 2 are displayed, as they are similar to Methods 1 and 3, to simplify figures. As seen, results are considerably better when using just one connector kit (red trace in Fig. 2.12) for both lines instead of using different kits (blue trace) for each line. As expected, the attenuation constant is significantly more sensitive to repeatability errors than the phase constant. However, the phase constant deteriorates considerably from 40 GHz to the limit of the considered frequency band.

This fact is because it is obtained from equation

$$\beta = \frac{\theta + 2n\pi}{\Delta l},\tag{2.32}$$

which has infinite possible solutions. To get the correct one, it is necessary to unwrap the phase, but when there are large random errors, the unwrap function can fail and take the phase constant to another solution that is not physically correct. As shown in the histograms of Fig. 2.12, the propagation constant obtained after applying the method considering Gaussian errors continues having a Gaussian probability distribution. This hypothesis has been validated through an Anderson-Darling test at 5% significance level. In addition, there is a similarity between the standard deviation of $[R]$ displayed in Fig. 2.10 and the one of the propagation constant (σ_α and σ_β), showed in Fig. 2.12 (note that Y-axis is displayed logarithmically in this figure).

2.6   Real case method assessment by measurements

2.6.1   VNA and line lengths errors

The developed theory has been tested using circuital simulations in the previous sections. A set of 7 lines made of Rogers RO4350B has been manufactured to validate the procedure experimentally. This material, whose permittivity and dispersion are known and given by the manufacturer [40], will be used to assess the methods's performance. This frequency-dependent permittivity is imported into the full-wave simulator ANSYS HFSS [47] to obtain a more realistic and accurate simulation that can be compared with the experimental results. Considering that similar results are obtained when using a quasi-linear or a logarithmic distribution, the first one ($q = 1.2$) has been chosen to design the line lengths. These lengths are depicted in Table 2.1. S-parameters of the seven lines are taken by using the VNA Agilent PNA-X (N5247A), between 0.01 and 50 GHz. A photograph of the real measurement setup is shown in Fig. 2.13. Figure 2.14 depicts the simulated and measured results of the structure. The phase constant, β, has been plotted in terms of effective relative permittivity, $\varepsilon_{\mathrm{r,eff}}$, to reduce the range of possible values and to make it easier to extract information from the graph. For this purpose, the variance of the effective relative permittivity can be obtained from the transformation

$$\sigma^2_{\varepsilon_{\mathrm{r,eff}}} = \sigma^2_\beta \left| \frac{\partial \varepsilon_{\mathrm{r,eff}}}{\partial \beta} \right|^2 = 2\sigma^2_\beta \frac{c^2}{\omega^2}\beta.\tag{2.33}$$
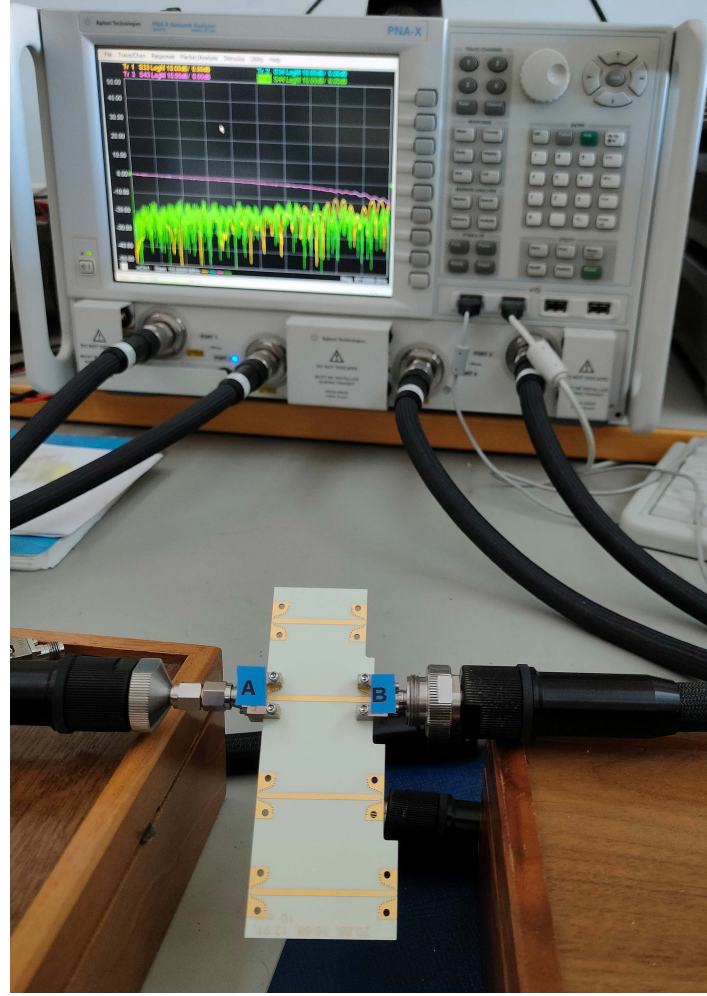
Figure 2.13: Photograph of microstrip lines and the measurement setup using Vector Network Analyzer for S-parameters measurement.

The confidence intervals shown in Fig. 2.14 have been calculated from Eqs. (2.23) and (2.24). S-parameter magnitude and phase variances have been extracted from the VNA datasheet [48]. In contrast, length variance has been chosen by taking ten measures of the same line with a digital caliper and calculating the variance of these measurements, being $\sigma^2_{\Delta l} = 0.02$ mm. As it can be seen, the confidence intervals are discontinuous in frequency. This is because the VNA manual specifies S-parameter variances for different frequency ranges, so shifts in confidence intervals are located in the frequency points in which an interval change occurs in the VNA, being more noticeable in the attenuation constant.

As seen in Fig. 2.14, both the 2-lines and the 7-lines results are within the confidence intervals. The attenuation constant obtained by taking two lines shows the difference between the three proposed methods quite well. Method 1 displays a resonant behavior
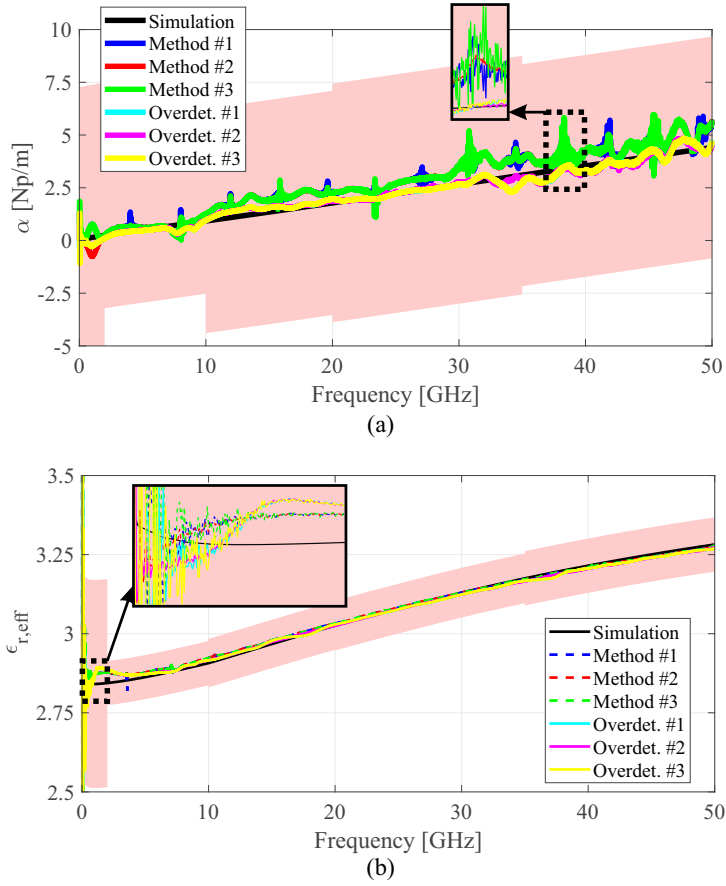
Figure 2.14: Experimental results of the attenuation (a) and phase (b) constants using the proposed methods with 2 and 7 lines, in comparison with electromagnetic simulation.

in more frequencies than the rest. However, these resonances are noisier in Method 3, whereas Method 2 is the most insensitive to errors. However, it is important to mention that the overdetermination of the three methods eliminates most of the noise and makes the measured attenuation constant quite similar to the one obtained through EM simulation. The same reasoning can be applied to effective relative permittivity. Specifically, in the lower frequencies, it is possible to see that both Method 1 and 3 are much noisier than Method 2. However, the methods are much more accurate for estimating the phase constant. This is mainly because the phase variance of the VNA is much smaller than the magnitude one. Despite this, the experimental results show an excellent agreement with the simulated ones, which points out the use of this kind of overdetermined methods to estimate the propagation constant. One of the points to pay attention to is the propagation of higher-order modes, limiting the microstrip' operational bandwidth. The cutoff frequencies of such modes can be found in [49]. These modes usually affect high permittivity substrates or very wide track widths. In the case of the line used, the first mode that could be excited would be Transverse

Microstrip Resonance, at 40 GHz. The rest are outside the measurement bandwidth. However, given the results' accuracy, there does not seem to be a problem of higher modes in the characterized transmission line.

2.6.2   Connector repeatability errors
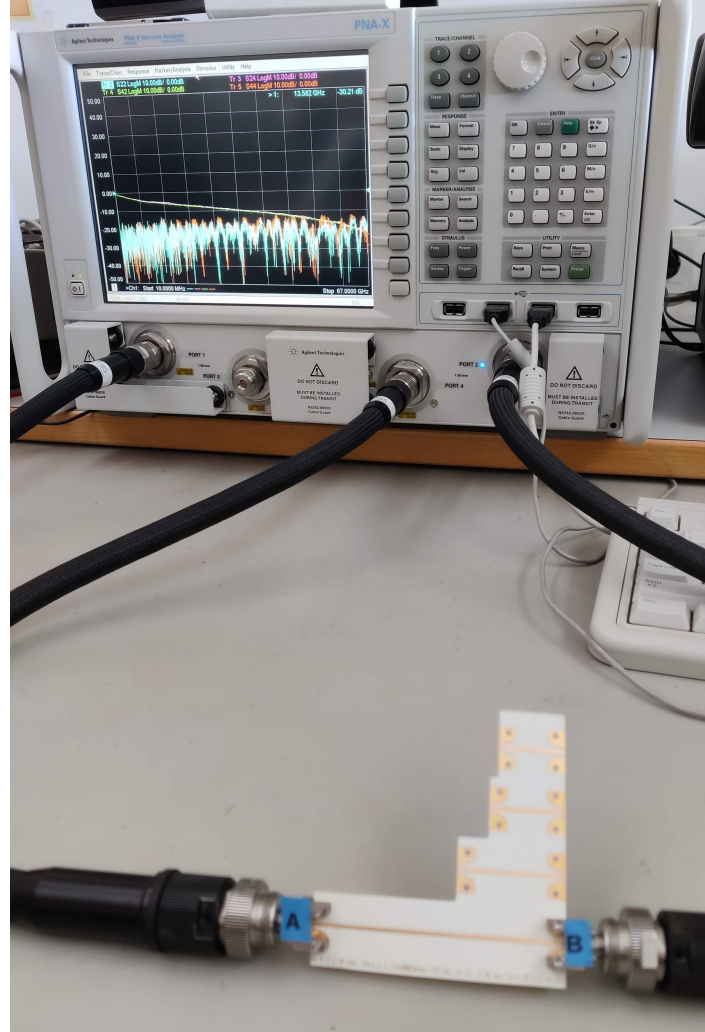
Figure 2.15: Photograph of four microstrip transmission lines and the measurement setup using Vector Network Analyzer for S-parameters measurement. The picture shows a pair of labeled connectors that are used through the measurement process.

To validate the analysis performed, the two lines simulated in the previous section with lengths 11.31 and 52.59 mm are manufactured using Rogers 4350B to extract the propagation constant. These lines are measured using the same VNA as in Section II, between 0.01 and 67 GHz. At this point, it is essential to mention that measurements were taken without any calibration of the VNA since the proposed methods do not

require it to work properly [50]. A photograph of the measurement setup is shown in Fig. 2.15. In a similar way as done above, sixteen measurements of each line have been taken using the same pair of connectors, and another sixteen measures combining four different connector kits. From these measurements, Method 2, which is the least sensitive to the VNA's random errors, has been applied to all the possible combinations of lines, using 1 or 4 different connector kits for each line. Each connector is assembled and disassembled before each measurement to emulate a real measurement process. Results of the estimated propagation constant are depicted in Fig. 2.16 in terms of attenuation and phase constants. Both the mean and the standard deviation of these results have been represented. As seen, keeping the same pair of connectors reduces the standard deviation of the estimated propagation constant considerably, as discussed in the previous section. The measured propagation constants continue to fit a normal distribution, as validated through an Anderson-Darling test at a 5% significance level. Furthermore, it is noteworthy that the attenuation constant has less ripple and is more accurate at higher frequencies when only one connector kit is used. Losses are one of the main drawbacks of this kind of methods, and this can be a simple way of reducing uncertainty in the estimation of α and β significantly.
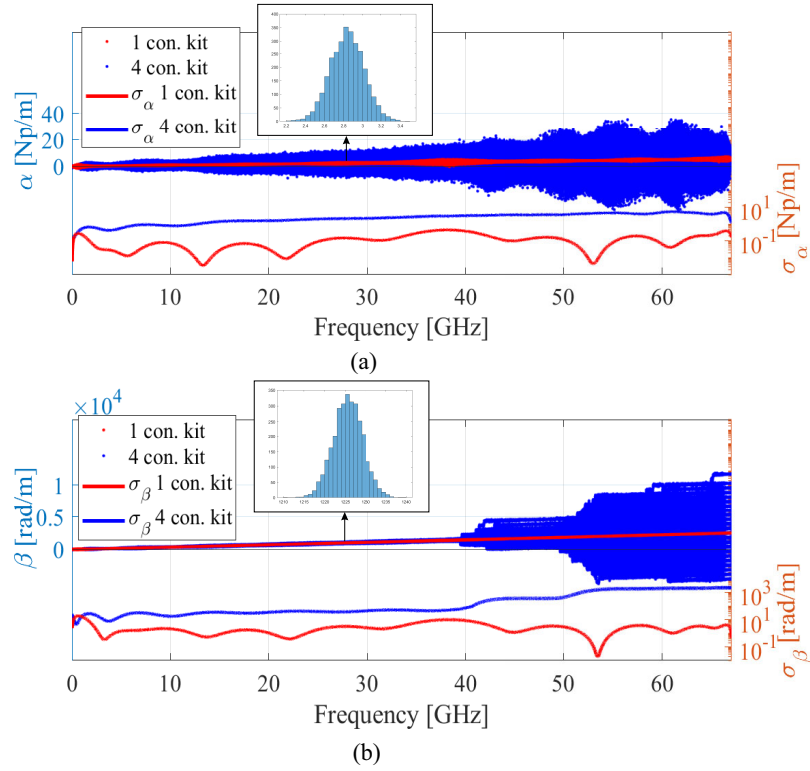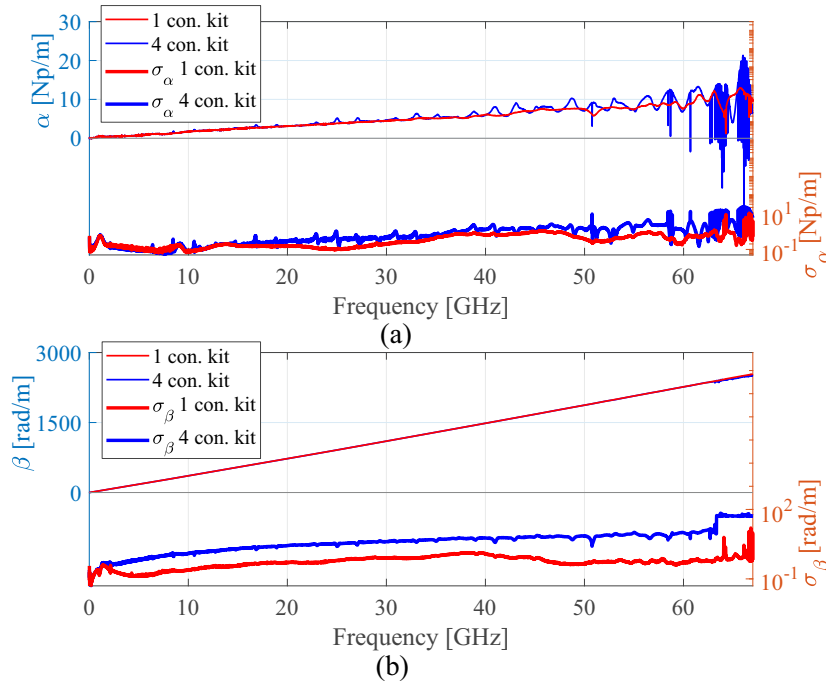

Figure 2.16: Mean of the estimated attenuation constant (a) and phase constant (b) and their standard deviation obtained by using 1 and 4 connector kits through Method 2.

2.7   Conclusion

In this chapter, we have studied how three different methods used for the experimental characterization of the propagation constant of TLs are affected by various sort of random errors. Although it might be thought that these three methods work similarly, it has been demonstrated that they have totally different behavior in the presence of VNA and line lengths random measurement errors. Specifically, the method based on eigenvalues is the one that shows better tolerance to errors, while the other two have resonant behaviors. For this reason, it is considered the best option to use an eigenvalue-based method to calculate the propagation constant when only two-line measurements are available. To reduce errors in the propagation constant, the proposed overdetermination of the methods, based on a LS approximation, works better when the number of lines is increased. Furthermore, resonant behavior can be eliminated by using the proposed non-linear length selection criterion. If it is taken, all the methods work in a similar way regarding random errors. Regarding connector repeatability errors, all methods behave in the same way. It has been shown that using the same connector kit instead of different ones in all the TLs used for the characterization of the propagation constant is an appropriate way to reduce the uncertainty of the final estimation considerably. Finally, the developed analysis carried out has been corroborated by comparing EM simulations with real uncalibrated measurements, showing an excellent agreement between both attenuation and phase constants between simulated and measured results up to 50 GHz. In addition, the experimental results have shown that the behavior of the methods is different in the presence of errors and that it is improved substantially when the proposed overdetermination is applied.

Furthermore, it has been checked that taking measurements with the same kit of connectors reduces the standard deviation of both attenuation and phase constants. Therefore, it corroborates the analysis proposed in this chapter. This fact is especially relevant in estimating the attenuation constant, which is quite more sensitive to measurement errors. It reduces its ripple drastically and is much more accurate at higher frequencies if only one connector kit is used.

Chapter 3

Characterization of Structures Made Using Additive Manufacturing

In this chapter, an optimized broadband method using multilayer TLs to characterize the dielectric permittivity and loss tangent of material samples is presented. For this purpose, a microstrip line loaded with a piece of the selected dielectric to be characterized is used. The propagation constant can be obtained from two-port measurements and using different length lines. To minimize random errors and improve accuracy, an overdetermination of the method that increases the number of lines measured, and a criterion to choose the optimal line lengths is considered, as described in Chapter 2. Firstly, the measurement method is applied to uncovered microstrip lines, and an accurate substrate model is obtained. Secondly, the lines are covered with several materials, made by Fused Deposition Modeling (FDM) AM technique, such as ABS, Polylactic Acid (PLA), HIPS, Thermoplastic Polyurethane (TPU), Copolyester (CPE), FLEX, Polyethylene Terephthalate Glycol (PETG) and Nylon. A model of the TL considering the cover is developed, and an EM simulator is used to determine the cover material electrical parameters indirectly. Results show excellent agreement with EM simulations in the 0.01- to 67- GHz frequency band, so they assess the suitability of the proposed material characterization.

3.1   Introduction

Nowadays, the number of materials and manufacturing techniques available on the market is increasing rapidly. Concretely, AM technologies have become one of the

most researched topics in many scientific fields. Their main advantages include the low cost, the possibility of great customization, rapid prototyping, design flexibility, or the possibility of combining materials. Specifically, in microwave area, several designs have been proposed for different purposes [7, 51--54]. Mechanical properties are usually available from manufacturers. However, despite the large number of materials available, there is not much information about the EM properties of these materials. Furthermore, the wide variety of manufacturers and materials available make it very necessary to achieve characterization techniques as simple as possible to be accessible to all designers who want to use this kind of materials. Manufacturers of AM materials from time to time change the formulation of materials, or even different batches can produce different EM properties. For those reasons and considering the advantages and growth of this manufacturing technology, investigations on printed EM material properties have grown in the last few years [10].

Over time, numerous papers have been proposed in the literature to characcterize the propagation constant of planar TLs. They can be grouped mainly in two different categories, as explained in Chapter 2. On the one hand, resonant methods have been proposed for the characterization of printed materials [8, 55]. On the other hand, several broadband methods have been used in microwave [11] and millimeter bands [56] to characterize printed materials. Another novel strategy for the characterization of materials is the one proposed in [57], based on microstrip lines of variable width. It is noteworthy that most of these methods need calibrated S-parameters. However, the method used in this chapter does not require calibration because it is based on mathematical invariants. Some other methods, for instance such as those based on Nicolson-Ross-Wier method, do require calibration of the S-parameters to eliminate systematic errors [26, 58]. To increase the performance of measurement methods, the overdetermination of samples needed is usually considered [29, 42, 59], as previously considered.

It is important to mention that materials under consideration in this chapter do not replace conventional low loss materials, necessary especially at millimeter band as a substrate, i.e. for microstrip antennas. However, these materials can be used to generate structures in prototyping stages and final products or structural parts for supporting devices as radars or sensors at microwave or millimeter-wave bands. The dielectric parameters must be known accurately to be considered properly in EM simulators before fabrication. These materials can also play a functional role as ABS in [60, 61] or HIPS in [62]. Particularly, HIPS, as a polystyrene variant, has demonstrated to be a

candidate for millimeter-wave material. Other materials, such as TPU or FLEX, with flexible mechanical properties, could be useful in the microwave band for wearable and conformable circuitry. Although in certain areas AM is considered non-competitive in comparison to conventional manufacturing techniques, specifications of the complete system will mark the viability of the technology used. There are numerous works on radiating elements and waveguides [62], but there are not so many investigations where TLs are the main focus [7]. The need to interconnect systems based on coaxial to radiating elements requires the use of TLs manufactured with the same technology of those radiating elements. This is important in devices such as patch antennas. The TL plays a fundamental role since it will interconnect the different parts of the circuit. The problem is the combination of parts of dielectric and conductive materials. One of the possibilities is to use inkjet technology for metallic materials. However, this technique is strongly influenced by the conductivity of the resulting conductor, and it has not been very studied yet. For this reason, a study on how conductivity influences the estimation of the propagation constant is presented in Appendix A.

In this chapter, a method to find EM properties of material samples, made by AM FDM, is proposed. It is based on two-port measurements of microstrip TLs. For this purpose, it is required the use of a two-port VNA with no need of calibration. Dissipation factor and dielectric permittivity are determined in an extraordinary bandwidth, from 10 MHz up to the limit of the available VNA, 67 GHz. The broadband measurement method is described in Section 3.2. Several line length differences are considered to achieve better accuracy ousing the proposed methodology, and a previous microstrip characterization is carried out. A material sample to be characterized is placed over the microstrip line. The extraction of material parameters of a multilayer microstrip is based on the one in [63]. This procedure is shown in Section 3.3. Section 3.4 includes experimental and simulated results for the dielectric permittivity and the loss tangent of the used material samples. Finally, conclusions are provided in Section 3.5.

3.2 Broadband measurement method

3.2.1 Bianco and Parodi two lines method

The method addressed in this chapter is based on the one in [3], and was explained, in part, in Chapter 2. Therefore, this subsection will briefly replicate the complete process explained in the previous Chapter, just to facilitate a better understanding by

(a)

(b)
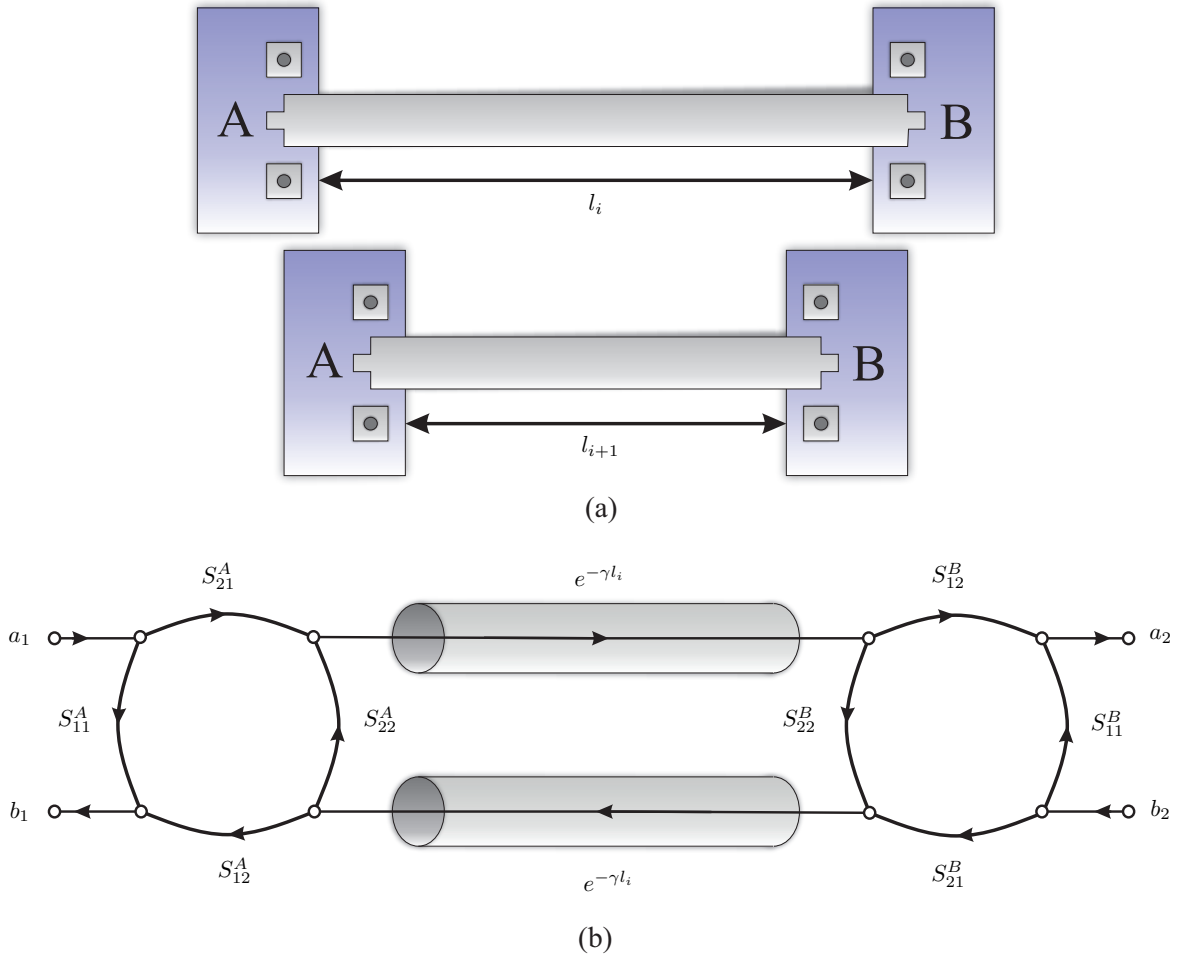
Figure 3.1: (a) Measurement setup using two microstrip lines. (b) Signal-flow of the model including error two-port circuits.

the reader. This method was then used in the estimation of the propagation constant in TRL calibration for six-port transmission measurements and VNAs [28, 64--66]. The measurement setup and the signal flow are depicted in Fig. 3.1. Firstly, it is necessary to take the S-parameters of two LUT with different lengths. It is noteworthy that the error two-port circuits R_A and R_B are the same throughout the whole set of measurements. The S-parameters have to be transformed into T-parameters, called M_1 and M_2. These matrices can be rewritten as $M_1 = R_A L_1 R_B$ and $M_2 = R_A L_2 R_B$, being L_1 and L_2 the transmission matrices of the lines excluding the effect provoked by the transitions between the LUT and the ports, whose effects are considered in R_A and R_B respectively. On the one hand, L_i are diagonal matrices, given by

$$L_i = \begin{bmatrix} e^{+\gamma l_i} & 0 \\ 0 & e^{-\gamma l_i} \end{bmatrix}, \tag{3.1}$$

being $L = L_1 L_2^{-1}$ and l_i the length of the line i.

On the other hand, the transmission matrices can be combined as

$$M = M_1 M_2^{-1} = R_A L_1 L_2^{-1} R_A^{-1} = R_A L R_A^{-1}. \tag{3.2}$$

At this point, it is important to highlight that both M and L are similar matrices [32], which means that their eigenvalues coincide and are given by

$$\lambda_1 = e^{-\gamma \Delta l}, \quad \lambda_2 = e^{+\gamma \Delta l}, \tag{3.3}$$

where $\Delta l = l_2 - l_1$. From (3.3), the propagation constant can be obtained as an average of those eigenvalues as

$$\gamma = \frac{1}{\Delta l} \ln \left(\frac{1/\lambda_1 + \lambda_2}{2} \right). \tag{3.4}$$

Considering Eq. (3.2), the use of calibrated or raw S-parameters does not affect the results. The inclusion of a new two-port error box cascaded with R_A and R_B do not affect similarity between the new M and L matrices. Therefore, it is not necessary to eliminate systematic errors calibrating the VNA before the measurement of TLs. This method proved to be the least affected by random errors, as explained in Chapter 2.

3.2.2   Problems due to the existence of multiple solutions

A problem associated with Eq. (3.4) is that the natural logarithm of a complex number has an ambiguity when $\beta \Delta l > \pi/2$, and phase shifts appear. This is due to the infinite solutions of this function, whose value is given by

$$\ln(z_p) = \ln |z_p| + j \left(\arg(z_p) + 2\pi k \right) \quad k = 0, 1, ..., \tag{3.5}$$

As it has infinite solutions, an infinite number of propagation constants can be obtained from Eq. (3.4). To fix this problem, Eq. (3.4) is solved using an iterative technique such as Newton's method to find the complex zero of

$$\gamma - \frac{1}{\Delta l} \ln \left(\frac{1/\lambda_1 + \lambda_2}{2} \right) = 0. \tag{3.6}$$

Nevertheless, this has an inconvenience: to achieve a good method performance, it is necessary to have good starting values, and it is not always possible to get the values

that allow finding the correct solution. Starting from the solution of the propagation constant at the lower frequency point, this value is used to initialize the second frequency point and so to the last frequency points. This way, the iterative process starts from a very close point to the correct solution.

3.2.3   Overdetermination of the method

Despite the problems associated with multiple solutions of Eq. (3.4), random errors introduced during the measurements of the S-parameters must be taken into account. Systematic errors could be removed by calibration, although it is not strictly necessary, because port effects are being considered in (3.4), by assuming that they are going to be the same in all the measurements. For this reason, all experiments performed in this chapter have been carried out without calibration, i.e., using raw data from the VNA.

Random errors, however, affect all the measurements and are not predictable or removable by calibration. They can be produced, in part, by the VNA. Nevertheless, the most important sources of random errors in the proposed method are the repeatability of the transitions and the estimation of the line lengths used. These errors mean that it is not possible to determine the exact value of the propagation constant, so the objective is to achieve the best estimation from the available measurements.

To improve the accuracy of the method, it is proposed to increase the number of lines to be measured and use a LS approximation. Thereby, the effects produced by random errors of measurements repeatability are minimized. The propagation constant is obtained by solving the equation

$$\min_{\alpha,\beta} \frac{1}{2} \sum_{n=1}^{N} \left| \left(\frac{1/\lambda_1 + \lambda_2}{2} \right) - e^{+\gamma\Delta l} \right|^2, \tag{3.7}$$

where N is the number of possible combinations between all the k lines, taken two by two. Increasing k is a good way to reduce uncertainty, but this increment should be accompanied by different Δl values, in order to achieve better results. Optimal line lengths selection will be explained in the next section.

Finally, it should be borne in mind that attenuation and phase constants will have very different order of magnitude. For this reason, errors in numerical optimization will penalize α much more than β. To avoid this, the transformation $\varepsilon_{\mathrm{r,eff}} = (c\beta/\omega)^2$ is applied in order to make both variables have the same order of magnitude, and Eq. (3.7)

is expressed as

$$\min_{\alpha,\varepsilon_{\text{r,eff}}} \frac{1}{2} \sum_{n=1}^{N} \left| \left(\frac{1/\lambda_1 + \lambda_2}{2} \right) - e^{+\gamma_t \Delta l} \right|^2, \tag{3.8}$$

being $\gamma_t = \alpha + j\,\omega\sqrt{\varepsilon_{\text{r,eff}}}/c$.
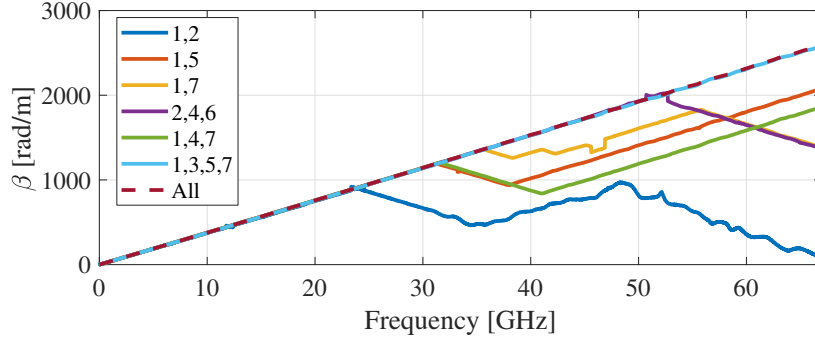
Figure 3.2: Phase constants using different line combinations.

To demonstrate how the method works, Fig. 3.2 shows the phase constant obtained from measurements of 7 lines with HIPS as top substrate. The measurement setup will be explained in following sections, but what is important to note at this point is that phase shifts [13, 67] occur at higher frequencies as the differences in line lengths are greater. From 4 lines, the bandwidth of the method reaches the measurement bandwidth. Furthermore, random errors decrease as the number of lines increases.

3.2.4   Optimal line lengths

Random errors are inherent to any estimation problem based on measurements made by real instruments. Considering Eq. (3.4), the attenuation and phase constants are obtained from the measurement of different lengths Δl_k, and the uncalibrated S-parameters measured using a VNA. To minimize the effect of these random errors, special care must be taken in connections repeatability, the similarity of connectors, and line lengths measurement.

Overdetermination of the method proposed using more than two lines will help minimize errors significantly. Apart from a very good statistical data processing and the repeatability of the connections, some other considerations must be taken into account to get reasonable estimations of the propagation constant. One of those is the choice of the line lengths employed. For that reason, the idea raised in Section 2.4 will be used to select the line lengths for material characterization, choosing a quasi-linear criterion. The frequencies where the phase difference of measured S_{21} is zero can be

easily obtained as

$$f_n = \frac{n \cdot c}{(l_b - l_a)\sqrt{\varepsilon_{\text{r,eff}}}}, \quad n = 1, 2, 3... \quad . \tag{3.9}$$

(a)

(b)
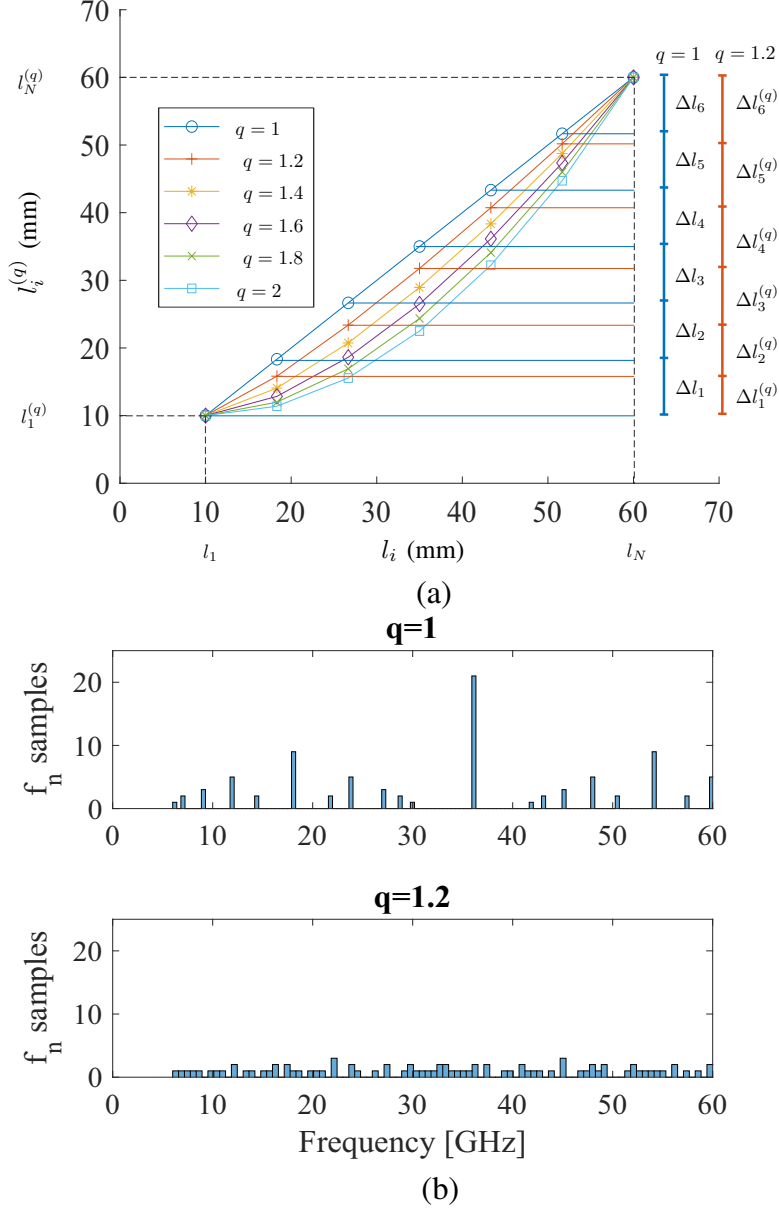
Figure 3.3: (a) Quasi-linear lengths of lines under test. (b) Histograms of f_n for different values of factor q.

Figure 3.3 shows the difference in the increment Δl_{ij} for different strategies. Figure 3.3(b) compares histograms of the aggregation of frequencies where the phase difference between measured S_{21} appears. For $q = 1.2$ the distribution is homogeneous through the frequency band.

3.2.5 Microstrip characterization

Once the method has been presented, it is evaluated through experimental validation and EM simulation. For this, 7 microstrip lines are manufactured over Rogers 4350B LoPro substrate, with 30 mil thickness, $\varepsilon_r = 3.66$, $\tan\delta = 0.0031$, and 17.5 μm thick copper metallization. The line lengths, shown in Fig. 3.4 caption, are calculated following the procedure explained in the previous section. The line width is set to 1.65 mm, in order to get a 50 Ω characteristic impedance.

The characterization method consists of measuring the S-parameters of the 7 lines. Later, Eq. (3.8) is applied, in order to obtain α and $\varepsilon_{r,eff}$, from which the estimated nominal ε_r of the substrate, including dispersion, is extracted using the Kirschning and Jansen model [68]. Finally, the obtained ε_r is imported into the commercial full-wave finite-element EM simulator ANSYS HFSS [47], and one of the seven microstrip lines is simulated, getting its propagation constant. The whole process is summarized in the flowchart of Fig. 3.5.

Figure 3.4 shows the measured and simulated effective permittivity and the attenuation constant obtained applying the method to the set of 7 lines. In addition, the information about the substrate dispersion given by the material manufacturer [40] up to 50 GHz is also depicted. As seen, there is an excellent agreement between the measured effective relative permittivity and the one obtained by simulation using manufacturer data. In this sense, it must be highlighted that the relative permittivity, obtained from the one in Fig. 3.4(b) using the Kirschning and Jansen model and plotted in Fig. 3.4(c), is quite similar to the one given by Rogers, showing how good is the proposed method for estimating this parameter. For this reason, the obtained ε_r of the Rogers 4350B LoPro substrate will be used in the next section for the simulation of the proposed structure to characterize more precisely the material samples, including lower substrate dispersion. Regarding losses, the disagreement (50 - 67 GHz) is because the lines were fabricated in the lab using an LPKF Protomat S103 machine, making the fabrication not as accurate as those of the lines in Chapter 2 (see the estimated propagation constant in Fig. 2.14). In addition, 2.4 mm connectors were used, for which the manufacturer only guarantees their response up to 50 GHz.
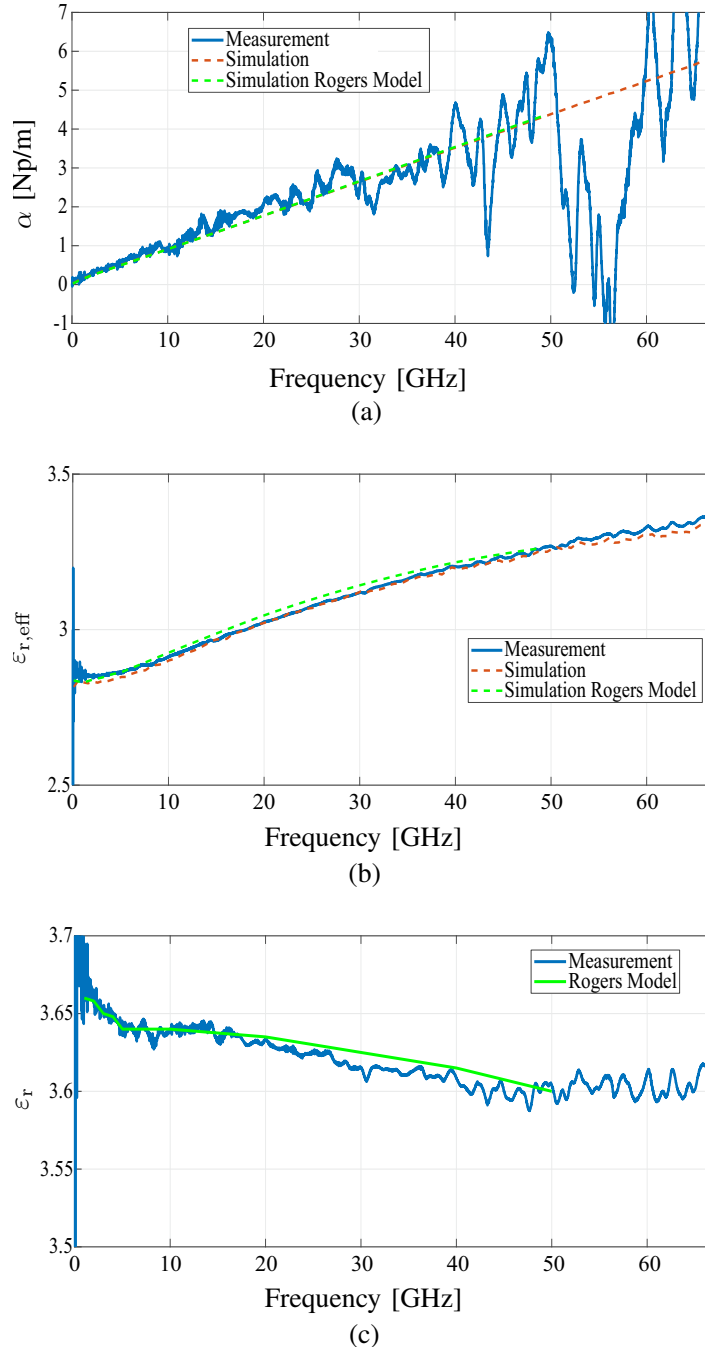
Figure 3.4: Experimental results of the propagation constant using the proposed method with 7 line lengths compared to electromagnetic simulation results. The line lengths are 2, 2.69, 3.60, 4.61, 5.68, 6.82 and 8 cm. (a) Attenuation constant. (b) Relative effective permittivity. (c) Estimated substrate permittivity.

3.3   Estimation of material parameters

The setup proposed for estimating dielectric parameters consists of a microstrip line loaded with a dielectric overlay made of the material that will be characterized. The
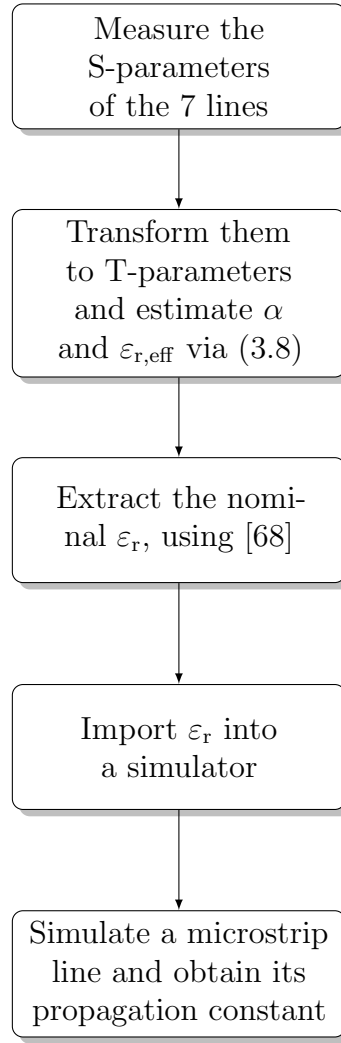
Figure 3.5: Flowchart of the lower substrate characterization.

measurement scheme is shown in Fig. 3.6. As shown, microstrip dielectric has a known permittivity ε_{r1}, estimated in the previous section, and a height h_1, whereas the overlay has an unknown permittivity ε_{r2}, and a height h_2.
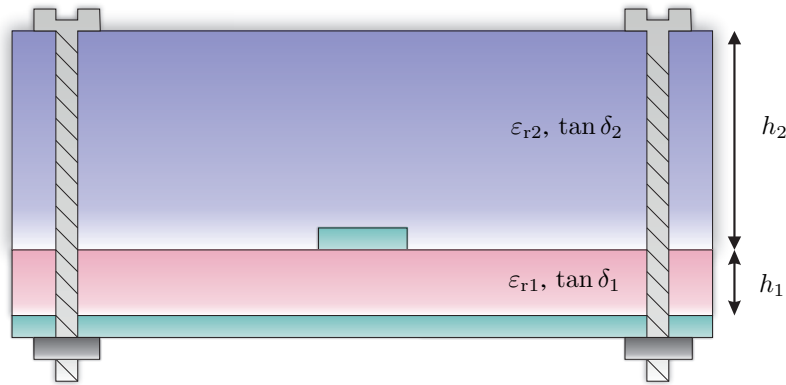
Figure 3.6: Covered microstrip lines using nylon screws for layer bonding.

The procedure consists of determining the propagation constant of the loaded microstrip and then extracting the attenuation and phase constant of the dielectric overlay. Several numerical models have been proposed to estimate the effective relative permittivity of this structure, highlighting [63, 69]. Both models are based on numerical methods and come from [70].

The problem with these methods is that the estimated relative permittivity is calculated using a quasi-static model. For that reason, they do not consider the material's own dispersion. As seen in Fig. 3.4, relative permittivity has a slight downward trend with frequency, and this trend will also appear in printing materials. For that reason, a mathematical model that characterizes this decreasing curve between the minimum and the maximum frequencies that our VNA allows us to measure will be raised. This simple curve model will be defined as

$$\varepsilon_{\mathrm{ri}} = \varepsilon_{\mathrm{r1}} - (\varepsilon_{\mathrm{r67}} - \varepsilon_{\mathrm{r1}}) \left(\frac{i-1}{N-1}\right)^{p}, i = 1, N, \qquad (3.10)$$

where $\varepsilon_{\mathrm{r1}}$ and $\varepsilon_{\mathrm{r67}}$ are the estimated relative permittivity at 1 GHz and 67 GHz respectively, and p is a quasi-linear factor. This value can be $p = 1$ for a linear model, $p = 2$ for a quadratic model or a value between these values, that will suppose a quasi-linear model. After comparing measurements and simulations, the value $p = 1.5$ shows that minimal differences are achieved, and, therefore, it is selected for this model.

3.3.1   Losses consideration

To determine $\tan \delta$ or α, the process will consist of two parts. On the one hand, it will be necessary to determine losses in conductors. For this process, the analytical model presented in [70] and improved in [71], which includes the effect of surface roughness, will be used. The surface roughness of conductors causes that losses are slightly increased. If this effect were not considered, the estimated loss tangent of the upper substrate would be higher. To verify this, some simulations have been carried out. Figure 3.7 shows the difference in the estimated attenuation constant with and without surface roughness, using HIPS as a superior substrate. As seen, surface roughness increases the slope of the estimated α. Once these losses have been considered, it is necessary to determine losses in dielectrics. This process is based on finding the $\tan \delta_{eq}$ of both dielectrics [72]. From it, knowing the loss tangent of the lower substrate $\tan \delta_1$, it is possible to obtain the loss tangent of the upper substrate $\tan \delta_2$. This method provides

an exact value of the loss tangent for the upper substrate. In addition, it allows us to distinguish between values whose tangent of losses is similar. For example, Fig. 3.8 shows the attenuation constant of three structures. The first one has a loss tangent of 0.001; the second one has 0.004, and the third one has 0.01. As seen, the slope of the attenuation constant is different. As the value of the loss tangent decreases, it will be more difficult to differentiate the values, but the method provides a fairly accurate value.
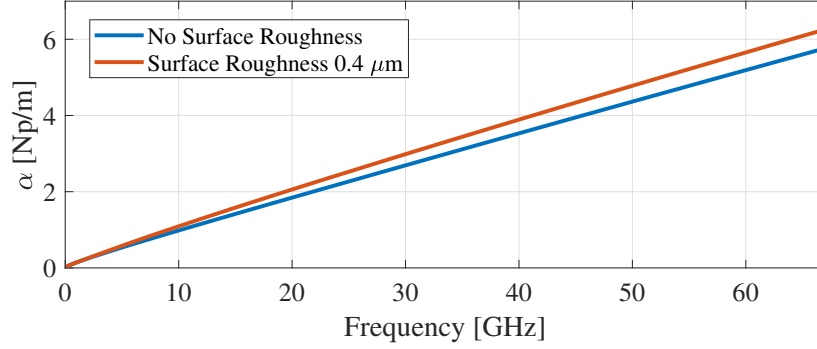
Figure 3.7: Simulated results of the attenuation constant obtained from the proposed method with 7 line lengths using HIPS as top substrate with and without metal surface roughness in the bottom substrate.
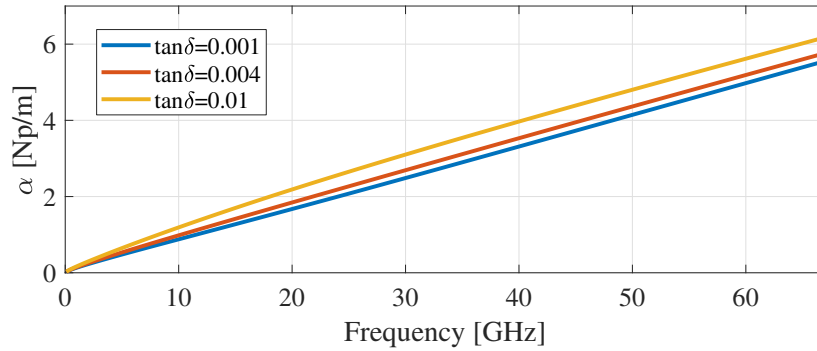
Figure 3.8: Simulated results of the attenuation constant obtained from the proposed method with 7 line lengths using three different $\tan \delta_2$.

3.4 Results

To validate the developed method, a sample of RO4350B has been made to use it as top substrate. As it is a material whose permittivity is known, it will be used to assess the method's performance. In addition, pieces of HIPS, 2 different ABS, TPU, CPE, NYLON, FLEX, PLA and PETG materials have been manufactured and measured. In the printing process, a 100% infill has been used to estimate the pure material

characteristics. If a smaller infill had been used, lower permittivities and losses would have been obtained [11] because there would be air inside the substrate. However, at this point, it is important to remark that not all printers manufacture in the same way or follow the same patterns a 100% infill, and probably there will always be a small amount of air between the sheets of the substrate. For that reason, printer and printing setup should be specified when characterizing materials.
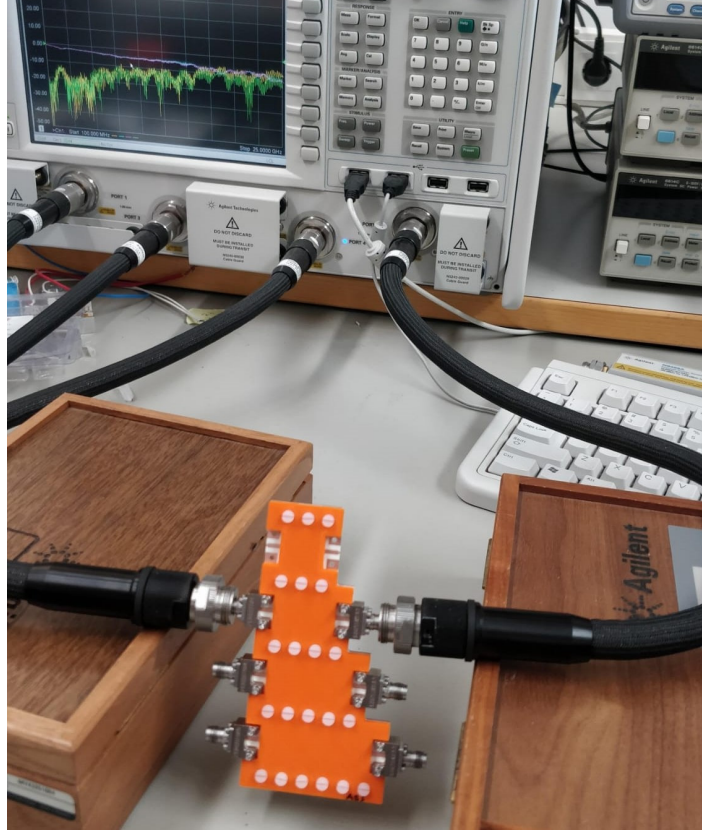
Figure 3.9: Photograph of microstrip lines covered by orange ABS and the measurement setup using Vector Network Analyzer for S-parameters measurement.

A photograph of the manufactured structure is shown in Fig. 3.9. In that Figure, it is possible to see the uncalibrated measured data on the VNA screen. The junction between the substrate and the manufactured piece is made with screws. To ensure the repeatability of the transitions and minimize errors in cable movement, the same two connectors were used for measuring all the lines, changing them for each measurement. Furthermore, a torque wrench was used to ensure that all connectors were equally tight, and a visual inspection with a microscope was made before each measurement, to ensure a correct positioning and contact. Lastly, a rigid plate was placed under the substrate to ensure that it remains utterly straight during every measurement.

The microstrip line, as well as the line lengths, are the same than the ones used

during the microstrip characterization in Section 3.2.5. S-parameters of the seven lines are taken by using the VNA Agilent PNA-X (N5247A), between 0.01 and 67 GHz. Using the EM simulator ANSYS HFSS [47], a structure as shown in Fig. 3.6 has been simulated for every material. A 0.4 μm surface roughness [73], considering the Groisse model [74], has been used for the simulations. The heights of the substrates are $h_1 = 0.762$ mm and $h_2 = 3$ mm, respectively. The gap between the substrates will cause the obtained relative permittivity to vary slightly. For this reason, some simulations have been carried out to assess this variation, using the maximum gap, which is the height of the metallization (17 μm), and the minimum gap (0 μm). The results of these simulations are depicted in Fig. 3.10. As seen, the gap works as a bias in the relative permittivity. However, the maximum difference between ε_{r2} values obtained with the gaps mentioned above is 0.35%, which means that the error made by the separation between substrates is enough to be negligible in this study.
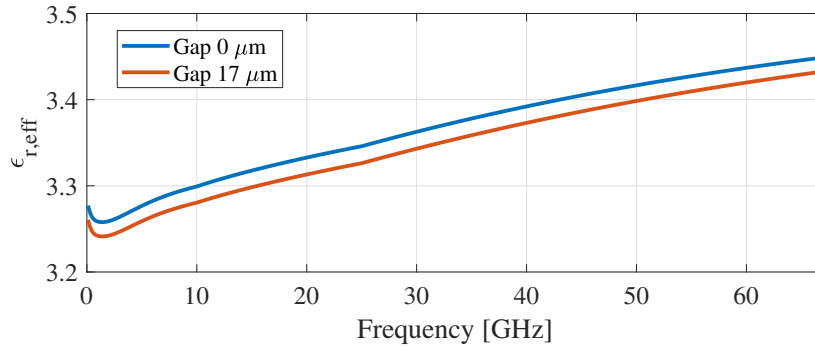
Figure 3.10: Simulated results of the effective relative permittivity obtained from the proposed method with 7 line lengths using HIPS as top substrate and two different gaps between substrates.

The dielectric permittivity of the Rogers 4350B LoPro lower substrate, used in the simulation (ε_{r1}) is the one shown in Fig. 3.4(c), that was calculated by using the proposed method. The dielectric permittivity of the printed material (ε_{r2}) for the simulation is calculated from the measured results, considering the dispersion model raised in Eq. (3.10). Specifically, the values of ε_r of the Rogers top substrate and the material samples at 1, 10, 25 and 67 GHz, as well as the $\tan \delta$ used for the simulations and the attenuation constant at 1 GHz for a plane wave are depicted in Table 3.1. As seen, results for the Rogers material are quite near to the one given by the manufacturer, shown in Fig. 3.4(c). Small differences that are less than 1%, are probably due to the small gap between both substrates or permittivity temperature dependence. Regarding printed materials, results are also similar to those found in other works [75--77], even considering that printing materials are not completely pure materials. Despite the

variety of the materials studied, they all show a relative permittivity between 2.45 and 2.95. These values are similar because the printed samples are all plastic materials manufactured with the same manufacturing process. However, there are significant differences in terms of loss tangent, which makes some materials clearly candidates for use for microwave circuits (i.e., HIPS or ABS), while others are not as suitable (i.e., flexible materials such as TPU or FLEX).

Table 3.1: Comparison between the analyzed materials.

Material	ε_r@1 GHz	ε_r@10	ε_r@25	ε_r@67	$\tan\delta$	α@1 $[dB/m]$	Δ_1	Δ_2
Rogers 4350B	3.63	3.61	3.59	3.57	0.0039	0.67	12.1×10^{-3}	6.4×10^{-3}
HIPS	2.45	2.43	2.42	2.4	0.004	0.57	5.2×10^{-3}	3.2×10^{-3}
ABS	2.67	2.65	2.63	2.61	0.009	1.34	6.9×10^{-3}	2.1×10^{-3}
TPU	2.67	2.64	2.61	2.57	0.032	4.75	16.7×10^{-3}	6.4×10^{-3}
CPE	2.8	2.78	2.77	2.75	0.013	1.98	4.9×10^{-3}	2.2×10^{-3}
NYLON	2.95	2.94	2.92	2.91	0.019	2.97	11.6×10^{-3}	5.6×10^{-3}
ABS2	2.7	2.68	2.66	2.63	0.009	1.35	6.9×10^{-3}	2.1×10^{-3}
FLEX	2.65	2.63	2.61	2.58	0.036	5.33	5.2×10^{-3}	3.2×10^{-3}
PLA	2.5	2.48	2.46	2.43	0.013	1.87	5.3×10^{-3}	2.4×10^{-3}
PETG	2.85	2.83	2.80	2.77	0.022	3.38	7.2×10^{-3}	3.1×10^{-3}

To guarantee the repeatability of the process, the printing setup, including the manufacturer of each material, the printer used, the filament size, the infill, the extrusion temperature, and the bed temperature, are shown in Table 3.2. The path of the nozzle was set to "grid", which lets the printer choose the best way to minimize manufacturing time. To validate the performance of the dispersion model in Eq. (3.10), the figure of merit Δ is defined as

$$\Delta = \frac{1}{N} \sum_{i=1}^{N} \left| \varepsilon_{\mathrm{r,eff}_i}^{\mathrm{sim.}} - \varepsilon_{\mathrm{r,eff}_i}^{\mathrm{meas.}} \right|^2, \tag{3.11}$$

where N is the number of points of the measurement and simulation. This figure of merit can be used as an estimator of the error in $\varepsilon_{r,eff}$. In Table 3.1, Δ_1 is obtained by using a simulation where dispersion is not considered, while Δ_2 is obtained by using the raised dispersion model. As seen, lower differences between measurements and simulations are achieved by using the developed model.

Figures 3.11 and 3.12 show the measured and simulated propagation constants in terms of attenuation constant and effective dielectric permittivity of the structure used for characcterization. For simplicity, considering that both pieces of ABS have similar results, only the one made by Ultimaker 3 has been depicted. As seen, an excellent agreement between measurements and simulation is achieved, highlighting the excellent accuracy in the phase constant and a good estimation of the loss tangent. Uncertainty

Table 3.2: Printing setup of each material.

Material	Manufacturer	Printer	Filament Size (mm)	Infill (%)	Extrusion temperature (°C)	Bed temperature (°C)
HIPS	Orbi-Tech	Ultimaker 3	2.85	100	235	100
ABS*	Ultimaker	Ultimaker 3	2.85	100	250	90
TPU	Ultimaker	Ultimaker 3	2.85	100	225	70
CPE	Ultimaker	Ultimaker 3	2.85	100	245	75
NYLON	Ultimaker	Ultimaker 3	2.85	100	240	70
ABS2*	Smartmaterials3D	Prusa i3 MK3	1.75	100	240	100
FLEX	Smartmaterials3D	Prusa i3 MK3	1.75	100	240	50
PLA	Smartmaterials3D	Prusa i3 MK3	1.75	100	215	50
PETG	Smartmaterials3D	Prusa i3 MK3	1.75	100	235	75

ABS* and ABS2*: These materials were manufactured with the printer
fully covered to avoid air flows that could cause delaminations.

in the measurement of the attenuation constant at high frequencies is due to the high values of the phase constant. Therefore, the errors are located in the attenuation constant, whose order of magnitude is much smaller.

Losses play a crucial role in designing structures for high-frequency applications. Although these methods are not suitable for loss characterization, the proposed overestimation and the technique to select the most appropriate line lengths allow to obtain coherent results up to 40 GHz, where fluctuations of the attenuation constant limit the available frequency range of this method. However, this frequency range is quite wider, and the obtained attenuation constant is more accurate than others in the state-of-the-art [5]. As it can be seen in Table 3.1, HIPS has a low loss tangent, $\tan \delta = 0.005$, and a low relative permittivity, $\varepsilon_r = 2.45$, if it is compared to the rest of substrates under test in this chapter. HIPS is used in numerous applications because of its easy processing, performance, and low cost [78]. The values of parameters estimated in this chapter strongly agree with published data by manufacturers [79]. This fact makes HIPS an excellent material to build support structures for circuits and antennas [62].

3.5 Conclusion

In this chapter, a simple technique to determine the broadband EM characteristics of material samples has been developed. It is very useful because of its simplicity and can be applied to both microstrip lines and lines covered with printing materials. No calibration is needed, and just the repeatability of the transitions will strongly influence the results. Furthermore, the method allows obtaining very accurate results in attenuation constant and effective dielectric permittivity by using only a few lines, whose lengths are optimized to minimize errors provoked by resonances. The achieved results show an excellent agreement between measurements and simulations, which is
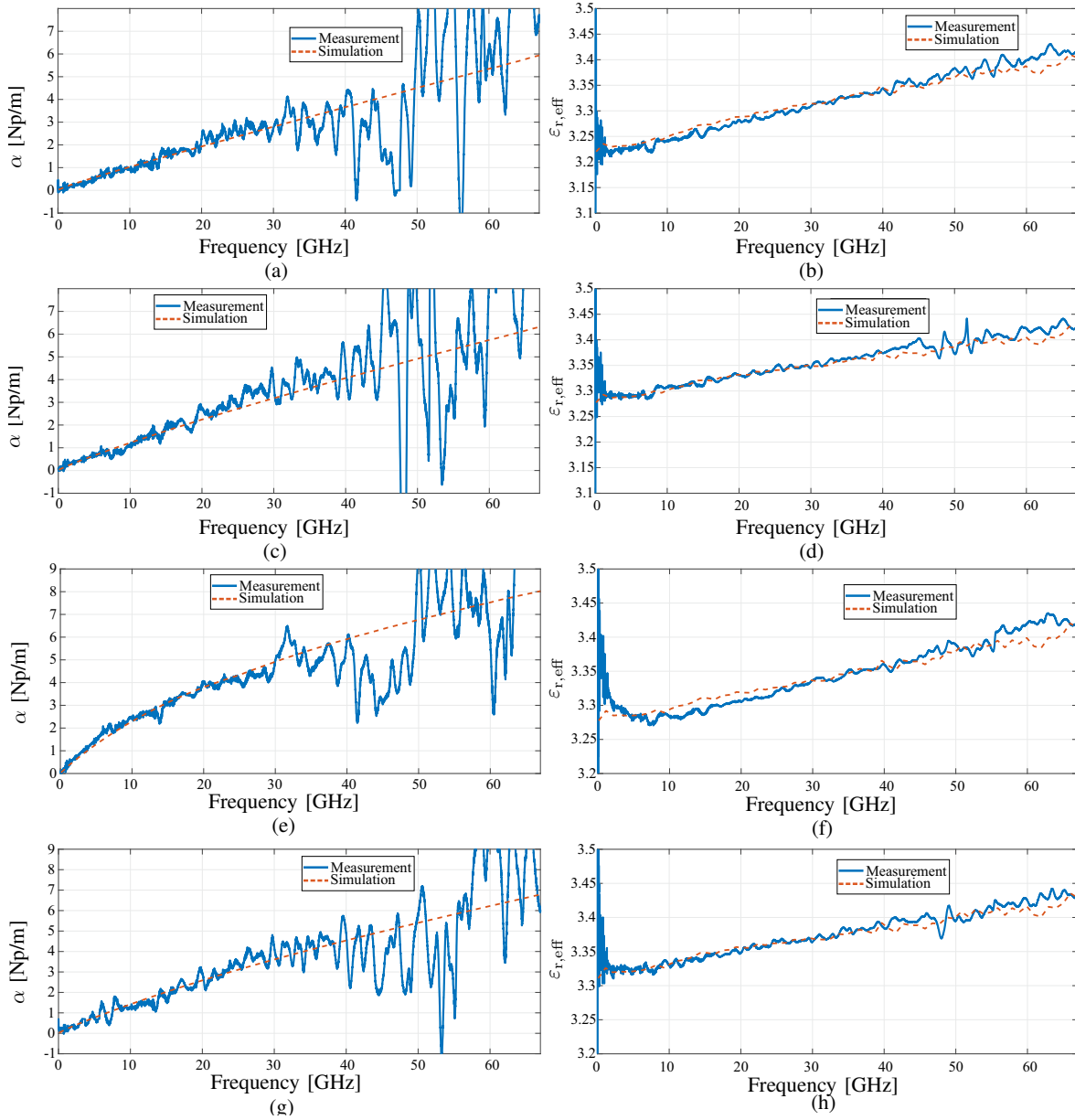
Figure 3.11: Experimental results of the propagation constant using the proposed method with 7 line lengths in comparison with electromagnetic simulation results using: (a),(b) HIPS, (c),(d) ABS, (e),(f) TPU, (g),(h) CPE.

the reason why the proposed procedure can be considered a good alternative to those found on the state-of-the-art, due to its simplicity and the accuracy of the obtained results. HIPS has demonstrated low losses and can be established as a candidate for fabrication of EM structures due to its loss tangent close to 0.004 up to 67 GHz.

The proposed method can be used for any problem with TLs or waveguides. Despite having used an indirect characterization process in this chapter based on the measurement of the S-parameters of a multilayer structure, it has been possible to achieve
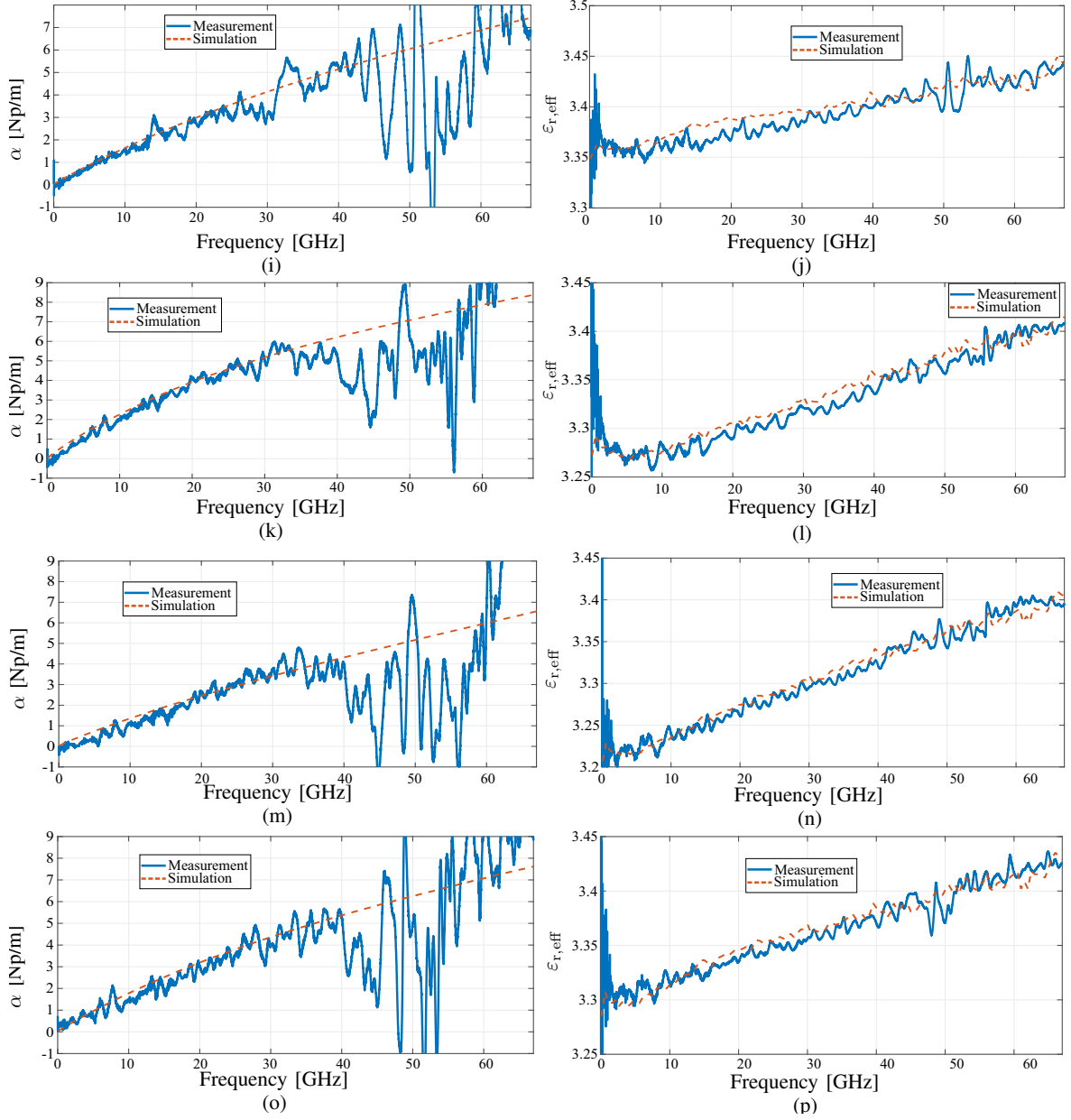
Figure 3.12: Experimental results of the propagation constant using the proposed method with 7 line lengths in comparison with electromagnetic simulation results using: (i),(j) NYLON, (k),(l) FLEX, (m),(n) PLA, (o),(p) PETG.

models that include the substrate's dispersion or metal surface roughness. However, it is important to mention that one must be careful with the gap between both substrates to ensure that the error made is very small in the relative permittivity obtained. In addition, it must be considered that the characterization carried out will take into account the characteristics of the printed material as it is, with its infill, its possible printing defects, or its manufacturing temperatures. Therefore, if any of these parameters is changed, it would be convenient to carry out a new characterization.

Chapter 4

Characterization of Multiconductor Transmission Lines

This chapter presents a broadband method to characterize the even and odd mode propagation constants of symmetrical microstrip coupled lines using four-port pure-mode differential and common mode S-Parameters. From these 4-port measurements, parameters corresponding to the even and odd modes can be extracted using mixed-mode S-parameter matrices. Differential and common mode sub-matrices will be considered as an equivalent 2-port TL, to which the proposed method will be applied to extract their propagation constants of even and odd modes. A discussion is included on ensuring the correct excitation of the modes in the structure and avoiding possible unwanted effects such as radiation, that negatively affects the results. To validate the theory presented, several sets of seven lines are manufactured. The measured results show an excellent agreement, both with EM simulations and with the analytical model used, which verifies the correct functioning of the method. In addition, the measurements are presented in the range 0.01-67 GHz, which represents a significant advance in bandwidth for this type of structures.

4.1   Introduction

Characterization techniques for symmetrical coupled TLs have been a topic of active research for years since the use of differential circuits is notably increasing in microwave technology. This particular case of MTL is widely used for several applications in the microwave and millimeter-wave frequency bands where devices such as filters [20],

power dividers [80], and directional couplers [81] are extensively used. The knowledge of the actual propagation constant of quasi-Transverse Electromagnetic (TEM) modes is of great relevance, specially for broadband applications, as well as the difference in phase velocities, and therefore, dispersion characteristics of modes propagating in the structure limit remarkably the operational bandwidth of the device.

In a pair of symmetrical coupled TLs, as depicted in Fig. 4.1, the propagation mode is a combination of the odd and even modes [82]. Several methodologies have been proposed in the literature to characterize their propagation constants. On the one hand, resonant methods [83, 84] look to force resonances in the structure, and it is possible to obtain a fairly accurate value of the propagation constant. Their main drawback is that they only offer a solution in a limited number of frequencies. On the other hand, broadband methods [5, 85] allow estimating, ideally, a solution that covers the entire frequency sweep of the VNA. However, their main inconvenience is the lack of accuracy when estimating the attenuation constant of low-loss transmission media. Extensive discussions for single mode transmission media have been done in Chapters 2 and 3.
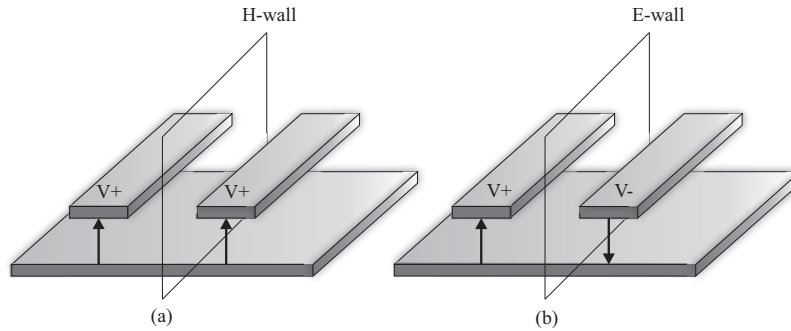
Figure 4.1: Field configuration of coupled lines even (a) and odd (b) modes.

The characterization of differential devices can be performed using a four-port VNA. In this case, two generators are used to provide differential and common mode excitation to the device under test. It is well known that this characterization is necessary for active devices due to non-linearity possible behavior. Meanwhile, for passive devices, a conventional four-port VNA is enough using the mixed-mode transformation [86]. However, in passive devices, conversion mode sub-matrices uncertainties are reduced using a pure-mode VNA [87]. From pure-mode S-parameters, in [88] it was proposed to characterize coupled microstrip lines from the TL approach model in [89]. Regarding calibration, in [13], a multimode TRL calibration, based on generalized reverse cascade matrices, was presented. In [90], multimode TRL calibration was applied for the characterization of homogeneous differential discontinuities.

This chapter deeply studies a method for accurate modeling of lossy coupled TLs over a very broad frequency band. The studied method pays special attention to the accurate characterization of attenuation constant, known as the most problematic parameter to determine using broadband methods. The procedure for measuring differential S-parameters, using a pure-mode VNA, as well as the separation of parameters of the even and odd modes are explained in Section 4.2. Section 4.3 shows the process to apply the method to each of the even and odd mode matrices to extract the propagation constant. In Section 4.4, it is discussed how the excitation of the modes influences the correct operation of the method. Section 4.5 includes the analytical, simulated, and measured results of the performed experiment to validate the presented theory. Conclusions are given in Section 4.6.

4.2   S-parameters of symmetrical coupled lines

A pair of microstrip coupled TLs deals with two independent propagation modes: the even and odd modes, as mentioned above.. A diagram of the field configuration of these modes is shown in Fig. 4.1. Their characteristic impedances, Z_{0_o} and Z_{0_e}, can be calculated analytically from the line parameters following the Kirschning and Jansen model [91]. From these characteristic impedances, the S-parameters of each mode can be computed as

$$
\begin{aligned}
S_{11_o} = S_{22_o} &= \frac{\left(Z_{0_o}^2 - Z_0^2\right)\sinh\left(\gamma_o l\right)}{2Z_0 Z_{0_o}\cosh\left(\gamma_o l\right) + \left(Z_{0_o}^2 + Z_0^2\right)\sinh\left(\gamma_o l\right)}, \\
S_{12_o} = S_{21_o} &= \frac{2Z_0 Z_{0_o}}{2Z_0 Z_{0_o}\cosh\left(\gamma_o l\right) + \left(Z_{0_o}^2 + Z_0^2\right)\sinh\left(\gamma_o l\right)}, \\
S_{11_e} = S_{22_e} &= \frac{\left(Z_{0_e}^2 - Z_0^2\right)\sinh\left(\gamma_e l\right)}{2Z_0 Z_{0_o}\cosh\left(\gamma_e l\right) + \left(Z_{0_e}^2 + Z_0^2\right)\sinh\left(\gamma_e l\right)}, \\
S_{12_e} = S_{21_e} &= \frac{2Z_0 Z_{0_e}}{2Z_0 Z_{0_e}\cosh\left(\gamma_e l\right) + \left(Z_{0_e}^2 + Z_0^2\right)\sinh\left(\gamma_e l\right)},
\end{aligned}
\tag{4.1}
$$

being γ_e and γ_o the propagation constant of even and odd modes respectively, and Z_0, the impedance of each port. However, these S-parameters can not be measured independently. Instead, what is measured is a combination of both since they are simultaneously propagated.
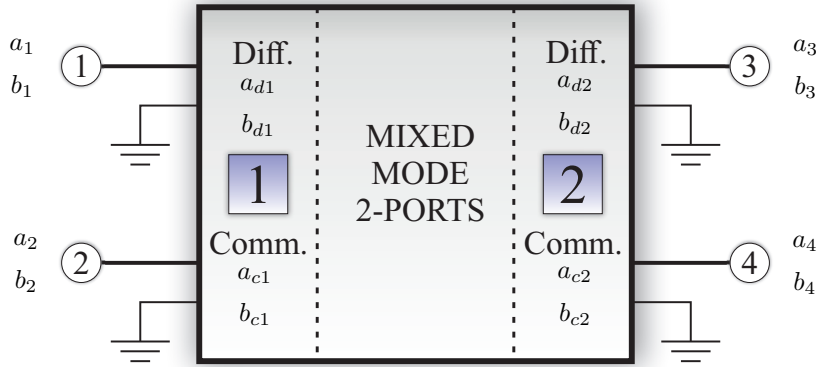
Figure 4.2: Diagram of the mixed-mode S-parameters measurement.

4.2.1   Differential S-parameters

In order to measure the S-parameters of each mode, from which its propagation constant is going to be estimated, mixed-mode S-parameters can be used. D. Bockelman and W. Eisenstadt introduced them in 1995 [92] to model differential circuits and devices. Using these parameters, it is possible to characterize more precisely the behavior of the common and differential modes of this type of devices [87]. They start from a single-ended measurement of a four-port device ($[S_{se}]$), which they transform into an equivalent device with two ports that include both the differential and common modes ($[S_{mm}]$). Figure 4.2 shows a diagram of the operation of mixed-mode S-parameter measurement, where the four single-ended ports are considered as two ports, propagating differential and common modes independently.

The single-ended S-parameters are given by

$$\begin{pmatrix} b_1 \\ b_2 \\ b_3 \\ b_4 \end{pmatrix} = \begin{pmatrix} S_{11} & S_{12} & S_{13} & S_{14} \\ S_{21} & S_{22} & S_{23} & S_{24} \\ S_{31} & S_{32} & S_{33} & S_{34} \\ S_{41} & S_{42} & S_{43} & S_{44} \end{pmatrix} \cdot \begin{pmatrix} a_1 \\ a_2 \\ a_3 \\ a_4 \end{pmatrix}, \tag{4.2}$$

whereas the mixed-mode ones are given by

$$
\begin{pmatrix} b_{d_1} \\ b_{d_2} \\ b_{c_1} \\ b_{c_2} \end{pmatrix} = \begin{pmatrix} S_{dd_{11}} & S_{dd_{12}} & S_{11_{dc}} & S_{12_{dc}} \\ S_{dd_{21}} & S_{dd_{22}} & S_{21_{dc}} & S_{22_{dc}} \\ S_{cd_{11}} & S_{cd_{22}} & S_{11_{cc}} & S_{12_{cc}} \\ S_{cd_{21}} & S_{cd_{22}} & S_{21_{cc}} & S_{22_{cc}} \end{pmatrix} \cdot \begin{pmatrix} a_{1_d} \\ a_{2_d} \\ a_{1_c} \\ a_{2_c} \end{pmatrix}.
\tag{4.3}
$$

The matrix in (4.3) can be viewed as four sub-matrices corresponding to pure differential mode (S_{dd}), pure common mode (S_{cc}), and the sub-matrices S_{dc} and S_{cd}, representing the transfer of energy between the differential and common modes. S_{dc} and S_{cd} are usually named cross-mode matrices. Matrices (4.2) and (4.3) can be related using [92]

$$
[S_{mm}] = [M][S_{se}][M]^{-1},
\tag{4.4}
$$

being

$$
[M] = \frac{1}{\sqrt{2}} \begin{pmatrix} 1 & -1 & 0 & 0 \\ 0 & 0 & 1 & -1 \\ 1 & 1 & 0 & 0 \\ 0 & 0 & 1 & 1 \end{pmatrix}.
\tag{4.5}
$$

In a way, coupled lines work as differential devices, in which the odd mode corresponds to a differential excitation, whereas the even mode to a common one, as depicted in Fig. 4.1. However, this assumption would only be entirely true if both modes had an impedance of 50 Ω. Taking into account the different impedances of the even and odd modes, the transformation to be performed is

$$
[S_{mm}] = ([M_1][S_{se}] + [M_2]) \left([M_1] + [M_2][S_{se}]\right)^{-1},
\tag{4.6}
$$

where $[M_1]$ and $[M_2]$ can be calculated following the procedure described in [93]. If the lines were uncoupled, the condition $Z_0 = Z_{0_o} = Z_{0_e}$ would be fulfilled and $[M_2] = [0]$, $[M_1] = [M]$, and therefore, Eq. (4.6) reduces to Eq. (4.4).

The cross-mode parameters should be negligible in coupled lines, so $S_{ijd} = S_{ijdc} =$

$0 \forall i, j$, and the sub-matrices can be decoupled as

$$\begin{pmatrix} b_{d1} \\ b_{d2} \end{pmatrix} = \begin{pmatrix} S_{dd11} & S_{dd12} \\ S_{dd21} & S_{dd22} \end{pmatrix} \cdot \begin{pmatrix} a_{1d} \\ a_{2d} \end{pmatrix}, \tag{4.7a}$$

$$\begin{pmatrix} b_{c1} \\ b_{c2} \end{pmatrix} = \begin{pmatrix} S_{cc11} & S_{cc12} \\ S_{cc21} & S_{cc22} \end{pmatrix} \cdot \begin{pmatrix} a_{1c} \\ a_{2c} \end{pmatrix}. \tag{4.7b}$$

These parameters will be the starting point of the proposed method for the estimation of the propagation constant: (4.7a) will be used for the odd mode and (4.7b) for the even one. Today's VNA allow measuring differential S-parameters directly, internally carrying out the transformation proposed in Eq. (4.6), provided they have the option to perform pure-mode measurements.

4.2.2   Pure-mode network analyzers

Pure-mode measurements were introduced in [94]. To perform them, it is necessary the availability of a Pure-Mode Vector Network Analyzer (PMVNA). For this type of measurement, four physical ports must be used. The main idea is to generate the four virtual ports shown in Fig. 4.2 (2 for the common mode and 2 for the differential mode). For this purpose, it must be ensured that between physical ports 1 and 2 and ports 3 and 4, there is a phase difference of 0° and 180°. If this happens, the structure is being excited in common or differential mode, respectively. From this excitation, it is possible to obtain, directly from the PMVNA the mixed-mode S-parameters matrix ($[S_{mm}]$). It is important to highlight the need for the VNA to have two different signal generators operating simultaneously. It was demonstrated that PMVNA uncertainty is lower than that of a traditional four-port VNA when measuring differential devices [87].

4.3   Method proposal

The proposed method estimates the propagation constant of 2-port TLs in broadband. It is based on the one proposed by Bianco and Parodi in [3], and extensively described previously. The key point to using it for coupled lines is to work independently with odd and even mode matrices, previously separated, measured using a PMVNA. The procedure starts with the measurement of the S-parameters of two coupled lines of different lengths. To concatenate parameters, a transformation to T-parameters is
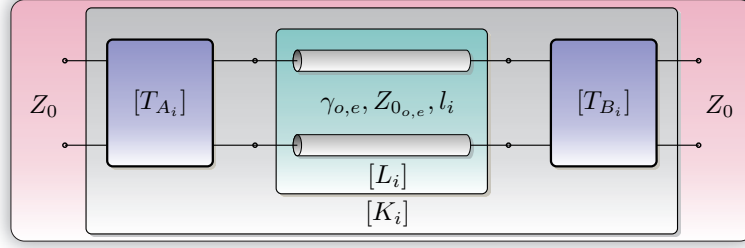
Figure 4.3: Cascade connection diagram of two-port circuits involved in the transmission line T-parameters measurement using a Vector Network Analyzer.

performed. As seen in Fig. 4.3, these parameters ($[K]$) include both the effects of the transitions ($[T]$) and those of the TL ($[L]$). In this way, K_i, that will be different for each propagation mode, can be expressed as $K_i = T_{A_i} L_i T_{B_i}$. However, this expression includes both the effects of transitions and the effect of the line. To solve this problem, a mathematical transformation must be applied to eliminate the effect of transitions. This is done by measuring lines of different lengths and using the mathematical concept of invariants [32]. Since this concept was raised, there have been several mathematical strategies to isolate the effect of the line from that of the transitions. On the one hand, there are strategies based on the calculation of traces [22] or determinants [39] of matrices. However, in [50] it was shown that the most efficient strategy was to use methods based on eigenvalues since these are the least affected by random errors. For this reason, an eigenvalue-based method will be used in this chapter. The starting point is T-parameters matrices K_1 and K_2. These matrices can be combined following

$$[K_1][K_2]^{-1} = [T_A][L_1][L_2]^{-1}[T_A]^{-1}. \tag{4.8}$$

This equation can be rewritten if matrices $[K]$ and $[L]$ are defined as $[K] = [K_1][K_2]^{-1}$ and $[L] = [L_1][L_2]^{-1}$, so (4.8) can be expressed as

$$[K] = [T_A][L][T_A]^{-1}. \tag{4.9}$$

Eq. (4.9) is a similarity transformation, so $[K]$ and $[L]$ are similar matrices and, therefore, their eigenvalues, determinants and traces coincide. Being $\gamma_{o,e} = \alpha_{o,e} + j\beta_{o,e}$ and $\Delta l = l_2 - l_1$, matrix $[L]$ is a diagonal matrix defined as

$$[L] = \begin{bmatrix} e^{+\gamma_{o,e}\Delta l} & 0 \\ 0 & e^{-\gamma_{o,e}\Delta l} \end{bmatrix}, \tag{4.10}$$

and its eigenvalues are $\lambda_1 = e^{+\gamma_{o,e}\Delta l}$ and $\lambda_2 = e^{-\gamma_{o,e}\Delta l}$. These eigenvalues coincide with those of matrix $[K]$. Therefore, the propagation constant $\gamma_{o,e}$ can be calculated using

$$\gamma_{o,e} = \frac{1}{\Delta l} \ln \left(\frac{\lambda_1 + 1/\lambda_2}{2} \right). \tag{4.11}$$

At this point, it is important to mention that if the obtained method were applied to two-port lines, it would not be required to calibrate the VNA since the effects of transitions have been eliminated by introducing the concept of invariants. A deeper discussion can be found in [50]. Although this way of obtaining the propagation constant would be sufficient under ideal conditions, the truth is that the presence of random errors due to manufacturing or the measurement system reduces the method's accuracy. That is why many authors have proposed increasing the number of lines to obtain a more precise broadband characterization. In [50], it was shown that the standard deviation of random errors decreases as the number of lines increases. To improve the precision of the method, it is proposed to use a LS fit, which is the maximum likelihood estimator for a Gaussian distribution of random errors, solving the equation

$$\min_{\alpha_{o,e}, \beta_{o,e}} \frac{1}{2} \sum_{n=1}^{N} \left| \left(\frac{\lambda_1 + 1/\lambda_2}{2} \right) - e^{+\gamma_{o,e}\Delta l} \right|^2, \tag{4.12}$$

where N is the number of lines. The lengths of these lines can be calculated considering a quasi-linear or logarithmic criterion, as explained in [50].

Regarding mixed-mode S-parameters measurement, the transformation carried out in Eq. (4.4) does not change the method behavior, since, like Eq. (4.9), both equations are similarity transformations. To validate the operation of the proposed method in an ideal case, two pairs of coupled lines, like the ones in Fig. 4.1, have been simulated in the full-wave simulator ANSYS HFSS [47]. For this purpose, it has been used Rogers 4350B substrate, with 20 mil thickness, $\varepsilon_{\mathrm{r}} = 3.66$, $\tan\delta = 0.0031$, and 17.5 μm thick copper metallization. The line widths are set to 1.095 mm, to get a 50 Ω characteristic impedance at interface ports, whereas the lengths are 10 and 35 mm, respectively. Two types of simulations have been carried out. On the one hand, a modal simulation has been used, from which the constant propagation of even and odd modes in the ports of the structure is obtained. On the other hand, a terminal simulation has been carried out in which the 4-port S-parameter matrix of the structure ($[S_{se}]$) is obtained. The transformation to differential S-parameters is applied to this matrix, obtaining the matrices of the even and odd modes, to which the proposed

method is applied. Figure 4.4 shows the results of both simulations. For ease of view, the phase constant is represented in terms of effective relative permittivity, using the transformation $\varepsilon_{r,eff_{o,e}} = (c\beta_{o,e}/\omega)^2$. As seen, both the simulated propagation constants and the ones obtained from the proposed method clearly coincide. The small differences in the attenuation constant at high frequencies are due to the port size in the simulation, being too large for those frequencies.
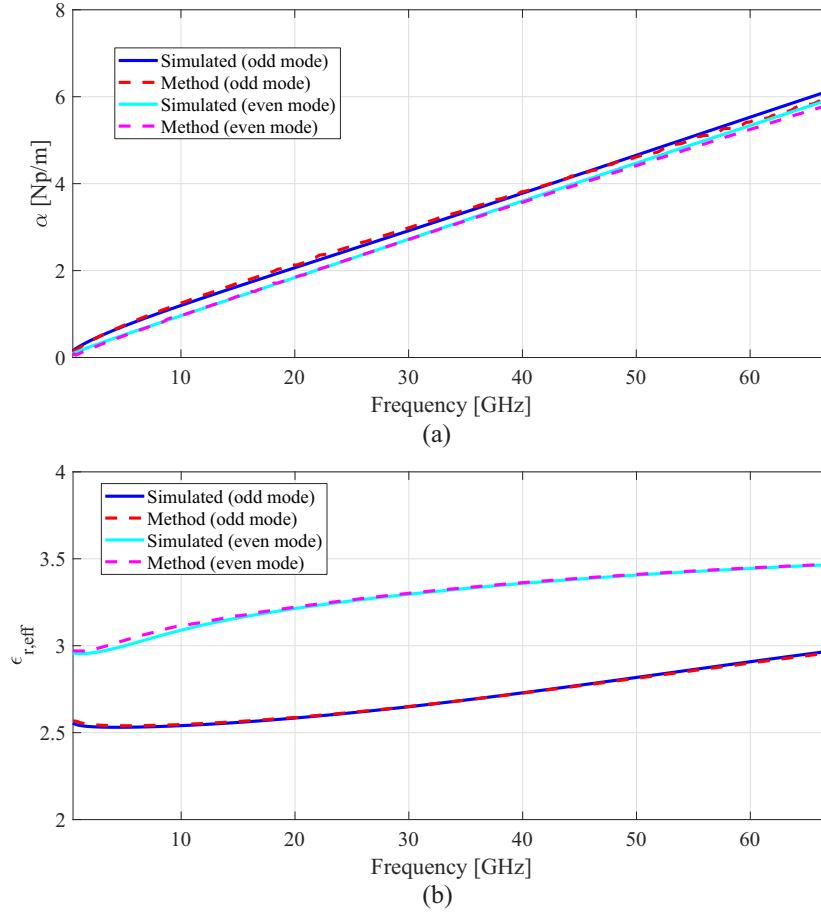
Figure 4.4: Attenuation constant (a) and effective relative permittivity (b) obtained from simulation and using the proposed method.

Results show the method's validity to obtain the propagation constant of both modes. The problem arises when trying to validate the method experimentally. It is necessary to place connectors at the end of the lines. These connectors do not fit in the configuration of two coupled lines, so it will be essential to look for a configuration based on bends that makes it possible to feed the lines. A deeper discussion will be presented in the next section.

4.4   Modes excitation
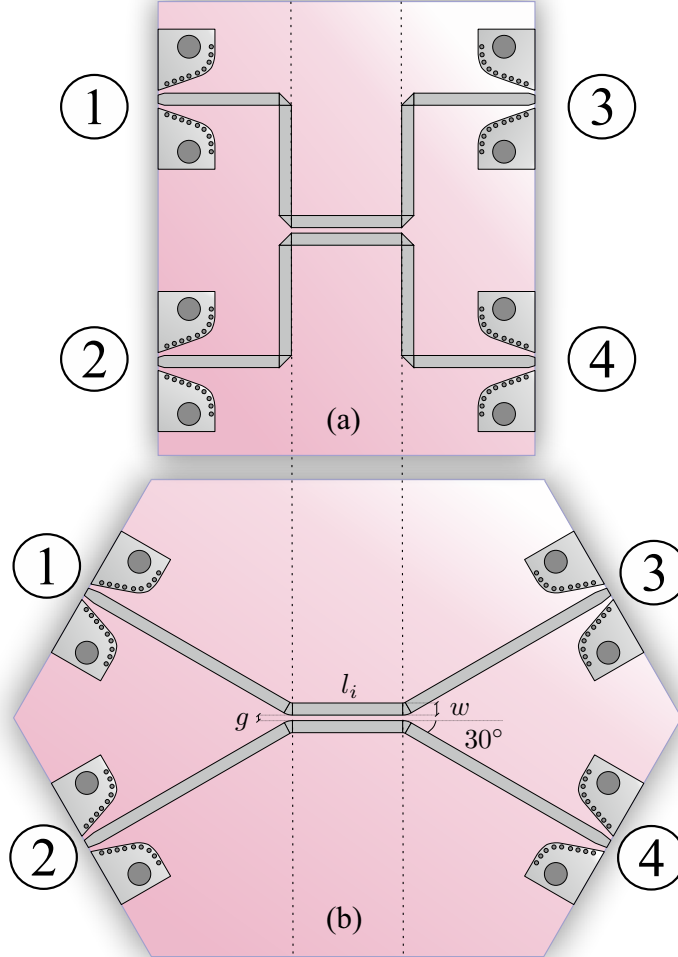
Figure 4.5: Configuration of coupled lines using 90° (a) and 30° (b) bends.

To place the connectors at the edges, it is necessary to get enough space, so they fit in the structure. For that reason, bends are used to adequately separate connectors. First, a simple structure with two 90° mitered bends for each port is proposed, as shown in Fig. 4.5(a). As all the access lines are the same, it is guaranteed that coupled lines will have a differential or common mode feed. However, for PMVNA measurements, it is necessary to use a Short-Open-Load-Through (SOLT) calibration that compensates the differences between the VNA ports to ensure that ports can have differential or common mode feeds. This is the main difference in comparison to when the proposed method is applied for single mode 2-port TLs. The main problem associated with bends is radiation losses [95]. These losses are especially significant when the angle of the

bends increases [96] and at high frequencies when the length of lines between bends is comparable with guided wavelength. For this reason, an additional configuration with only a 30° bend is proposed and depicted in Fig. 4.5(b). 30° allows a proper connection to the VNA. Lower values can be used, but 30° is a balance between admissible parasitic effects and adequate connections with reasonable lengths in access microstrip lines.

Two figures of merit are proposed to compare how the two configurations can affect the presented method, which are key to understanding how the method works. On the one hand, the attenuation constant strongly depends on the absolute value of the S-parameters [50]. To satisfy energy conservation, the equation

$$\sum_{n=1}^{N} |S_{nm}|^2 \leq 1 \ \forall m \tag{4.13}$$

must be fulfilled for each line [97]. In this sense, considering that the structure is reciprocal, and to evaluate radiation losses, indicator Δ can be defined as

$$\Delta = |S_{11_i}|^2 + |S_{21_i}|^2 + |S_{31_i}|^2 + |S_{41_i}|^2 \leq 1. \tag{4.14}$$

On the other hand, the phase constant depends on the phase difference of two lines with different lengths. For this reason, the figure δ can be defined as

$$\delta = \angle S_{31_2} - \angle S_{31_1}. \tag{4.15}$$

The two defined indicators will serve to evaluate how bends can affect the behavior of the proposed method. Figure 4.6 shows Δ and δ indicators for the 2 lines simulated in the previous section using 30° and 90° bends. As it can be seen, there is much greater power loss due to radiation when using 90° bends. This irregular behavior will cause the estimated attenuation constant to deteriorate rapidly. Bad results are expected for α even at low frequencies (Fig. 4.6). In addition, for that configuration, the phase difference does not have a linear behavior with frequency, so the phase constant will not be correctly calculated at high frequency. Therefore, 30° bends configuration is expected to make the method works better, as will be seen subsequent in measurements.
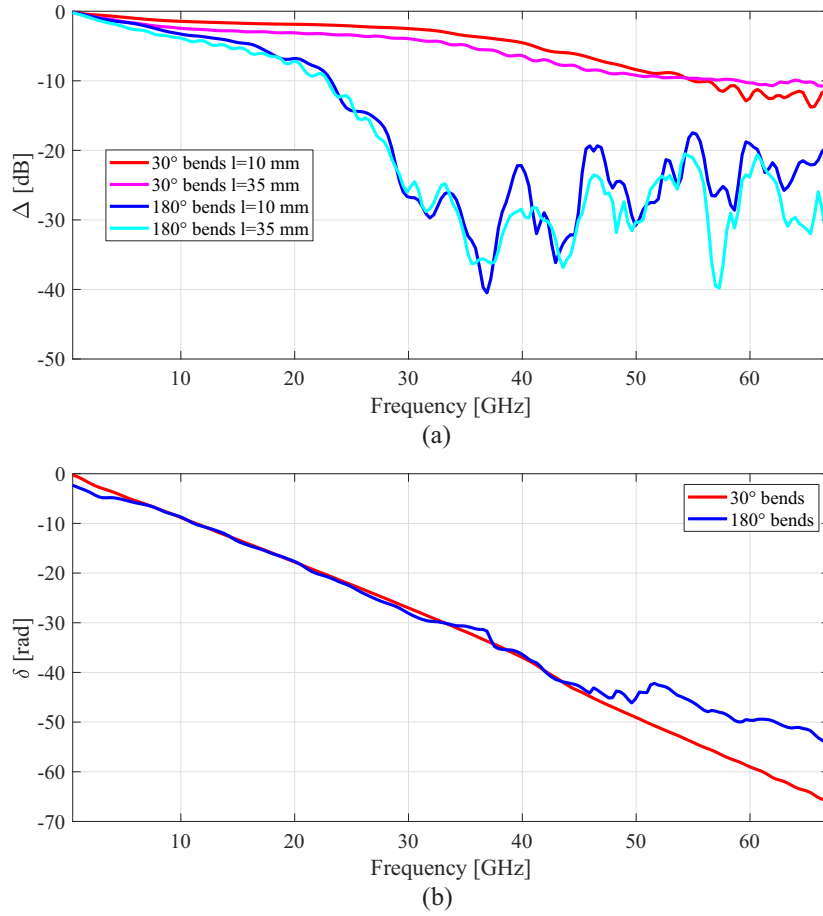
Figure 4.6: Δ (a) and δ (b) indicators using 90° and 30° bends and lines of 10 and 35 mm.

4.5   Assessment of the method

In order to assess the performance of the developed method, two experiments have been carried out. The first one consisted of 7 lines, whose lengths were chosen taking the quasi-linear (q=1.2) criteria [50] (10, 12.91, 16.69, 20.88, 25.37, 30.09, and 35 mm), and using a 30 mils high substrate. The line width was set to 1.65 mm, and the gap between lines to 0.2 mm. Initially, a structure with 90° bends was used, like the one shown in Fig. 4.5(a). This structure was manufactured and measured using the VNA Agilent PNA-X (N5247A), between 0.01 and 67 GHz. Results are depicted in Fig. 4.7. The analytical model used to compare with simulated and measured results is the one proposed by Hammerstad and Jensen in [98]. Simulated results have been obtained in the full-wave simulator ANSYS HFSS [47], using a modal simulation. The results obtained after using the proposed method have the expected behavior. On the one hand, attenuation constants give good results up to 30 GHz. From this frequency,
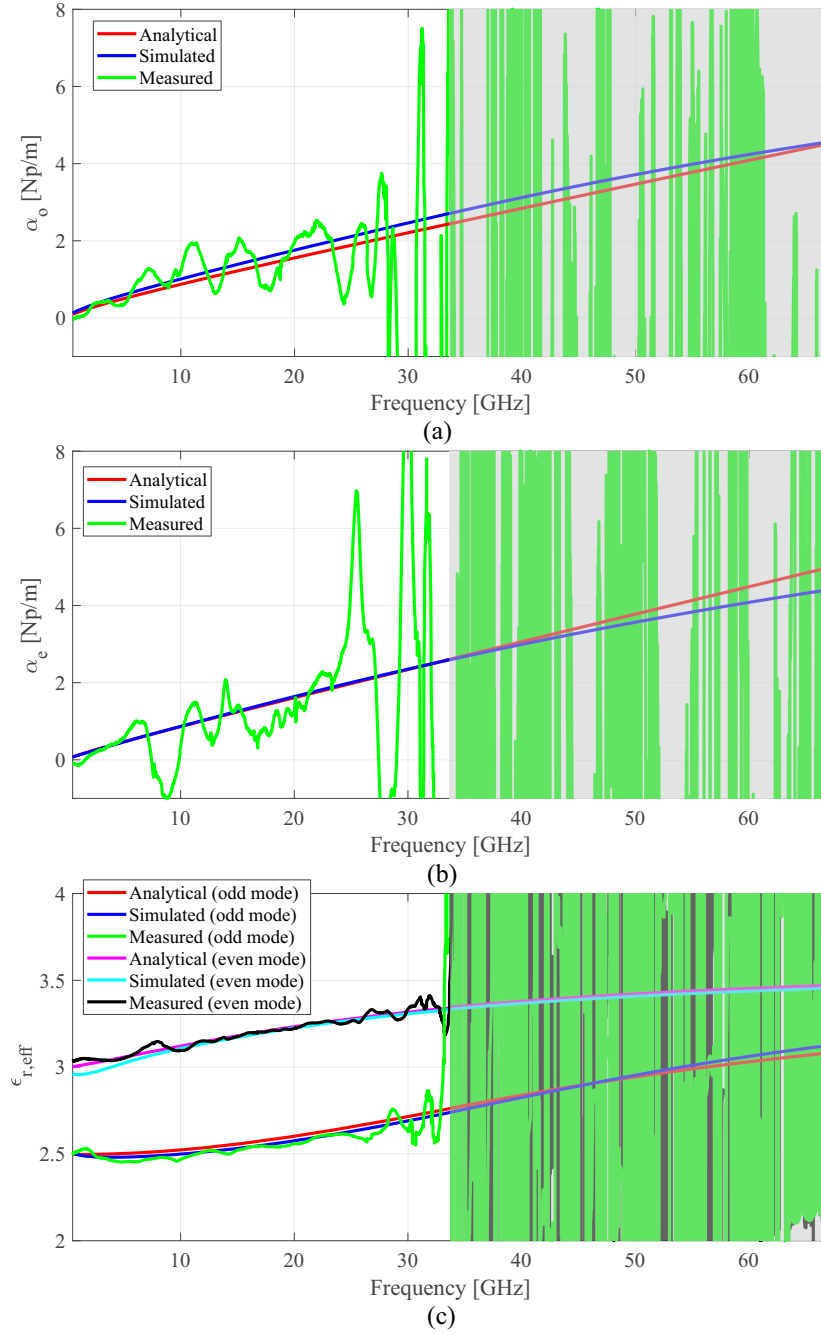
Figure 4.7: Experimental results of the attenuation constants (a)(b) and effective relative permittivities (c) using the proposed methods with 90° bends (Fig. 4.5(a)), in comparison with electromagnetic simulation and analytical model.

bends radiation provokes that a good estimation of attenuation constants at higher frequencies cannot be obtained. On the other hand, the effective relative permittivity obtained for both modes is very similar to that of the simulation and of the analytical model up to approximately 35 GHz. From this frequency, where, as seen in Fig. 4.6, the phase difference between lines is not linear, the method stop working properly and the

estimated effective relative permittivity obtained for each mode is not correct, arising a very high deviation in results.

Figure 4.8: Photograph of manufactured coupled lines and the measurement setup using Vector Network Analyzer for Pure Mode S-parameters measurement.

As mentioned above, to improve the performance of the first experiment, a second round of manufacturing, in which 30° bends are used, and the substrate is changed for the 20 mils high one, is performed. The line lengths used were the same as in the first experiment (between 10 and 35 mm), while the line width changed to 1.095 mm to ensure a characteristic impedance, Z_0, of 50 Ω in the access ports. In this case, lines with gaps of 150, 300, and 500 μm were manufactured. The same VNA as in the first experiment was used for the measurement, obtaining the S-parameters in the pure-mode configuration after a SOLT calibration. A photograph of the measurement setup is shown in Fig. 4.8. Results are depicted in Figs. 4.9, 4.10, and 4.11. The analytical and simulated models are the same as in the previous case. The differences between these models in the attenuation constant are because the model proposed in [98] is

not valid for very tight couplings. As seen, the accuracy of the obtained attenuation constant is greater, and the bandwidth of the method. Regarding the effective relative permittivity, the results obtained are highly accurate, similar to those of the analytical and simulated models. Excellent results for the phase constant have been obtained in the full measured bandwidth. Using 30° bends allows a significantly better performance of the method. The attenuation constant is very sensitive to measurement errors in S-Parameters, and it deteriorates as the coupling coefficient increases. This is due to the measured cross-mode matrices, whose values are not negligible when the gap between lines decreases and frequency increases.

4.6   Conclusion

This chapter presents a method to obtain the even and odd modes propagation constant of microstrip coupled lines from 4-port pure-mode S-parameters measurements. The method uses the measures of different length coupled lines. It allows obtaining excellent results, in comparison with the analytical and simulated models, in both the phase and the attenuation constants over the entire measurement bandwidth (0.01-67 GHz). Furthermore, the results of the attenuation constant significantly improve those obtained using other methods proposed in the state-of-the-art. In this sense, a study has been performed, showing that reducing the angle of the bends improves the excitation of the modes since radiation is drastically reduced, causing the result of the attenuation constant to be considerably enhanced and the bandwidth of the phase constant extended. The experimental validation has served to assess the theory presented, showing very accurate results throughout the entire bandwidth of the VNA used. Therefore, it can be concluded that, despite its simplicity, the presented method allows obtaining the propagation constant quite accurately.
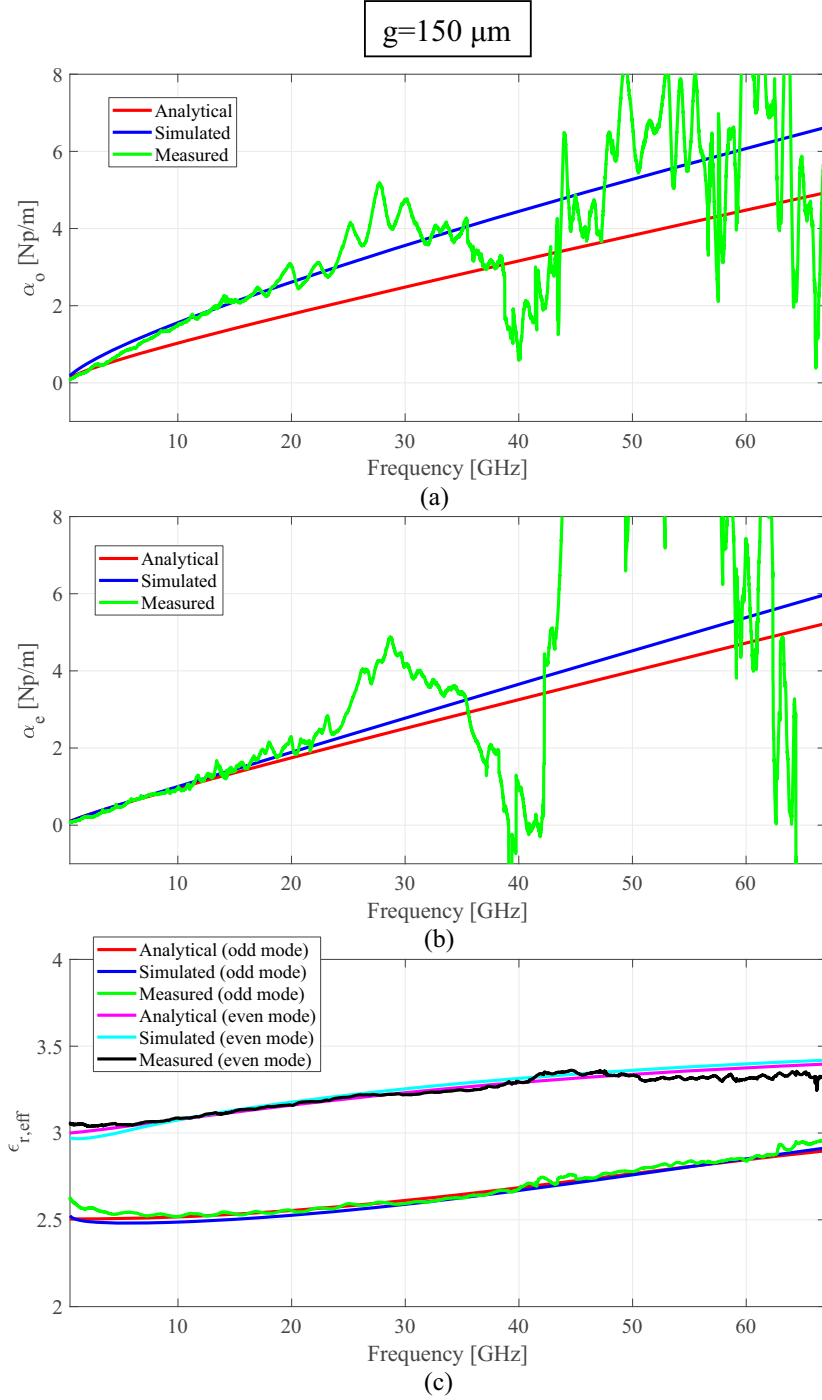
Figure 4.9: Experimental results of the attenuation constants (a)(b) and effective relative permittivities (c) using the proposed methods with 30° bends (Fig. 4.5(b)), for $g = 150$ μm, in comparison with electromagnetic simulation and analytical model.
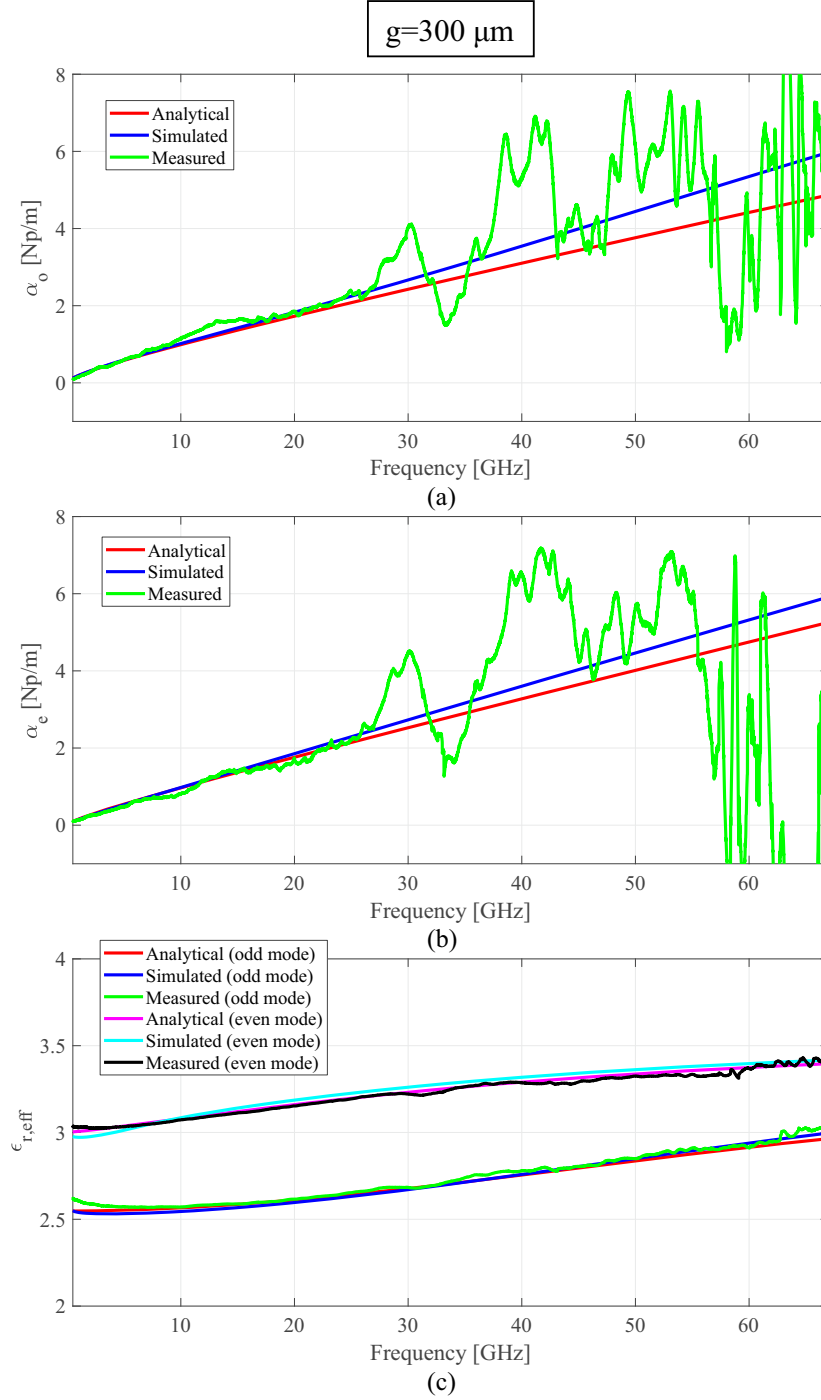
Figure 4.10: Experimental results of the attenuation constants (a)(b) and effective relative permittivities (c) using the proposed methods with 30° bends (Fig. 4.5(b)), for $g = 300~\mu$m, in comparison with electromagnetic simulation and analytical model.
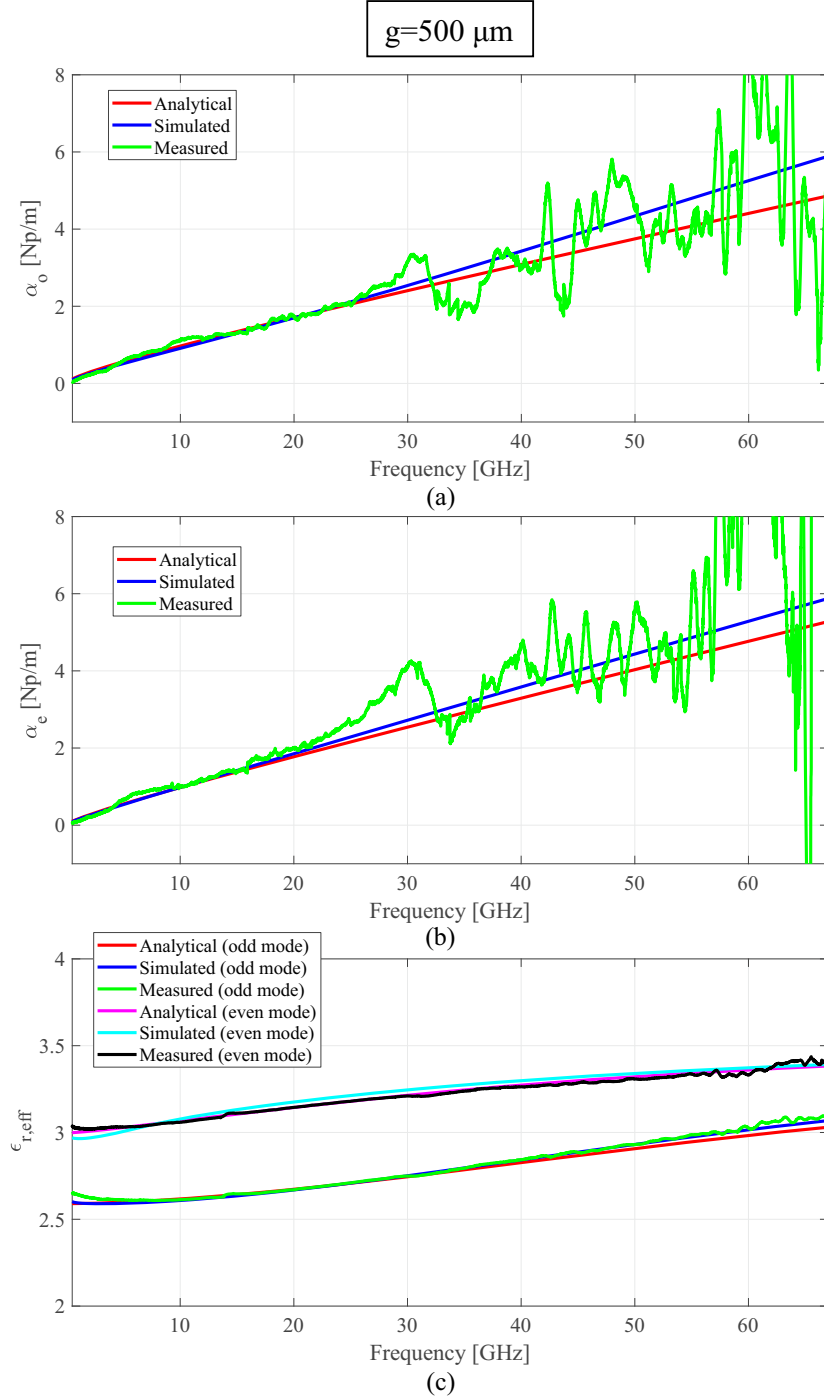
Figure 4.11: Experimental results of the attenuation constants (a)(b) and effective relative permittivities (c) using the proposed methods with 30° bends (Fig. 4.5(b)), for $g = 500$ μm, in comparison with electromagnetic simulation and analytical model.

Chapter 5

Multi-band Filter Design Using Multiconductor Transmission Lines

The design of dual-band and multi-band BPFs consisting of series short-circuited wire-bonded MTLs and shunt open stubs is thoroughly carried out in this chapter. Three different configurations are studied, and closed-form analytical design equations are derived to synthesize Chebyshev filtering functions. A novel, simplified and time-saving synthesis procedure to design dual-band filters with narrow or moderate broad bandwidths is finally presented, attending to the required final specifications and the physical and manufacturing limitations. If the number of stubs increases, it is possible to achieve multi-band bandpass responses. The usefulness and validity of the proposed analytical equations are illustrated by designing, manufacturing, and measuring four different prototypes, showing an excellent agreement between analytical and measured results.

5.1   Introduction

Nowadays, the enormous growth of data traffic is promoting new solutions used to transport this high amount of data. Different techniques, such as Multiple-input Multiple-output (MIMO) systems, multicarrier, or carrier aggregation, are used to satisfy this demand. Nevertheless, not only is signal processing important to achieve high data rates, but also every part of the communication system can be enhanced. In the RF domain, many improvements are utilized, such as the use of wider, double, or triple band systems [99, 100]. In this sense, BPFs are one of the most essential components,

and multi-band responses have become crucial in the design of RF circuits [101, 102].

The main issue of dual-band filters is that they must be designed and optimized for diverse specifications and applications, which could need broad or narrow bandwidths, large or small frequency ratios, and different in-band ripple factors or return losses. Different topologies have been proposed to achieve these specifications. The most straightforward ways of designing dual-band filters is by cascading two single-band filters [103] or combining a wideband filter with a bandstop filter [104]. These methods are the simplest, but they usually have insertion losses and circuit size problems. For that reason, the main topologies proposed by researchers are based on the multimode resonators. These filters can be implemented in different shapes and topologies, including open-loop resonators [105, 106], ring resonators [107, 108], stepped-impedance resonators [109, 110] or quadruple-mode resonators [111]. Furthermore, the coupling between adjacent resonators is normally complicated, and there is a strong dependence on full-wave simulations to characterize it. Therefore, the time spent in the design and optimization process of filters based on resonators is usually large. Transmission or coupled lines are also quite used in planar dual-band BPFs, both in single-layer [112, 113] as in multilayer technologies [114, 115]. Under certain conditions, as proposed in this chapter, it is possible to obtain analytical design expressions, even without the use of EM simulators. Apart from that, mathematical transformations from single-band to multi-band filters have been proposed to synthesize multifrequency responses from single ones [116].

Sometimes, services and applications as IoT devices demand multifrequency bands simultaneously. For that reason, researchers are also focused on how to achieve more than two band elements, especially for communication systems, such as antennas [117], amplifiers [118] or filters [119]. Concretely, and related to this chapter, many RF and microwave applications need compact filters with low losses and multi-band operation. In recent years, there is a research group that stands out for having proposed different technologies to create multi-band responses, including filters based on Acoustic-Wave-Lumped-Element-Resonators [120], Evanescent-Mode-Cavity-Resonators [121], and differential [122] or split-type filters [123]. Coupled lines have been used traditionally in many applications to develop filters with appropriate frequency responses. One of their most important advantages is that, normally, an analytical model allows designers to control the main parameters of the filters. When increasing the number of fingers in MTLs, a great variety of responses can be obtained because there is a greater range of impedance and coupling factor values that can be achieved. This is only possible as the

coupled lines are alternatively interconnected with wire-bondings to eliminate undesired TEM modes inherent to multiconductor structures. In this sense, MTLs have been used successfully for synthesizing wide and Ultra Wide Band (UWB) differential [12] or dual-band BPFs [124].

In this chapter, two topologies of dual-band and a topology of multi-band planar BPFs based on series short-circuited MTLs and shunt open stubs are proposed and analyzed through analytical equations. Using the proposed architectures, dual-band or multi-band filters with one or two poles in each band can be achieved. As one of the main contributions, new design equations to synthesize filters with a Chebyshev-type response employing a quick and reliable procedure are deduced. With this configuration, filters parameters can be controlled by varying the even and odd mode impedances and the electrical lengths of the MTLs and the stubs. Additionally, and to improve out-of-band frequency response, wire-bondings have been added in the middle of the MTLs, whereas two spur-line filters are used to mitigate the first replica of the filter frequency response.

This chapter is structured as follows. First, in Section 5.2.1, circuit analysis of the first two presented topologies is carried out to characterize the behavior of both topologies separately. Subsequently, dual-band filtering functions and a transformation between frequency and electric length domains are presented in Section 5.2.2. By using such transformations, a synthesis procedure and a complete set of analytical equations for the design of Chebyshev-type dual-band filters are obtained in Section 5.2.3. A design methodology, taking into account the limitations of the filter, is proposed in Section 5.3. In Section 5.4 an additional configuration that allows obtaining multi-band responses is proposed. Finally, in Section 5.5, experimental validation is carried out by designing, fabricating, and measuring four filters, corroborating the developed theory and techniques. Conclusions are given in the Section 5.6.

5.2   Analytical design procedure

In this section, the first two circuit topologies, shown in Fig. 5.1, have been analyzed. The procedure used to analyze these circuits is similar to the one in [125--129]. Firstly, the frequency response of the circuits is computed (i.e., the S_{21} parameter). Then, a proper filtering function for synthesizing dual-band BPFs is obtained, and finally, the circuit design parameters are determined by equating the transfer functions to the filtering functions. Through this procedure, closed-form analytical design equations are

obtained to design dual-band BPFs with known return losses and operating bandwidths.

5.2.1 Circuit analysis
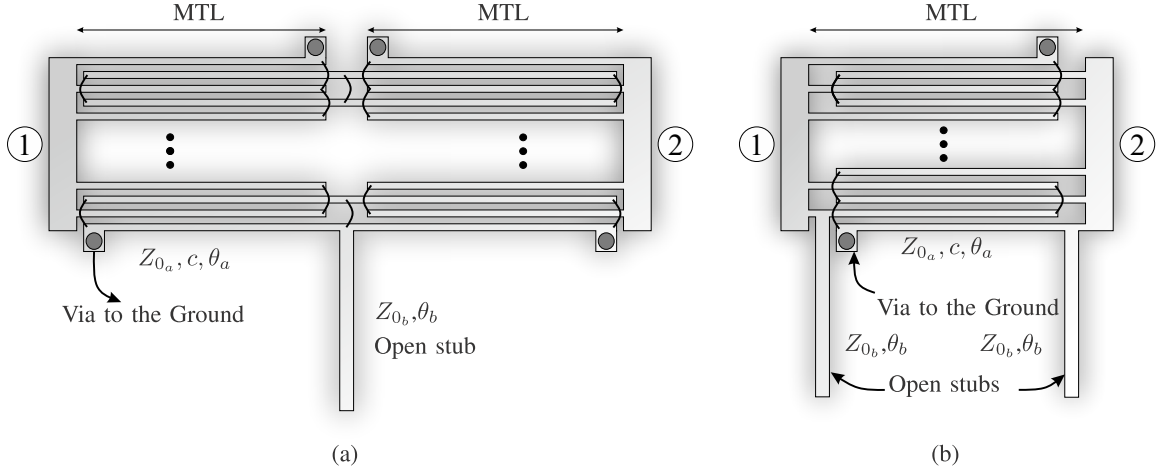
Figure 5.1: Layout of the proposed circuit for the analyzed dual-band bandpass filters: (a) prototype I and (b) prototype II.

The proposed circuits (see Fig. 5.1) are composed of series short-circuited MTLs and shunt open-circuited stubs. Two symmetrical prototypes are considered to design first- and second-order dual-band BPFs. The analysis of both filters can be directly carried out by using the equivalent circuit for a short-circuited MTL [130], consisting of a TL section and two shunt short-circuited stubs with characteristic impedances Z_{0_a} and Z_{sc_a}, respectively. The equivalent circuit models based on TL for both prototypes are depicted in Fig. 5.2. On the one hand, the characteristic impedances of the MTL, Z_{0_a} and Z_{sc_a}, are given by

$$Z_{0_a} = \frac{2}{(k-1)(Y_{oo} - Y_{oe})} = \frac{2Z_{oe}Z_{oo}}{(k-1)(Z_{oe} - Z_{oo})} \tag{5.1a}$$

$$Z_{sc_a} = Z_{oe}\left(1 + \frac{(k-2)Z_{oo}}{Z_{oe} + Z_{oo}}\right)^{-1} = Z_{0_a}\frac{c}{1-c}, \tag{5.1b}$$

where Z_{oe} and Z_{oo} denote the even- and odd-mode impedances of a pair of coupled lines, and k is the number of conductors. θ_a is the electrical length of a MTL, computed as the arithmetic mean value of the even- and odd-mode electrical lengths, and c is related to the maximum coupling coefficient of a k-lines quarter-wavelength four-port
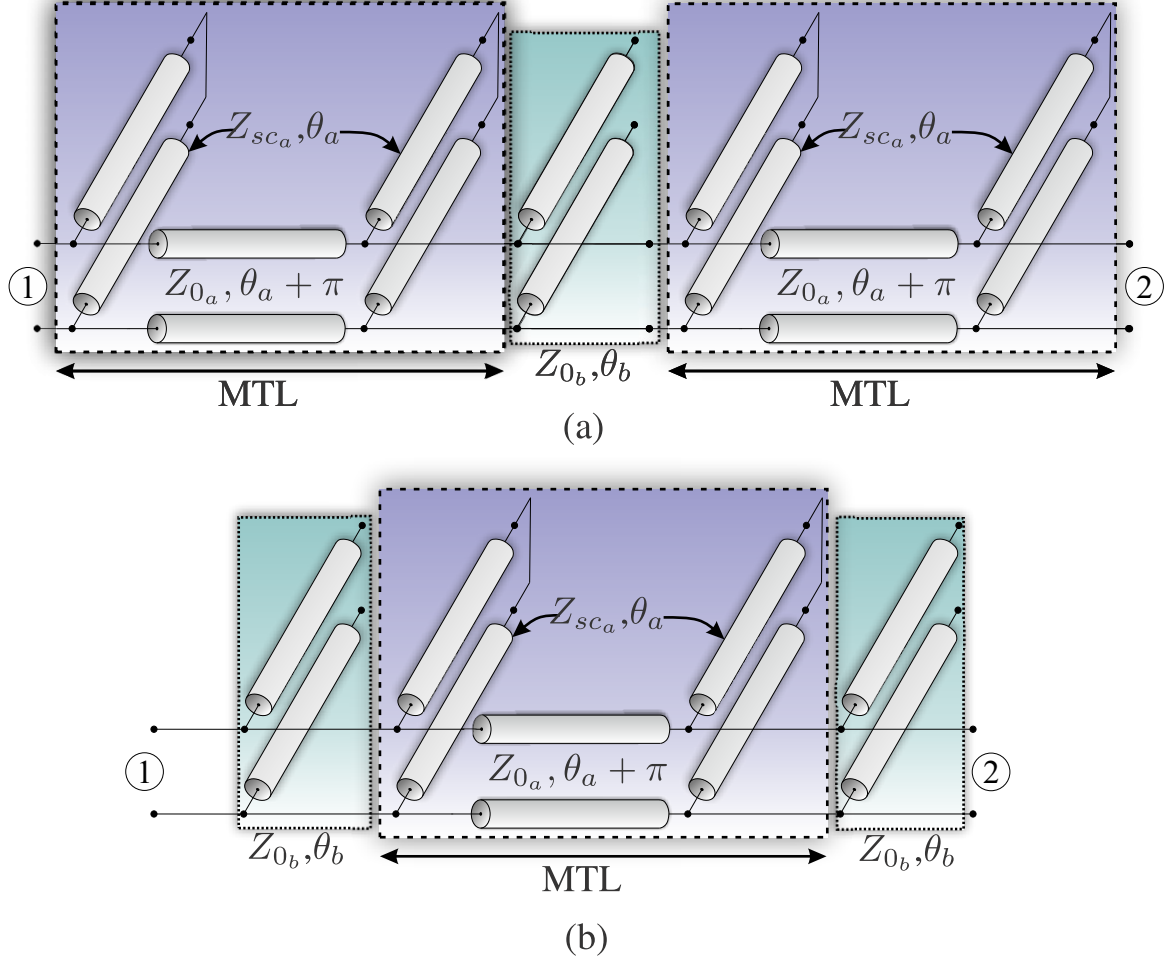
Figure 5.2: Equivalent circuit model for the proposed filters: (a) prototype I and (b) prototype II.

coupler [131], which can be written as

$$c = \frac{Z_{oe} - Z_{oo}}{Z_{oe} + Z_{oo}} \left(1 - \frac{(k-2)2Z_{oe}Z_{oo}}{(k-1)(Z_{oe} + Z_{oo})^2} \right)^{-1}. \tag{5.2}$$

On the other hand, the open-circuited stubs are defined by their characteristic impedance Z_{0_b} and their electrical length θ_b.

To analyze these circuits, the even- and odd-mode analysis is employed. Once the even- (Z_{in_e}) and odd-mode (Z_{in_o}) input impedances are calculated, the S-parameters of the filters are determined as

$$S_{11} = \frac{Z_{in_e} Z_{in_o} - Z_0^2}{\Delta}, \quad S_{21} = \frac{Z_0 \left(Z_{in_e} - Z_{in_o} \right)}{\Delta}$$
$$\Delta = Z_0^2 + Z_0 \left(Z_{in_e} + Z_{in_o} \right) + Z_{in_e} Z_{in_o}, \tag{5.3}$$

being Z_0 the characteristic impedance used to terminate the input and output ports. These expressions can be simplified because both, the wire-bonded MTL and the open stubs, are chosen to be a quarter-wavelength long at the middle frequency (f_o) of the desired two passbands. Besides, assuming a TEM propagation, it can be considered that

$$\theta_a = \theta_b = \theta = \theta_o \frac{f}{f_o} = \frac{\pi}{2} \frac{f}{f_o}. \tag{5.4}$$

From (5.3), and after some algebraic transformations, the squared magnitude of S_{11} and S_{21} can be expressed as

- Prototype I

$$|S_{11}|^2 = \frac{F_I^2}{1 + F_I^2}, \quad |S_{21}|^2 = \frac{1}{1 + F_I^2} \tag{5.5a}$$

$$F_I = \frac{g_4 \tan^4 \theta + g_2 \tan^2 \theta + g_0}{\tan \theta \left(1 + \tan^2 \theta\right)} \tag{5.5b}$$

$$K_I = \frac{1}{2c^3 \bar{Z}_{0_a} \bar{Z}_{0_b}} \tag{5.5c}$$

$$g_4 = \bar{Z}_{0_a}^3 c^3 K_I \tag{5.5d}$$

$$g_2 = \left(\bar{Z}_{0_a} c + 2\bar{Z}_{0_b} c^2 \left(1 - \bar{Z}_{0_a}^2\right)\right) K_I \tag{5.5e}$$

$$g_0 = -2\bar{Z}_{0_b} \left(1 - c^2\right) K_I \tag{5.5f}$$

- Prototype II

$$|S_{11}|^2 = \frac{F_{II}^2}{1 + F_{II}^2}, \quad |S_{21}|^2 = \frac{1}{1 + F_{II}^2} \tag{5.6a}$$

$$F_{II} = \frac{p_4 \tan^4 \theta + p_2 \tan^2 \theta + p_0}{\tan^2 \theta \left(1/ \sin \theta\right)} \tag{5.6b}$$

$$K_{II} = \frac{1}{2c^2 \bar{Z}_{0_a} \bar{Z}_{0_b}^2} \tag{5.6c}$$

$$p_4 = \bar{Z}_{0_a}^2 c^2 K_{II} \tag{5.6d}$$

$$p_2 = - \left(2\bar{Z}_{0_a} \bar{Z}_{0_b} c + \bar{Z}_{0_b}^2 c^2 \left(1 - \bar{Z}_{0_a}^2\right)\right) K_{II} \tag{5.6e}$$

$$p_0 = \bar{Z}_{0_b}^2 \left(1 - c^2\right) K_{II} \tag{5.6f}$$

where

$$\bar{Z}_{0_a} = Z_{0_a}/Z_0, \quad \bar{Z}_{0_b} = Z_{0_b}/Z_0. \tag{5.7}$$

The frequency response of both structures is perfectly characterized by means of (5.5) and (5.6), and taking into account the form of F_I and F_{II}, designing dual-band BPFs with real transmission zeros at $\theta_z = z\frac{\pi}{2}$ and $z = 0,1,2,...$ is possible. These transmission zeros are used to enhance both the isolation between two passbands and the rejection level in the lower and upper stop-bands. The transmission zeros at $\theta_z = z\frac{\pi}{2}$, $z = 0,2,4,...$ are inherent to the series MTL, while the zeros at $\theta_z = z\frac{\pi}{2}$, $z = 1,3,...$ are caused by the open stubs. Moreover, because of the degree of the numerator of F_I and F_{II} is four, both structures are, a priori, suitable to synthesize fourth-order dual-band bandpass filters. By adding different electrical length stubs, it could be possible to obtain multi-band bandpass responses, forcing zeros in the MTL passband. Notwithstanding, this feasibility will depend on the physical realizability of the required values of Z_{0_a}, Z_{0_b}, and c, which also conditions the operating bandwidths and the passband frequency ratio. This configuration will be further explored in Section 5.5.

Therefore, at this point, it is important to highlight the advantages of using MTLs instead of only a pair of coupled lines. The achievable values of Z_{0_a} and c as a function of the line width W and spacing S for several numbers of conductors k are shown in [12]. These curves were calculated using the Rogers 4350B substrate with a dielectric constant of 3.66 and a thickness of 30 mils, used throughout this Ph.D. thesis. It is straightforward to observe that by increasing the number of conductors, it is possible to reduce the value of Z_{0_a} with higher coupling values (c), which can be directly translated into wider bandwidths and higher frequency passbands ratios. This behavior will be examined in Section 5.3.

5.2.2 Dual-band filtering functions

Given the transfer functions of the two configurations analyzed (5.5), (5.6), it is necessary to compute suitable filtering functions to synthesize the dual-band frequency responses properly. These functions have to be symmetric concerning the middle design frequency f_o, with one or two transmission zeros at $\theta = \theta_0 = \pi/2$. Two procedures are explored to calculate such filtering functions. The first one uses a classical low-pass Chebyshev prototype [132, 133] with a dual-band frequency transformation (Fig. 5.3(a)) [116, 134], while the latter makes use of a generalized Chebyshev prototype [135] with the well-known Richard's transformation (Fig. 5.3(b)) [127]. Nevertheless, it is important to know the limitations or particularities of both methodologies. Using the first method, a dual-band filter of order $2m$ will have m coincident transmission zeros in the middle

of the two passbands (θ_0), while through the generalized Chebyshev prototype, the number of zeros at θ_0 will be one or an odd number.
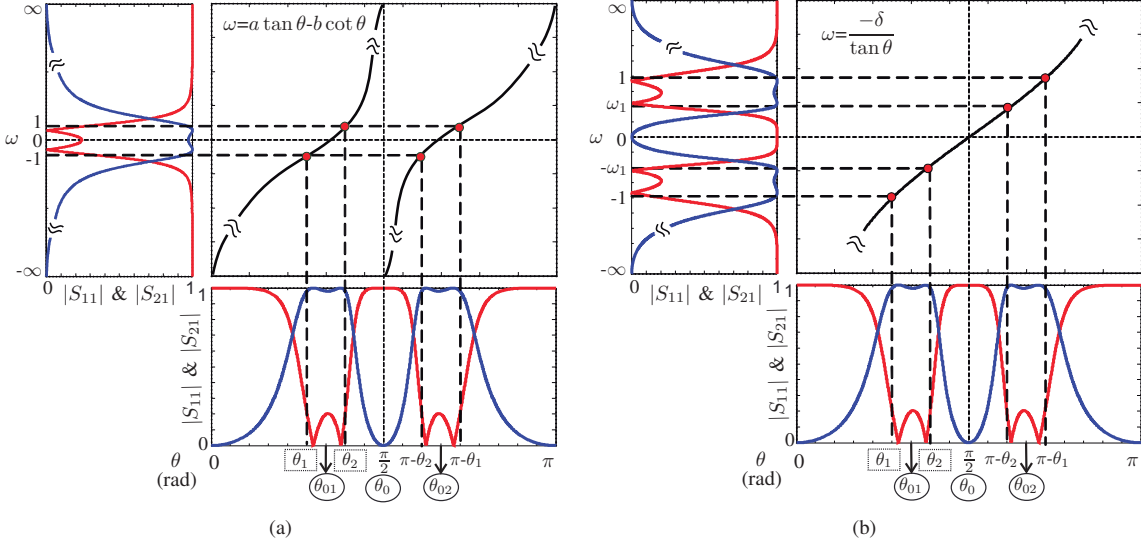
Figure 5.3: Transformations from the normalized ω-plane to the θ-plane using a (a) conventional low-pass Chebyshev prototype or (b) a generalized Chebyshev polynomial.

As seen in Fig. 5.3, the filtering functions in the normalized frequency ω corresponds to a conventional low-pass prototype (Fig. 5.3(a)) or a filter with two pass bands symmetrical respect to $\omega=0$ (Fig. 5.3(b)). θ_1, θ_2, π-θ_2 and π-θ_1 relate to the lower and upper cut-off frequencies of the two pass bands with central frequencies given by θ_{01} and θ_{02} (being θ_{02}=π-θ_{01}). By considering the desired Fractional Bandwidth (FBW) of the first band (FBW) and the central frequencies of the dual pass bands (f_{01}, f_{02}), the required design parameters θ_1 and θ_2 are obtained as

$$f_o = \frac{f_{01} + f_{02}}{2}, \quad \text{FBW} = \frac{f_2 - f_1}{f_{01}} = \frac{\theta_2 - \theta_1}{\theta_{01}},$$

$$\theta_0 = \pi/2, \quad \theta_{01} = \frac{\pi}{2}\frac{f_{01}}{f_o}, \tag{5.8}$$

$$\theta_1 = \theta_{01}\left(1 - \frac{\text{FBW}}{2}\right), \quad \theta_2 = \theta_{01}\left(1 + \frac{\text{FBW}}{2}\right),$$

and the frequency transformations can be calculated as

- Conventional low-pass Chebyshev prototype [132] to dual-band Bandpass filter

(BPF)

$$\omega = a \tan \theta - b \cot \theta \tag{5.9a}$$

$$a = \frac{1}{\tan \theta_2 - \tan \theta_1}, \quad b = \frac{\tan \theta_1 \tan \theta_2}{\tan \theta_2 - \tan \theta_1} \tag{5.9b}$$

- Generalized low-pass Chebyshev prototype [135] to dual-band BPF

$$\omega = \frac{-\delta}{\tan \theta}, \quad \delta = \tan \theta_1, \quad \omega_1 = \frac{\tan \theta_1}{\tan \theta_2}. \tag{5.10}$$

5.2.3 Synthesis of dual-band bandpass filters

Once the transfer functions of the structures analyzed have been derived in Section 5.2.1 and the low-pass to dual-band bandpass frequency transformations are known (5.9), (5.10), the proper filtering functions are derived herein. Thus, the design parameters Z_{0_a}, Z_{0_b} and c can be easily calculated equating the transfer function of the circuits (F_I, F_{II}) to the theoretical filtering functions (F_n) as

$$\epsilon F_n(\theta) = F_{I,II}(\theta), \tag{5.11}$$

where ϵ is the in-band ripple factor related to a given return loss L_R in decibels as [136]

$$\epsilon = \frac{1}{\sqrt{10^{L_R/10} - 1}}. \tag{5.12}$$

Prototype I

This prototype (Fig. 5.1(a)) has a polynomial F_I of order four with one real transmission zero at $\theta = \pi/2$. Thus, its frequency response can be modeled by using the generalized fourth-order Chebyshev function [135] and the Richard's frequency transformation. The transmission zeros of the S_{21} are located in

$$\tan \theta = 0, \infty; \quad \tan \theta = \pm j, \tag{5.13}$$

which can be mapped to the normalized ω frequency as (5.10)

$$\omega_{z1} = 0, \quad \omega_{z2} = \infty, \quad \omega_{z3,z4} = \pm j\delta = \pm j \tan \theta_1. \tag{5.14}$$

To compute the filtering function in the ω-plane, once the transmission zeros and the specifications of the passbands (θ_1 and θ_2) are given, the recursive formulas derived in [135] are employed. Subsequently, a filtering function for a fourth-order dual-band BPF can be obtained. However, it can be demonstrated that, regardless of the values of Z_{0_a}, Z_{0_b}, and c, it is not possible to obtain four real transmission poles. The roots of the numerator of F_I can be calculated by solving the quadratic equation

$$g_4 x^2 + g_2 x + g_0 = 0, \tag{5.15}$$

with x=$\tan^2 \theta$. However, because g_0/g_4 is always negative, one root of (5.15) will be positive whilst the other negative and, consequently, this structure is unsuitable for generating four real poles. Nevertheless, under the condition $\bar{Z}_{0_a} c$=1, this topology can be used to design second-order dual-band BPFs. Imposing this relationship on (5.5), the new transfer function reduces to

$$F_I = \frac{g_2 \tan^2 \theta + g_0}{\tan \theta}, \quad K_I = \frac{1}{2c^2 \bar{Z}_{0_b}}$$

$$g_2 = K_I, \quad g_0 = -2\bar{Z}_{0_b} \left(1 - c^2\right) K_I. \tag{5.16}$$

Note that this transfer function has only a transmission zero at θ=$\pi/2$ and, thus, the dual-band filtering function F_n can be obtained using the two frequency transformations discussed in Section 5.2.2. It can be proved that both methods lead to the same result. From a first-order Chebyshev polynomial in the ω-plane (F_n=ω), and after the frequency mapping (5.9) to the bandpass domain, the filtering function is given by

$$F_n(\theta) = \frac{g_{2t} \tan^2 \theta + g_{0t}}{\tan \theta}$$

$$g_{2t} = a, \quad g_{0t} = -b. \tag{5.17}$$

Equating (5.17) to (5.16), the following relations between coefficients are obtained

$$\frac{g_0}{g_2} = \frac{g_{0t}}{g_{4t}}, \quad \epsilon = \frac{g_2}{g_{4t}}, \tag{5.18}$$

that can be used to calculate the closed-form design equations as

$$\bar{Z}_{0_b} = \frac{1 + b\epsilon}{2a\epsilon} \tag{5.19a}$$

$$c = \frac{1}{\sqrt{1 + b\epsilon}} \tag{5.19b}$$

$$\bar{Z}_{0_a} = 1/c. \tag{5.19c}$$

For this configuration, there is a single transmission pole in each passband, so that ϵ determines the return losses (L_R) at the cut-off frequencies (θ_1 and θ_2). Mathematical development of filtering functions for prototype I is described in Appendix B.

Prototype II

This prototype (Fig. 5.1(b)) has two real transmission zeros at $\theta = \pi/2$ (5.6b) and it can be designed to generate four real poles. Therefore, the use of a conventional second-order Chebyshev polynomial with the frequency transformation indicated in (5.9) is used to obtain the required theoretical filtering function. If the generalized Chebyshev low-pass prototype presented in [135] was used, it would be possible to generate only an odd number of transmission zeros at the middle frequency of the two passbands. However, with the second-order polynomial and the low-pass to dual band-pass transformation (5.9), a filtering function with two real transmission zeros can be generated. The second-order Chebyshev polynomial $F_n = 2\omega^2 - 1$ is mapped to the θ-plane as

$$F_n(\theta) = \frac{p_{4t} \tan^4 \theta + p_{2t} \tan^2 \theta + p_{0t}}{\tan^2 \theta} \tag{5.20}$$
$$p_{4t} = 2a^2, \quad p_{2t} = -(4ab + 1), \quad p_{0t} = 2b^2,$$

and by equating this function with (5.6b), the following relationships are derived

$$\frac{p_2}{p_4} = \frac{g_{2t}}{g_{4t}}, \quad \frac{p_0}{p_4} = \frac{g_{0t}}{g_{4t}}, \quad \epsilon = \frac{p_4}{p_{4t}}. \tag{5.21}$$

Note that the term $1/\sin\theta$ in (5.6b) is not in the filtering function obtained in (5.20). Therefore, the next design equations will provide an approximated synthesis procedure. Nevertheless, once the design parameters are obtained, they can be easily corrected by

means of (5.6). From (5.21), the circuit design parameters can be calculated as

$$\bar{Z}_{0_a} = \left(1 + \frac{4ab\sqrt{1-c^2} - (4ab+1)(1-c^2)}{2b^2c^2}\right)^{\frac{1}{2}} \qquad (5.22a)$$

$$\bar{Z}_{0_b} = \bar{Z}_{0_a}\frac{c}{\sqrt{1-c^2}}\frac{b}{a} \qquad (5.22b)$$

$$\epsilon = \frac{1-c^2}{c^2}\frac{1}{4\bar{Z}_{0_a}b^2}, \qquad (5.22c)$$

where $\bar{Z}_{0_a}$ and $\bar{Z}_{0_b}$ depend on both, the coupling factor and the specifications of the pass bands (θ_1 and θ_2). Besides, from (5.22a) and (5.22c) it is possible to find an expression that relates c with the in-band ripple factor ϵ (5.12) as

$$
\begin{aligned}
a_4 x^4 &+ a_3 x^3 + a_2 x^2 + a_1 x + a_0 = 0 \\
a_4 &= 1 - 8\epsilon^2 m^2 b^2 (1 + 4ab + 2b^2) \\
a_3 &= 32\epsilon^2 m^2 ab^3 \\
a_2 &= 8\epsilon^2 m^2 b^2 (1 + 4ab + 4b^2) \\
a_1 &= -32\epsilon^2 m^2 ab^3 \\
a_0 &= -16\epsilon^2 m^2 b^4 \\
m &= 1/\sin\theta_{01}
\end{aligned}
\qquad (5.23)
$$

where

$$c = \sqrt{1-x^2}. \qquad (5.24)$$

In (5.23) the term $\sin\theta_{01}$ has been included to compensate for the effect of $1/\sin\theta$. Utilizing this correction, it is guaranteed that the desired return losses are achieved at the central frequency of both passbands. The analytical solution of this quartic equation (5.23), using an efficient algorithm proposed in [137], is described in Appendix C.

Consequently, once the specifications of the dual-band BPF are known, equations (5.22a) and (5.22b) can be used along with (5.23) to determine analytically the design parameters of the filter.

5.3 Bandwidth and design considerations

In the previous section, design equations for the two prototypes shown in Fig. 5.2 are obtained. However, it would be desirable to get a relation between the circuit design parameters and both, the achievable operating bandwidth and the pass band frequency ratio. Obviously, the performance of both filters will be conditioned by the required design values for the MTL and the shunt stub, and the limit values imposed by the manufacturing process capability. Therefore, it is possible to establish some design criteria depending on the obtained values.

Figure 5.4 shows several values of Z_{0_a}, c and Z_{0_b} in order to achieve different combinations of FBW and frequency ratio ($r = f_{02}/f_{01}$) for prototypes I and II, respectively. L_R=3 dB (ϵ=1) is used for prototype I, while for prototype II $L_R = 15$ dB has been employed. Thus, the 3 dB-FBW is considered for the former, while the FBW with equal-ripple response is defined for the latter. This definition is shown in Fig. 5.5.

As seen in Fig. 5.4, prototype I allows narrower bandwidths, independently of the separation between bands. Nevertheless, to achieve high-frequency ratios, low stub impedances (Z_{0_b}) must be used. Furthermore, increasing the number of conductors (k) must be taken into account to get a low MTL characteristic impedance (Z_{0_a}) and high coupling factors (c) [12]. Prototype II does not allow narrow bandwidths because large stub widths would be needed. In addition, it is remarkable that the frequency ratio hardly varies with the MTL impedance. As this impedance must be low, the number of conductors has to be increased to achieve the desired MTL impedances [12], justifying again the use of MTLs instead of only a pair of coupled lines. Thus, prototype I is more appropriate when using higher frequency ratios and narrow bandwidths, whereas prototype II is better suited to wide bandwidths. Once these criteria are taken into account, the design parameters can be effortlessly selected to synthesize the desired frequency response of the filter.

Taking into account the design considerations and limitations previously mentioned, it is possible to elaborate a design procedure to select the best prototype depending on the required specifications. This procedure can be summarized as follows:

- *Step 1:* From (5.8), calculate θ_{01} and θ_{02} according to the desired central frequencies of both bands (f_{01}, f_{02}) and the FBW. Obtain the value of f_0.

- *Step 2:* Choose the MTLs and stubs lengths to be a quarter-wavelength long at f_0.

(a)

(d)

(b)

(e)

(c)

(f)
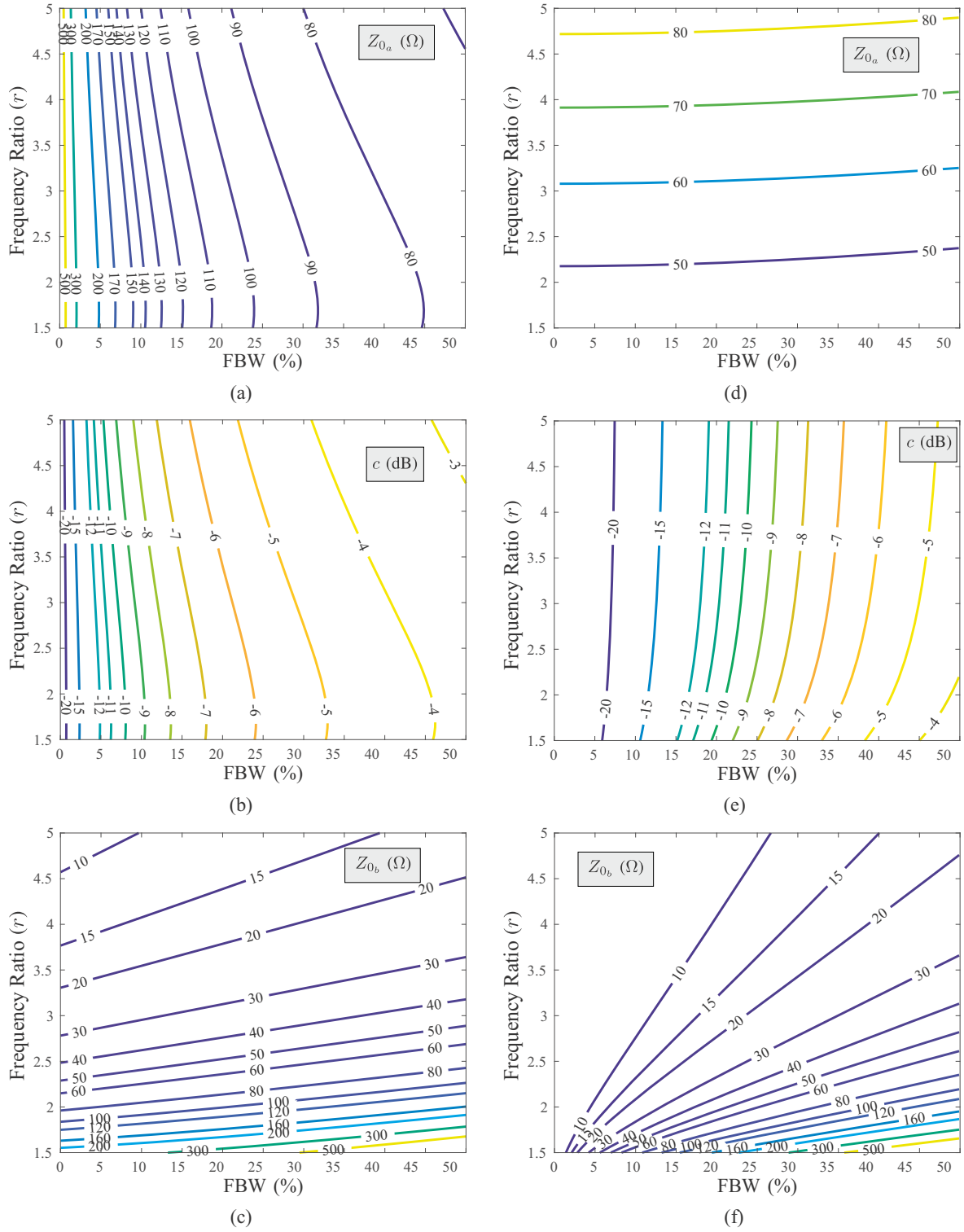
Figure 5.4: Z_{0_a}, c and Z_{0_b} values for prototype I (a)(b)(c) and prototype II (d)(e)(f), depending on the fractional bandwidth and the frequency ratio (r), calculated using (5.19), (5.22) and (5.24).

- *Step 3:* Obtain the values of a and b using (5.9).
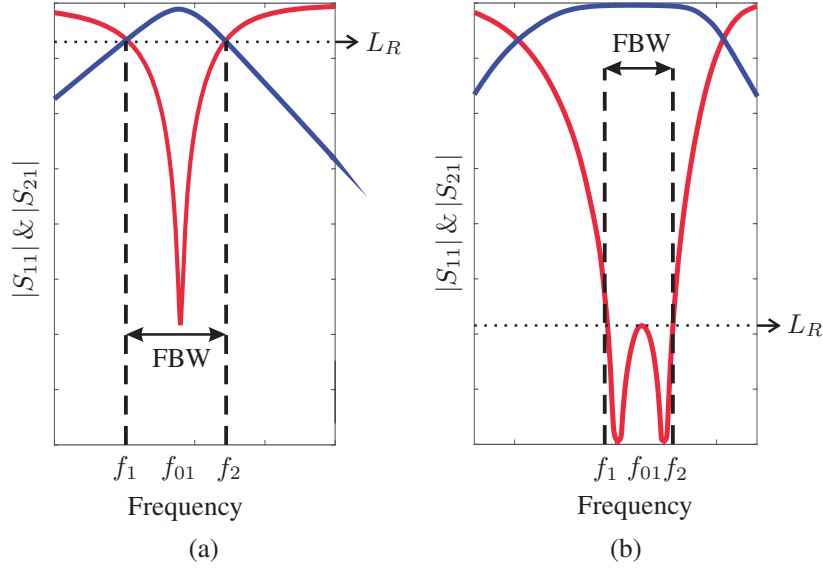
Figure 5.5: Fractional bandwidth definition: (a) prototype I and (b) prototype II.

- *Step 4:* Look at Fig. 5.4 and decide which prototype is more suitable for the given specifications, taking into account the FBW definition. When choosing the first prototype, consider L_R=3 dB (ϵ=1), but for the second one, obtain the in-band ripple factor ϵ, depending on the desired return losses L_R (5.12).

- *Step 5:* Use (5.19) or (5.22) and (5.24), depending on the chosen prototype, to calculate the required values of Z_{0_a}, c and Z_{0_b}.

Finally, it should be verified that the accomplished values are physically achievable by the manufacturing process. The whole design process is depicted in the flowchart of Fig. 5.6.

5.4 Multi-band bandpass filters

From the circuit elements used in this chapter, it is also possible to obtain multi-band responses. For this purpose, the topology shown in Fig. 5.7 is proposed. It is composed of two identical short-circuited MTLs, several shunt open stubs (by simplicity, only two are depicted in Fig. 5.7), and spur-line sections at the input and output of the filter to mitigate the first replica of the structure. The analysis is based on the one in Section 5.2.1. In short, the S-parameters from the TL equivalent model are computed and considered to obtain a proper filtering function so, finally, determine circuit design parameters.
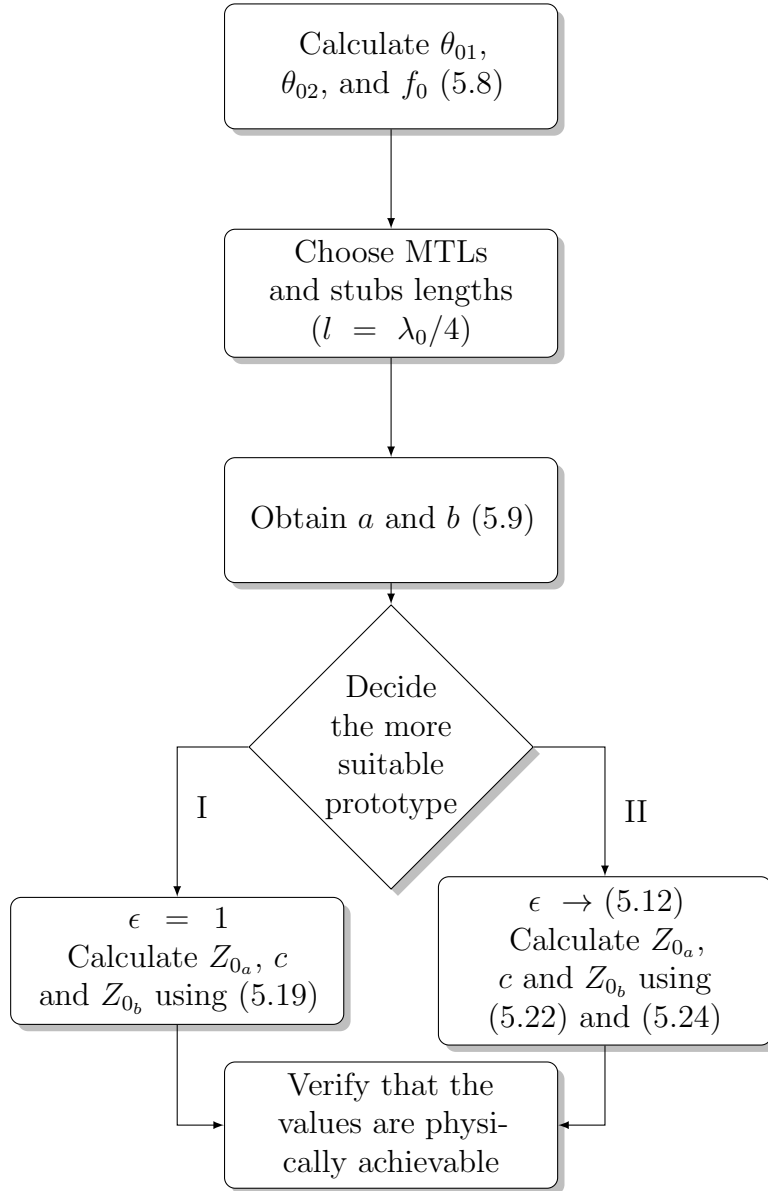
Figure 5.6: Flowchart of the filter design process.

The open stubs are defined by their characteristic impedance (Z_{b_i}) and electrical length (θ_{b_i}), whereas the equivalent model of the spur-line filters is composed by a TL section and a shunt open stub. Their characteristic impedances, Z_{sl1_j} and Z_{sl2_j}, can be calculated from [138]

$$Z_{sl1_j} = \frac{Z_{oo_{sl_j}} + Z_{oe_{sl_j}}}{2} \tag{5.25a}$$

$$Z_{sl2_j} = \frac{Z_{oe_{sl_j}}}{Z_{oo_{sl_j}}} \left(\frac{Z_{oe_{sl_j}} + Z_{oo_{sl_j}}}{2} \right), \tag{5.25b}$$

where $Z_{oe_{sl_j}}$ and $Z_{oo_{sl_j}}$ are the even- and odd-mode impedances of the pair of coupled
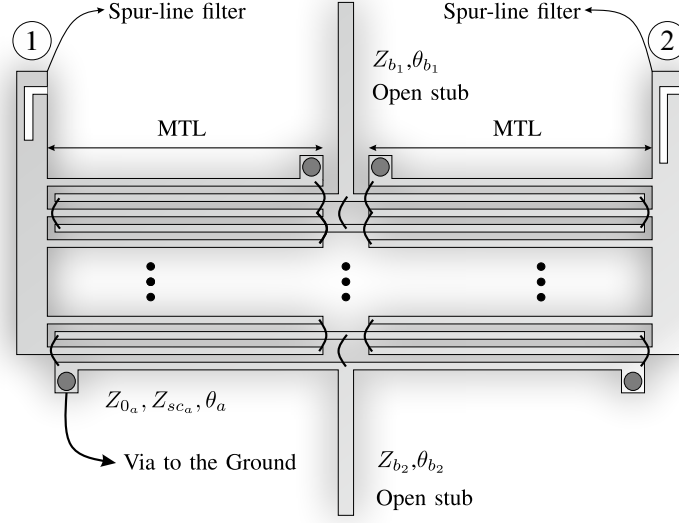
Figure 5.7: Layout of the proposed circuit for the analyzed multi-band bandpass filter.

lines that forms the filter, and the electrical length, θ_{sl}, is calculated again as the arithmetic mean value of the even- and odd-mode electrical lengths. The complete circuit model is presented in Fig. 5.8. The total S-parameter matrix can be obtained by cascading the transmission parameters of every section in the equivalent model.

5.4.1   Design considerations

The operation of the filter is based on splitting the wide band of the MTLs by forcing transmission zeros inside it with the stubs. These real transmission zeros will be used to get a good rejection for out-of-band signals and to improve the isolation between adjacent bands.

Multiconductor transmission lines

MTL design is the first step that must be taken. One of the most important advantages of using MTLs instead of a pair of coupled lines is the feasibility for synthesizing a wide range of different impedance values compared to a pair of coupled lines. This fact can be used to achieve high selective filters. The achievable values of Z_{0_a} and Z_{sc_a} as a function of line width W and spacing S for a different number of conductors are represented in [12] (Fig. 3). That plot was calculated using the Rogers 4350B substrate,
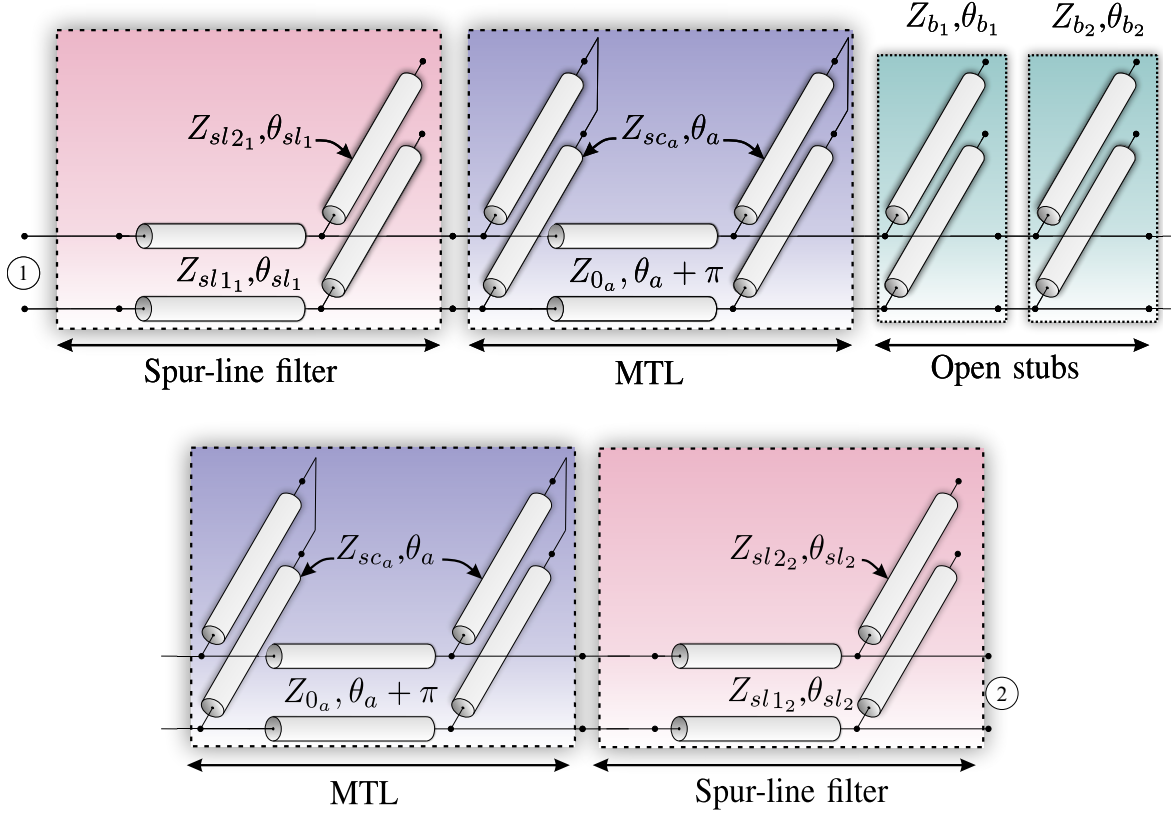
Figure 5.8: Equivalent circuit model for the proposed filter.

with a dielectric constant of 3.66, a loss tangent of 0.0031, and a thickness of 30 mils. This is also the substrate used in this chapter's analyzed and manufactured prototypes. As it can be seen, increasing the number of conductors or reducing the space between them, it is possible to achieve lower values of Z_{0_a}, and, therefore, it increases the design possibilities concerning using the traditional pair of coupled lines. Transmission zeros inherent to the MTL are located at $\theta_a = n\pi$, $n = 0, 1, 2, 3, ...$ However, the exact position of the zeros will vary with the MTL parameters. For instance, bandwidth will be wider and more selective when decreasing both finger width and gap spacing between them, equivalent to increasing the coupling factor. Another aspect that must be taken into consideration is MTL fingers interconnection. When connecting them, their real length is greater than the one without considering the interconnection. This fact provokes a resonance close to the transmission zero, when the length is equal to $\lambda/2$. Nevertheless, this fact can be effortlessly corrected by adding wire-bondings connecting alternate lines in the middle of the MTLs. Doing it guarantees that the alternate lines maintain the same voltage in the middle of the MTL. Therefore, the propagation of undesired TEM modes is avoided, so resonances are eliminated. Higher frequency resonances and replicas will be mitigated by the spur-line sections at input

and output ports.

Open stubs

The role of the open stubs included in the design is to force real transmission zeros in the middle of the MTLs passband. For this reason, the stubs will work as quarter-wave transformers, imposing short-circuit conditions to the structure at the desired frequency. When doing it, transmission zeros inherent to the stubs are located at $\theta_{b_i} = n\frac{\pi}{2}$, $n = 1, 3, 5, \dots$. Theoretically, N transmission zeros can be forced by N open stubs inside the MTL band, and consequently, there will be N+1 bands. In real cases, transmission media and geometry limit the number of possible stubs. Tee junction and open-ended effect in the shunt stubs [139] must be considered carefully to improve the design precision. To increase the order of the filter, it would be enough to choose stubs with greater bandwidth, such as radial stubs.

Spur-line sections

Spur-lines have been traditionally used as microstrip bandstop filters. They are compact structures, not susceptible to influence other parts, and they can be placed in every part of the circuit. They are used to mitigate the undesired high-frequency replicas of the MTLs and the stubs, and they will be located at the input and the output of the filter.

Design criteria

To design the proposed filter, the first step is to choose the MTL bandwidth through its length and position the zeros with the stubs, where its electrical length is equal to $\lambda/4$. To achieve a more selective filter and increase the bandwidth, it is only necessary to increase the coupling of the MTL or decrease the impedance of the stub, being possible to obtain very selective responses without the need to optimize or perform EM simulations, just using the analytical model.

5.5   Experimental validation

5.5.1   Dual-band filters

Three filters have been designed, fabricated, and measured to assess the developed theory and techniques. For prototype I, the center frequency was $f_0 = 3.9$ GHz, using the analytical equation (5.19) to choose its parameters. For the two filters of prototype II, the center frequency was set to be $f_0 = 2$ GHz, using (5.22a), (5.22b) and (5.23). The physical dimensions and design parameters are given in Table 5.1. All the measurements have been obtained by using Agilent PNA-X N5247A, after a TRL calibration to position reference planes correctly for further comparisons. Figure 5.9 details the coaxial to microstrip transition used for the characterization of filters designed in this chapter. Figures 5.10, 5.11 and 5.12 show the predicted values by analytical equations (5.5) and (5.6), and measured S-parameter results of the fabricated prototypes. In this sense, the measured group delay responses and photographs of these filters are depicted as well in Figs. 5.10, 5.11 and 5.12. For prototype II, double shunt open stubs have been used to reduce the stub width. The minimum strip width and the gap between lines allowed by our manufacturing capability are limited to 100 μm, which determines the range of possible values of Z_{0_a}, Z_{0_b} and c, and therefore, conditions the achievable frequency responses of the filters.
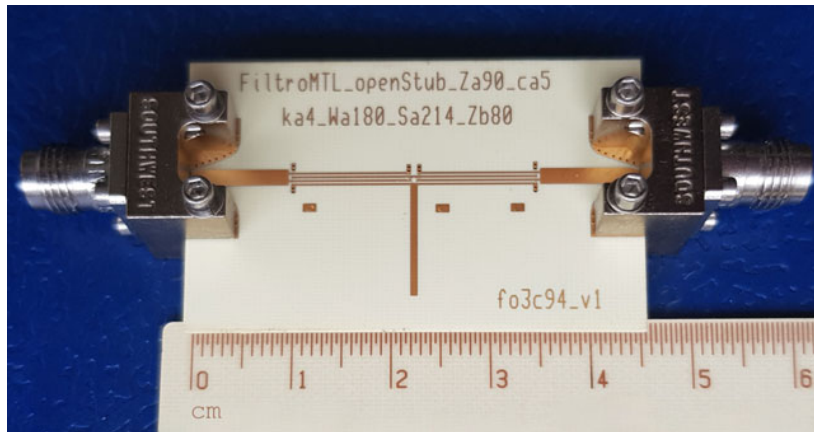
Figure 5.9: Photograph of the first prototype filter with connectors and a ruler that show its dimensions.

From Figs. 5.10, 5.11 and 5.12, it is noted that there is a very good agreement between the predicted and measured S-parameter results. In Fig. 5.11, it is plotted the broad-band measurement of one of the filters. As they are distributed structures, there will be replicas because of the wavelength dependence. The selectivity at the high
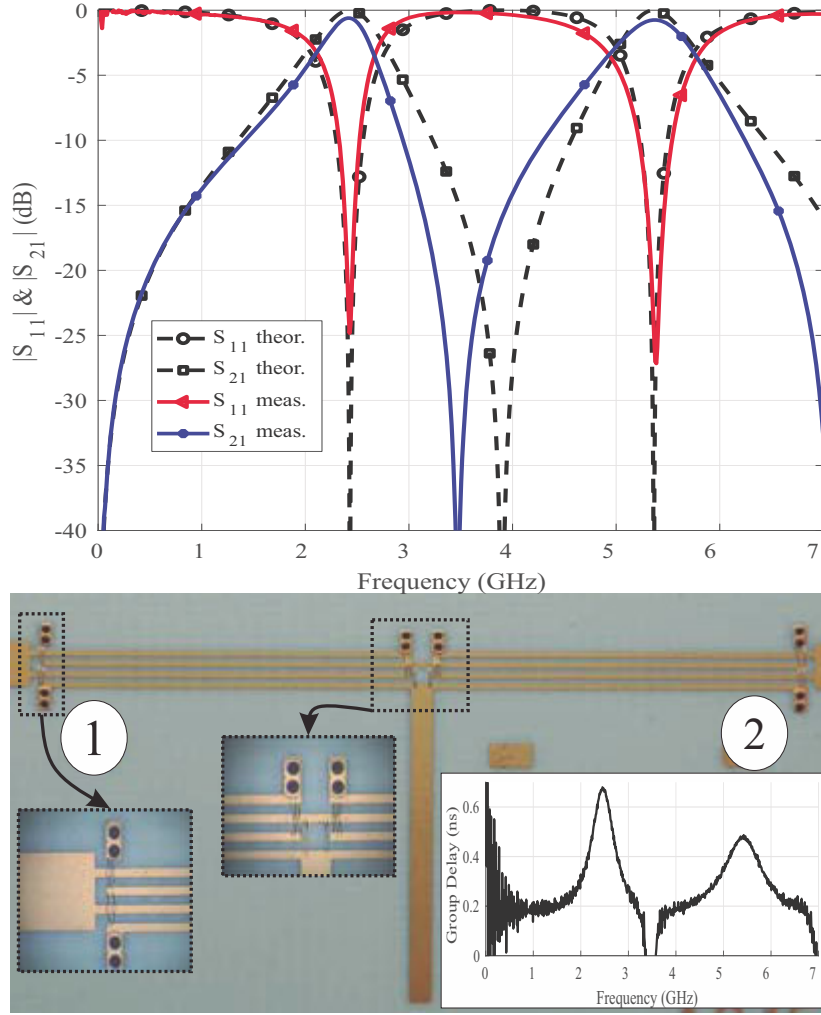
Figure 5.10: Theoretical prediction (5.5) and measured S_{11}, S_{21} and group-delay parameter performances for the manufactured prototype I filter (see Table 5.1).

side of the first passband and the low side of the second passband is better because they are close to the transmission zero, whereas in the opposite sides of the passband, transmission zeros are far away, and the slope is slight. FBW of 30% is used in the filter of the first prototype, whereas 30% and 48% are the ones for the second type. Deviations in the central frequency f_0 or S_{11} parameters and high-frequency degradation are mainly due to fabrication tolerances, unequal even- and odd-mode phase velocities in the wire-bonded MTLs as well as tee junction and open-ended effect in the shunt stubs [139].

Finally, a comparison of the proposed prototypes is summarized in Table 5.2. In this table, 3-dB FBW is used in all the cases, and λ_g denotes the guided wavelength at the center frequency of the lower passband. The proposed filters are more compact, even taking into account that stubs are not bent, which would have reduced even
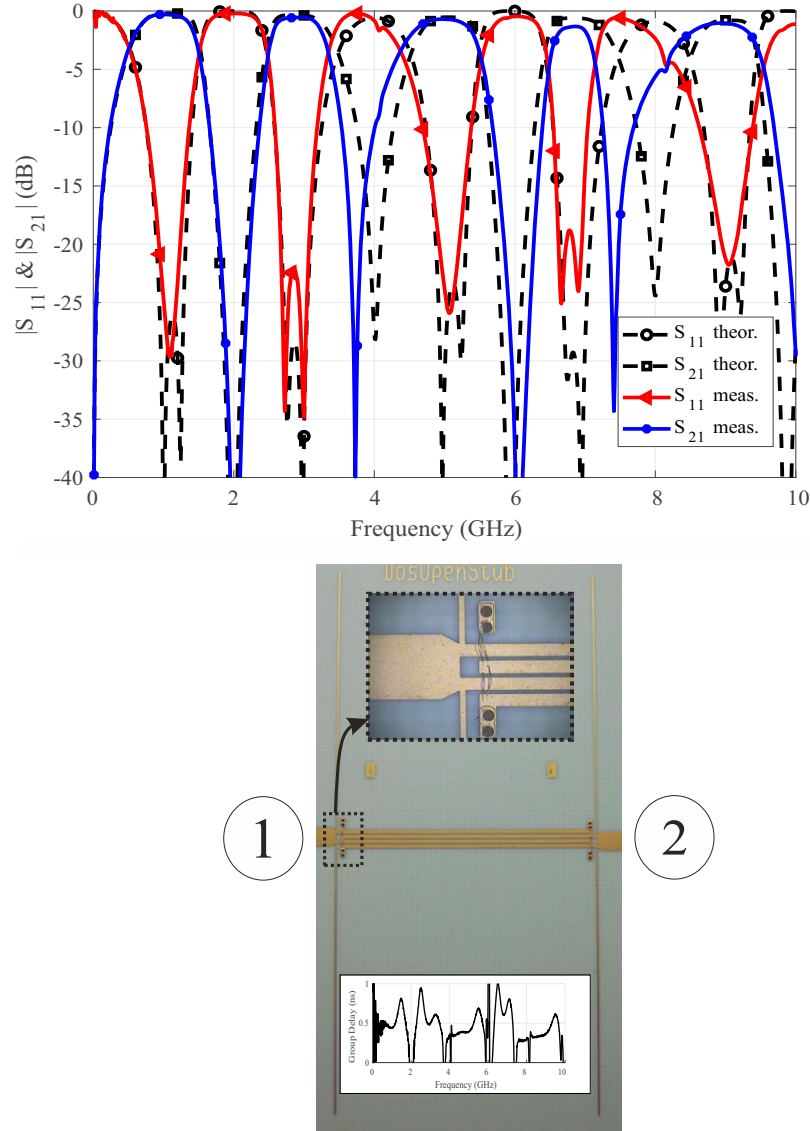
Figure 5.11: Theoretical prediction (5.6) and measured S_{11}, S_{21} and group-delay parameter performances for the manufactured prototype II first filter (see Table 5.1).

more the size of the circuits in the transversal dimension. In terms of insertion and return losses, the obtained results are significant in both bands, outperforming most of the compared cases. It must be taken into account that all the filters have been designed directly using the computed analytical equations previously developed, without any optimization made by an EM simulator. Furthermore, it is important to remark that there was no post-manufacture tuning. These facts are significant not only for validating the presented theory but also for providing feasibility to design dual-band BPFs without using an EM simulator, just by taking the analytical equations developed and calculating the MTL and stub parameters [91, 142].
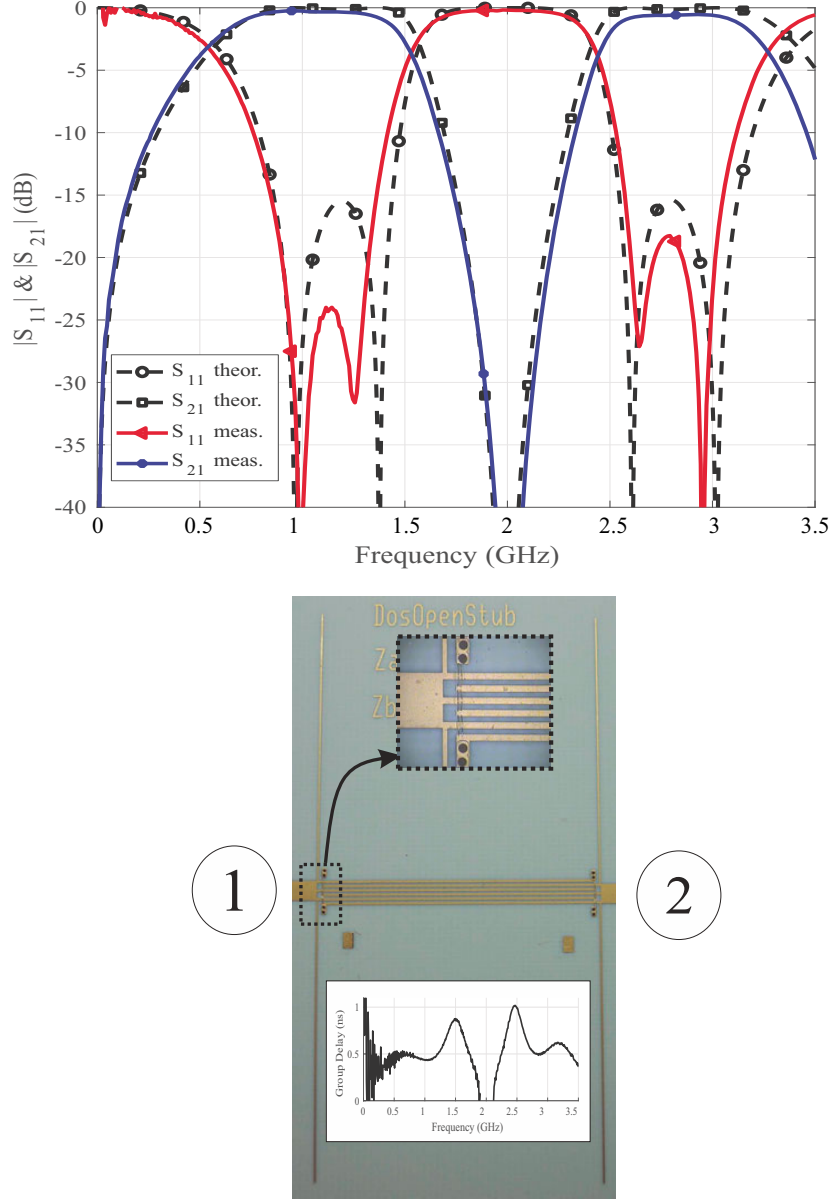
Figure 5.12: Theoretical prediction (5.6) and measured S_{11}, S_{21} and group-delay parameter performances for the manufactured prototype II first filter (see Table 5.1).

5.5.2 Multi-band filters

As a design example of the multi-band BPFs, a prototype fabricated using Rogers 4350B substrate ($h = 30$ mils) has been manufactured using external commercial facilities. The physical dimensions of the filter are summarized in Table 5.3. It is noteworthy that a problem in manufacturing tolerances caused a variation in the impedances of the original circuit design. Two identical short-circuited MTLs and two open stubs of different lengths and same widths are interconnected, as depicted in Fig. 5.13. When considering the dispersion model for microstrip and coupled lines, the values of the

Table 5.1: Physical dimensions of the fabricated filters.

	f_0 (GHz)	FBW* (%)	f_{02}/f_{01}	Z_{0_a} (Ω)	Z_{0_b} (Ω)	c (dB)	Z_{sc_a} (Ω)	Z_{oe_a} (Ω)	Z_{oo_a} (Ω)	k_a	W_a (μm)	S_a (μm)	l_a (mm)	W_b (μm)	l_b (mm)
Fig. 5.10	3.5	30	2.2	90	80	-5	115	184	78	4	180	214	12	685	12
Fig. 5.11	2	30	2.55	60	70	-4	102.5	157	57	4	314	118	23.5	130	23.8
Fig. 5.12	2	48	2.45	50	70	-4	85	185	75	6	195	200	23.7	130	24

FBW*: 3 dB-FBW (Prototype I) or FBW with equal-ripple response (Prototype II)

Table 5.2: Comparison among the proposed dual-band filters and published ones.

Filter	Frequency ratio (f_{02}/f_{01})	3-dB FBW (%)	Return Losses (dB)	Insertion Losses (dB)	Transmission Zeros in $(0, 2f_0)$	Size ($\lambda_g \times \lambda_g$)
[107]	1.08	4 / 3.7	21.52 /23.78	0.98 / 1.03	2	$0.33\lambda_g \times 0.34\lambda_g$
[109]	1.41	13 / 9.3	12	1.2	4	$0.3\lambda_g \times 0.28\lambda_g$
[140]	2.24	6.5 / 19.1	15 / 12	1.86 / 1.4	3	$0.327\lambda_g \times 0.194\lambda_g$
[141] A	1.77	3.3 / 2.4	14	1.3 / 1.8	3	$0.29\lambda_g \times 0.58\lambda_g$
[141] B	1.97	8.2 / 6.7	14	1.3 / 1.2	4	$0.29\lambda_g \times 0.29\lambda_g$
Fig. 5.10	2.2	30	24.9 / 27.2	0.6 / 0.74	3	$0.36\lambda_g \times 0.18\lambda_g$
Fig. 5.11	2.55	48	29.7 / 22	0.28 / 0.54	3	$0.165\lambda_g \times 0.33\lambda_g$
Fig. 5.12	2.45	50	24 / 18.5	0.25 / 0.52	3	$0.17\lambda_g \times 0.34\lambda_g$
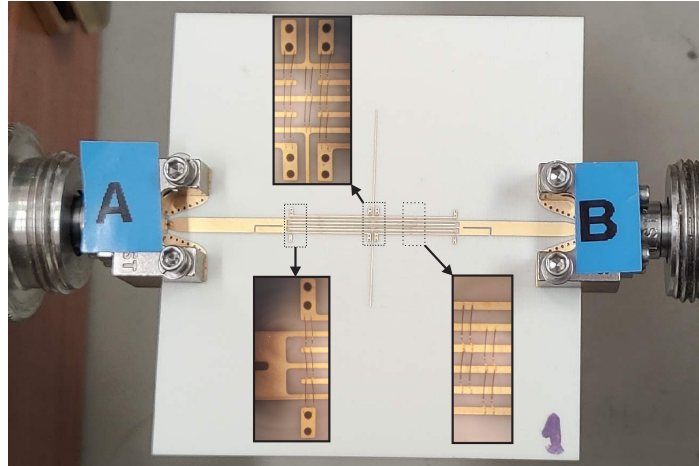
Figure 5.13: Photograph of the manufactured prototype with 6-finger short-circuited Multiconductor Transmission Lines and two shunt open stubs.

characteristic impedances are $Z_{0_a} = 56.5$ Ω (69.3 Ω in the manufactured prototype), $Z_{sc_a} = 91.9$ Ω (99.1 Ω) and $Z_{0_b} = 140.6$ Ω (158.6 Ω) respectively, using a reference impedance $Z_0 = 50$ Ω. The first transmission zero of the MTL must be located at 9.55 GHz, whereas the zeros provoked by the open stubs should be located at 3.91 GHz and 5.87 GHz, respectively. It could be used for WiFi, and other applications, such as IoT or vehicle-to-vehicle communications where high slopes are not critical and simple structures are needed. Theoretical S-parameters of the MTLs are calculated by using the model proposed in [131], whereas the model presented in [91] was used for the open stub. Once these parameters have been calculated, ABCD two-port parameters of both MTL and stub are computed. No EM simulation or optimization have been carried out for this design. Results are shown in Fig. 5.14. As seen, there is an excellent

Table 5.3: Physical dimensions of the simulated filters.

Parameter	Design Value	Manufactured
MTL number of fingers	6	6
MTL finger width	170 μm	123 μm
MTL finger separation	200 μm	238 μm
MTL finger length	9.5 mm	9.46 mm
Stub #1 width	130 μm	83 μm
Stub #1 length	8 mm	7.97 mm
Stub #2 width	130 μm	83 μm
Stub #2 length	12 mm	11.96 mm
Spur-line width	150 μm	192 μm
Spur-line gap	150 μm	195 μm
Spur-line length	3.25 mm	3.21 mm
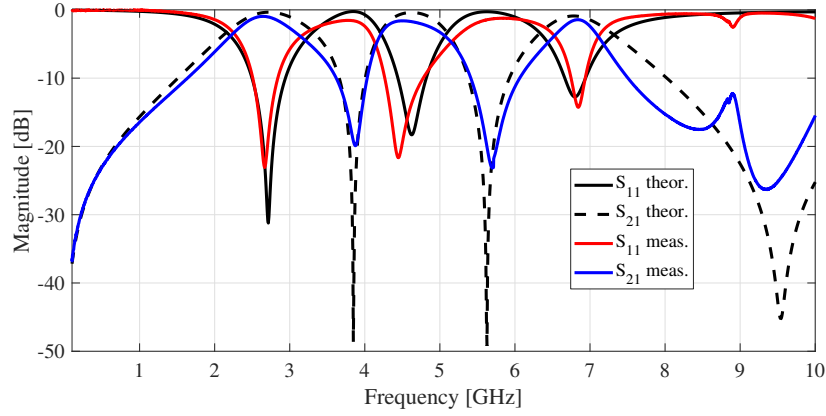
Figure 5.14: Analytical and measured scattering matrix elements (S_{11} and S_{21}) of the proposed prototype.

agreement between analytical and measured results. The small difference in bandwidth and matching is due to fabrication tolerances, which denotes the robustness of the technology presented, even when manufacturing errors are made. Finally, a comparison with others based on coupled lines filters found in the state-of-the-art is summarized in Table 5.4. In this table, RL denotes the minimum return losses, IL the maximum insertion losses, and λ_g is the guided wavelength at the center frequency of the lower passband. As it can be seen, the proposed filter improves the performance of those published, being more compact and easy to design.

Table 5.4: Comparison among the proposed multi-band filters and published ones.

Filter	RL (dB)	IL (dB)	Size ($\lambda_g \times \lambda_g$)
[119]	16.7	4.6	0.66 x 0.42
[143]	17.12	2.88	0.35 x 0.25
Proposed Filter	14.5	1.45	0.29 x 0.29

5.6   Conclusion

In this chapter, a rigorous analytical study consisting of short-circuited wire-bonded MTLs and shunt open stubs has been performed to design dual-band BPFs. First, closed-form equations are presented to characterize the behavior of the two developed configurations. From these analytical equations, a synthesis procedure is carried out to obtain the parameters that enable to have the desired Chebyshev frequency response. Expressions for two configurations, single-stub with two MTL sections and double-stub with a MTL section filters, have been deduced and validated through experimental results. In addition, the formulas presented here are also suited for designing other double-band bandpass coupled-line-based filters. It is important to stand out the excellent agreement between measured results and theoretical predictions, which gives designers a useful mathematical tool based on the developed theory for a quick and accurate synthesis of dual-band BPFs.

As an extension of the dual-band filters study, a modification of the proposed topology, consisting of two identical short-circuited MTLs interconnected with several shunt open stubs, has been proposed to obtain simple but extremely useful multi-band responses. When using this topology, a multi-band bandpass response is obtained as the open stubs create real transmission zeros in the MTL passband. By changing MTL and stubs parameters, it is possible to effortlessly select the central frequencies and the bandwidths of each band. Results from the considered prototype also showed an excellent agreement between the theoretical model and measurements, even considering manufacturing errors. Spur-line sections have been added to the circuit to mitigate the effect of the frequency response replicas inherent to distributed structures. In addition, it is noteworthy that there were no optimization processes or EM simulations throughout the design procedures provided in this chapter.

Chapter 6

Conclusions and Outlook

This final chapter summarizes the research work developed in this thesis and highlights the main contributions. Lastly, it points out different perspectives of future work to carry on from this research.

6.1 Summary and conclusions

The synthesis and main contributions of this thesis are listed below.

Characterization of transmission lines

Three different methods used for the experimental characterization of the propagation constant of TLs from two-port measurements have been compared. Although it might be thought that these three methods work similarly, it has been demonstrated that they have totally different behavior in the presence of errors. In this context, the main contributions are:

- Regarding random VNA errors, methods work in a completely different way. The best strategy is to use the method based on eigenvalues, which is the only one that does not show a resonant behavior.

- Regarding line lengths and conductivity errors, they work as a bias in the solution, being more significant at high frequencies.

- Regarding end-launcher repeatability errors, all methods work in the same way. Using the same connector kit instead of different ones in all the TLs used for the

characterization of the propagation constant is an appropriate way to reduce the uncertainty of the final estimation considerably.

- Increasing the number of lines and using a LMS estimator is an excellent way to reduce uncertainty in the solution.

Characterization of additive manufacturing materials

A simple technique to determine the broadband EM characteristics of additive manufacturing materials has been proposed. It has been demonstrated that it is very useful since no calibration is needed. The achieved results show an excellent agreement between measurements and simulations, which is why the proposed procedure can be considered an excellent alternative to those found on the literature. The model includes substrate dispersion and metal surface roughness effects. The main contributions on this topic are:

- The methods allow very accurate results in terms of attenuation constant and effective dielectric permittivity using only a few lines.

- A non-linear criteria to choose the line lengths has been proposed to minimize errors provoked by resonances.

- A dispersion model has been proposed to characterize the relative permittivity of the available material samples in the whole bandwidth of the used VNA (0.01-67 GHz).

- HIPS has demonstrated excellent losses and can be established as a candidate for fabrication of EM structures due to its loss tangent close to 0.004.

Characterization of coupled microstrip lines

A method to obtain the propagation constant of the even and odd modes of symmetrical coupled microstrip TLs has been presented, using lines of different lengths. For this purpose, the measurement of the pure-mode S-parameters has been used to obtain the separated matrix of each mode. The proposed method has been validated through simulations and measurements since four different prototypes have been manufactured. The main contributions are:

- A method to accurately characterize and obtain both modes' propagation constant in symmetrical coupled microstrip lines separately has been proposed.

- A rigorous and comprehensive study of the modes excitation that shows that bend angles in the feeding lines are critical for the attenuation constant has been presented. The estimated attenuation constant is significantly better when using reduced bend angles.

- The measured results are very accurate throughout the whole bandwidth of the available VNA (0.01-67 GHz), especially in the phase constant. This fact represents a significant advance in the characterization bandwidth for this kind of structures.

Multi-band bandpass filters

The use of MTLs and shunt open stubs have been proposed to synthesize compact dual-band BPFs. A synthesis procedure is carried out from the derived analytical equations to obtain the parameters of a filter with the desired Chebyshev frequency response. The presented theory is validated by designing, manufacturing, and measuring three prototypes. The excellent agreement between the analytical model and measurements gives designers the confidence to use the proposed model. Furthermore, an additional configuration that includes several shunt open stubs allows obtaining multi-band bandpass responses. Replicas inherent to the proposed distributed structure can be mitigated using spur-line sections. The main contributions about this topic are:

- A novel structure to design compact dual-band and multi-band BPFs with good out-of-band rejection has been proposed and assessed through experimental validation.

- A set of closed-form design equations is obtained to design dual-band bandpass compact filters with a Chebyshev type response using two different prototypes.

- A filter design technique is proposed to obtain multi-band bandpass responses effortlessly. It is possible to select both the bandwidth and the center frequency of each band.

6.2 Future work

Some brief ideas and guidelines are presented below as future work that can carry on from this dissertation:

- **Using Deep Learning Techniques for characterization of TLs**
  Deep learning techniques have been on the rise in recent years in many fields of science, including telecommunications. They can be used to estimate the main parameters of a TL from the measurement of its S-parameters since a model has been previously trained with parameters of other TLs. The main objective would be the extraction of the characteristic impedance together with the propagation constant. With this procedure, it would not be necessary to use lines of different lengths. However, the accuracy would depend on how well the model has been trained.

- **Characterizing materials in free space**
  The use of samples of AM materials that are illuminated with a transmitting antenna to study their transmissivity and reflectivity must be further explored in the future. For this purpose, the variation of S_{11} and S_{21} parameters must be explored when the material is located in the direct path between the transmitting and receiving antennas. From this variation, it would be possible to extract material EM characteristics.

- **Characterizing asymmetric coupled lines**
  The technique proposed in Chapter 4 is used to characterize the propagation constants of symmetric coupled lines. However, an extension of the method should be carried out to explore C and π modes of asymmetric and inhomogeneous coupled microstrip structures. For this purpose, it would be necessary to ensure that the excitation of both modes is carried out correctly.

- **Characterizing multiconductor transmission lines**
  Another possible application to the technique proposed in Chapter 4 is to characterize the propagation modes in MTLs with interconnected alternate lines. Another study should be performed to ensure that the excitation of both modes is carried out correctly.

- **Using MTL stub loading for creating higher order BPFs**
  The use of MTL-based stubs allows the implementation of impedance levels that

are unapproachable with a single stub and that are of interest for the design of filtering structures. They can be used in the proposed multi-band BPFs to achieve more selective responses since the used single stubs limit the bandwidth of the transmission zeros forced inside the broadband of the MTLs. Using MTL-based stubs would allow improving the reject between adjacent bands significantly.

- **Implementation of MTLs using AM**

  In this thesis, a planar transmission line prototype made by AM has been proposed. This technology can be beneficial for the manufacture of MTLs. However, it will be necessary to improve the found problems, such as the inhomogeneity of the substrates and the conductivity of the printed inks. If these problems could be improved, the manufacture and implementation of competitive microwave circuits, such as the filter topologies based on MTLs developed in this thesis, will be possible using AM technologies.

Appendix A

Influence of Conductivity in the Estimation of the Propagation Constant

This appendix aims to study how conductivity influences methods for characterization of the propagation constant. For this purpose, it is intended to characterize a TL used to feed an UWB antenna, creating a system like the one shown in the diagram in Fig. A.1. In this diagram, $[R]$ includes transition effects. Figure A.2 shows the set of layers that will make up the stripline. HIPS will be used as the dielectric material. The metallization of the upper and lower ground planes will be done by spray deposition. The center strip will be made by printing silver nanoparticle ink on a kapton substrate. This process requires a curing process, usually made by heat or photonic curing. If it is not done correctly, the conductivity (σ) of the strip can change, which would provoke a change in the propagation constant of the structure. If this fact happened, the TEM mode initially expected might not propagate as expected, and the effective relative permittivity could not coincide with the permittivity of the dielectric.

In this Appendix, an experimental study of the effect of strip conductivity on the phase constants and attenuation of the TL is presented. Section A.1 shows the description of the structure. In Section A.2, it is studied how conductivity affects methods for characterizing the propagation constant. Finally, the experimental results obtained are given in Section A.4.. Conclusions are provided in Section A.4.
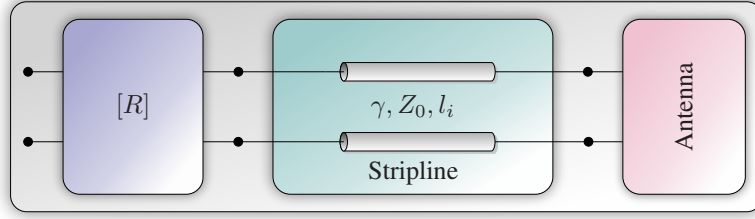
Figure A.1: Block diagram of the proposed device.
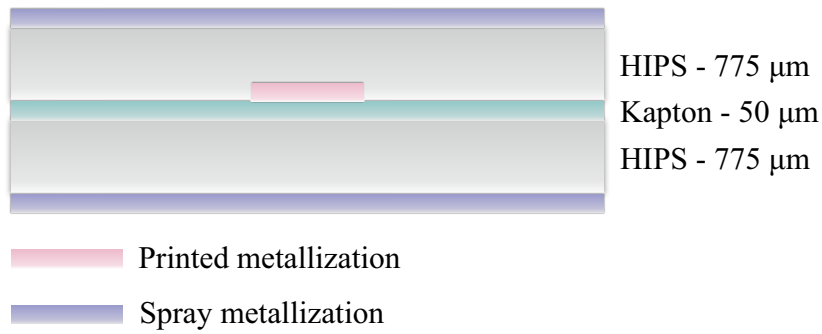
Figure A.2: Prototype stack-up.

A.1   Stripline description

An antenna using AM is being design using the stack-up of materials in Fig. A.2. That antenna, shown in the block diagram of Fig. A.1, requires a TL with a characteristic impedance, Z_0, of 50 Ω. A coaxial to stripline transition has been employed on each side of the stripline. This line is manufactured using two substrates made of HIPS and, subsequently, they have been metallized. These substrates have been manufactured by filament extrusion using the Ultimaker 3 printer with a height of 100 μm for each layer and a 100% density. Figure A.3 shows a photograph of the complete assembled structure, as well as the exploded view of the commercial connector. Between both substrates, a kapton film is inserted where the TLs have been printed using a silver nanoparticles ink [144] in the Fujifilm Dimatix DMP2850 material printer. In this structure, there is no impedance transformation since the width of the line remains constant at a value of 1.23 mm. The taper located on the ground plane is used only to screw the connector to the structure and causes little difference in the impedance of the line. In any case, this change in impedances would not affect the characterization method, as the used method is invariant to impedance transformations.
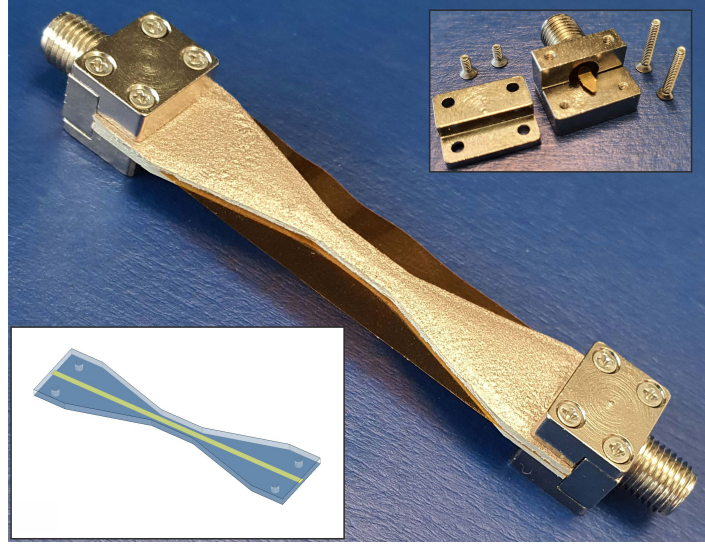
Figure A.3: Transmission line assembled with its connectors and an exploded view of those connectors.

A.2   Conductivity variation

One of the premises from which all invariant-based methods start is that the lines are made in the same way. This means that both the dielectric and the conductors are homogeneous, presenting the same permittivity, permeability, loss tangent, or conductivity properties. The problem is that these properties cannot be guaranteed in the proposed structure. Dielectrics can be assumed to be homogeneous and equal for all lines [22], as they are manufactured under the same conditions. However, it is more difficult to guarantee that the conductivity of metallic elements is the same. On the one hand, the ground planes are being metallized with a copper spray, whose conductivity depends on the homogeneity of the paint deposited on the substrate. On the other hand, the strip is made through ink printing. This printing requires a curing process whose main objective is that the element in which the silver nanoparticles are initially dissolved must be evaporated. The silver nanoparticles are deposited on the substrate and acquire conductivity through this process. The repeatability of this process is quite challenging to achieve. Proof of this is the difference in electrical impedance that the different conductors can present in every line. Starting from the previous problem, and to examine how the difference in the conductivities of the materials affects the proposed methods and the propagation constant, a simulation of the structure has been carried out in the full-wave simulator ANSYS HFSS [47], using metallic materials of different conductivity. For this purpose, the conductivity of the reference planes has been set and the one of the strip has been varied. Subsequently, it has been done
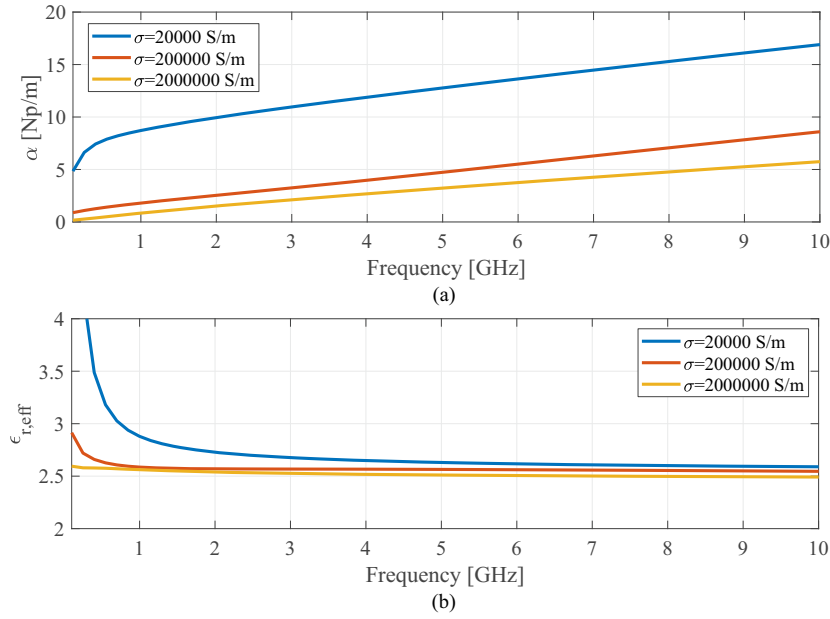
Figure A.4: Simulation of the attenuation constant (a) and effective relative permittivity (b) for several values of the conductivity of the strip.

oppositely, setting the one of the strip and changing the conductivity of the ground planes. Results show that the most influential factor is the conductivity of the strip, significantly affecting the propagation constant. That σ causes greater variations in the propagation constant than the one of the ground plane, both in the attenuation constant α and in the phase constant β. As seen in Fig. A.4, both constants increase their value when the conductivity is lower.

The sintering process is usually carried out by applying heat or light for a certain time, which the ink manufacturer usually specifies. Once this process has been performed, the ink is settled on the substrate and acquires the necessary conductivity. However, many times, factors can cause σ to vary from one strip to another: the number of printed ink layers made, the time between those passes, the handling of the strips, or whether the curing process is carried out correctly. All these factors make it impossible, in practice, to ensure that conductivity is the same in all the printed strips, so it can not be ensured that the propagation constants coincide at all. To study how this difference in the propagation constants affects the studied methods, it is proposed that one of the lines has a lower conductivity, so it will have a higher propagation constant, which will be called γ'. Taking this propagation constant, Eq. (2.2) can be rewritten as

$$[L] = \begin{bmatrix} e^{\gamma l_2 - \gamma' l_1} & 0 \\ 0 & e^{\gamma' l_1 - \gamma l_2} \end{bmatrix} = \begin{bmatrix} e^{\gamma \Delta l'} & 0 \\ 0 & e^{-\gamma \Delta l'} \end{bmatrix}, \tag{A.1}$$
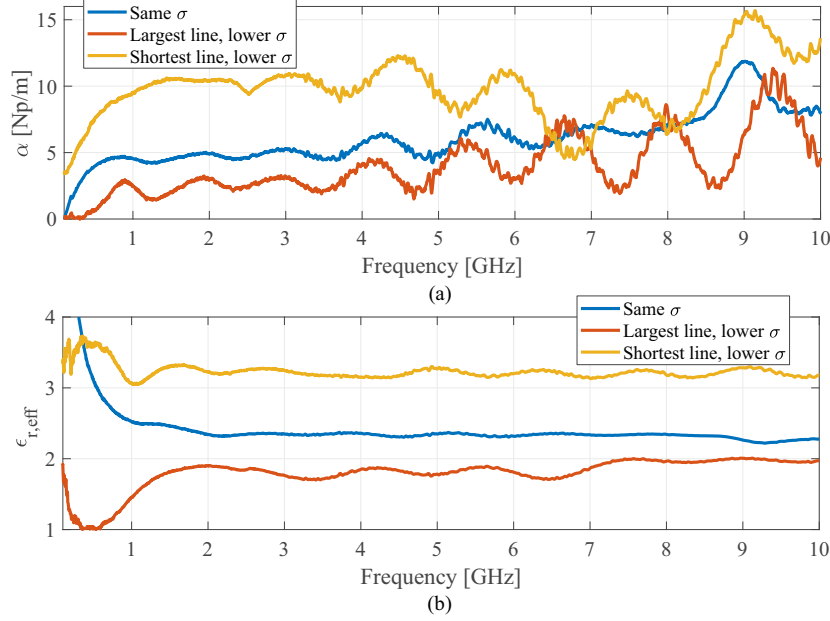
Figure A.5: Experimental results of the attenuation constant (a) and effective relative permittivity (b) estimated using lines of the same or different conductivity.

being $\Delta l_i' = l_2 - \xi l_1$ and $\xi = \gamma'/\gamma$. ξ is the quotient between the propagation constants. These constants are imaginary numbers whose phase is very close to $\pi/2$. This quotient, therefore, will tend to be a real number. Furthermore, it is known that γ' will be greater than γ, as it belongs to the line with the lowest conductivity. This fact guarantees that ξ will always be greater than 1. It implies that the proposed equivalent length variation, $\Delta l_i'$, is different from the original one but real. As demonstrated in [50], an error in the length of any of the lines corresponds to a deviation in the solution. This deviation will be positive if the line with the shortest length is the one with the lowest conductivity, while it will be negative otherwise.

A.3 Results

Four striplines, whose lengths are 10, 14.01, 19.22 and 25 mm, have been manufactured to check the validity of the proposed method. These dimensions have been calculated following the quasi-linear criterion with $q = 1.2$ raised in Section 2.4. However, and to check the validity of the proposed theory, one of the lines has had a reduced curing time, forcing its conductivity to lower values. Figure A.5 shows the obtained results applying the method to the four lines of equal conductivity, as well as applying it to a pair of lines with different conductivity. As expected, the different conductivities turn into a bias in the solution. It can be seen in both the attenuation constant and the phase constant.

When the line of lower conductivity is the longest one, the displacement is negative, while when it is the shortest, the bias is positive. In addition, it is possible to check how the precision of the method improves as the number of lines is increased. Although the structure presents high losses, its operation is correct in the band between 0.01 and 10 GHz. Above that frequency, high losses associated with low conductivity make it very difficult to use this technology for manufacturing electromagnetic structures. However, effective relative permittivity does show good behavior, tending to the nominal HIPS substrate, which is around 2.45 [50]. This is because being a closed stripline, the field is concentrated in the substrate, and the propagation is carried out through a TEM mode.

A.4   Conclusion

In this appendix, the use of a broadband method to characterize the propagation constant of a stripline made with additive manufacturing has been studied. As the lines were not complete equals, the method's results varied depending on the lines used. After some checks, it was possible to conclude that these differences were due to the conductivity of the printed conductor since it is highly variable depending on the curing process. This variation has been characterized as an error in the effective length of the lines, which is interpreted as a bias in the propagation constant. Therefore, it can be concluded that it is essential to properly carry out the curing process to guarantee that the propagation constant is the same in all lines. Thus, it is possible to apply appropriate characterization methods that allow extracting the propagation constant from measurements.

Appendix B

Filtering Functions for Chapter 5, Prototype I

Given the prescribed transmission zeros in the low-pass domain as

$$\omega_z = \{0, \infty, j, -j\} \tag{B.1}$$

the filtering function in the normalized frequency ω for a fourth-order Chebyshev filter is obtained as follows [135]

$$F_I(\omega) = \frac{t_4\omega^4 + t_2\omega^2 + t_0}{\omega\left(\delta^2 + \omega^2\right)}. \tag{B.2}$$

This function is mapped to the θ-plane as ($\omega = -\delta\cot\theta$)

$$F_n(\theta) = \frac{g_{4t}\tan^4\theta + g_{2t}\tan^2\theta + g_{t0}}{\tan\theta\left(1 + \tan^2\theta\right)}, \tag{B.3}$$

where coefficients t_i and g_{it} are given by

$$
\begin{aligned}
t_4 &= K\frac{\gamma(1+\omega_1) + 2}{(1-\omega_1)^2(1+\omega_1)} \\
t_2 &= K\frac{-\gamma(1+\omega_1)(1+\omega_1^2) - (1+\omega_1)^2 - S_1(1-\omega_1)^2}{(1-\omega_1)^2(1+\omega_1)} \\
t_0 &= K\frac{\gamma\omega_1^2(1+\omega_1) + \omega_1(1+\omega_1^2 + S_1(1-\omega_1^2))}{(1-\omega_1)^2(1+\omega_1)} \\
g_{4t} &= \frac{-t_0}{\delta^3}, \quad g_{2t} = \frac{-t_2}{\delta}, \quad g_{0t} = -t_4\delta \\
K &= \frac{2\delta^2 + \omega_1^2 + 1}{2}, S_1 = \frac{\omega_1^2 - 1}{4K}, \gamma = \frac{2}{1+\omega_1}\sqrt{1 - S_1^2}.
\end{aligned}
\tag{B.4}
$$

Equating this filtering function with the transfer function in (5.5), the following equations are obtained:

$$g_2/g_4 = g_{2t}/g_{4t} = \delta^2 t_2/t_0$$
$$g_0/g_4 = g_{0t}/g_{4t} = \delta^4 t_4/t_0.$$

(B.5)

From these equations, it is easy to derive the design expressions to calculate the values of Z_{0_a} and Z_{0_b} as a function of the coupling factor c as follows

$$\bar{Z}_{0_a}^4 - \frac{g_{2t}(1-c^2) + g_{0t}c^2}{g_{0t}c^2} \bar{Z}_{0_a}^2 + \frac{g_{4t}(1-c^2)}{g_{0t}c^4} = 0$$

(B.6a)

$$\bar{Z}_{0_b} = \frac{-g_{0t}c^3 \bar{Z}_{0_a}^3}{2g_{4t}(1-c^2)}.$$

(B.6b)

Appendix C

Analytical Solution to the Quartic Equation of Chapter 5, Prototype II

Given the quartic equation

$$a_4 x^4 + a_3 x^3 + a_2 x^2 + a_1 x + a_0 = 0 \tag{C.1}$$

with $a_4 \neq 0$, the four roots are determined as

$$x_1 = -\frac{a_3}{4a_4} - S + \frac{1}{2}\sqrt{-4S^2 - 2p + \frac{q}{S}} \tag{C.2a}$$

$$x_2 = -\frac{a_3}{4a_4} - S - \frac{1}{2}\sqrt{-4S^2 - 2p + \frac{q}{S}} \tag{C.2b}$$

$$x_3 = -\frac{a_3}{4a_4} + S + \frac{1}{2}\sqrt{-4S^2 - 2p - \frac{q}{S}} \tag{C.2c}$$

$$x_4 = -\frac{a_3}{4a_4} + S - \frac{1}{2}\sqrt{-4S^2 - 2p - \frac{q}{S}}, \tag{C.2d}$$

where

$$
\begin{aligned}
p &= \frac{8a_4 a_2 - 3a_3^2}{8a_4^2} \\
q &= \frac{a_3^3 - 4a_4 a_3 a_2 + 8a_4^2 a_1}{8a_4^3} \\
S &= \frac{1}{2}\sqrt{-\frac{2}{3}p + \frac{1}{3a_4}\left(Q + \frac{\Delta_0}{Q}\right)},
\end{aligned}
\tag{C.3}
$$

and where

$$Q = \sqrt[3]{\frac{\Delta_1 + \sqrt{\Delta_1^2 - 4\Delta_0^3}}{2}}$$

$$\Delta_0 = a_2^2 - 3a_3a_1 + 12a_4a_0$$

$$\Delta_1 = 2a_2^3 - 9a_3a_2a_1 + 27a_3^2a_0 + 27a_4a_1^2 - 72a_4a_2a_0.$$

(C.4)

If the discriminant Δ, defined as

$$\Delta = \frac{\Delta_1^2 - 4\Delta_0^3}{-27}$$

(C.5)

is greater that 0, then Q is a complex number, and S must be recalculated as

$$S = \frac{1}{2}\sqrt{-\frac{2}{3}p + \frac{2}{3a_4}\sqrt{\Delta_0}\cos\frac{\phi}{3}},$$

(C.6)

where

$$\phi = \arccos\left(\frac{\Delta_1}{2\sqrt{\Delta_0^3}}\right).$$

(C.7)

It is worthy to mention that, if the value of q is negative, x_1 (C.2a) must be chosen as the correct solution, but if it is positive, x_3 (C.2c) will be the chosen solution for the synthesis procedure.

Appendix D

Publications Derived From This Thesis

Journals

[1] M. Pérez-Escribano and E. Márquez-Segura, "Random Errors in Broadband Characterization of the Propagation Constant of Transmission Lines Using Multiple Two-Port Measurements," in *IEEE Access*, vol. 9, pp. 59038-59047, 2021, doi: 10.1109/ACCESS.2021.3073173.

[2] M. Pérez-Escribano and E. Márquez-Segura, "Parameters Characterization of Dielectric Materials Samples in Microwave and Millimeter-Wave Bands," in *IEEE Transactions on Microwave Theory and Techniques*, vol. 69, no. 3, pp. 1723-1732, March 2021, doi: 10.1109/TMTT.2020.3045211.

[3] J. J. Sánchez-Martínez, M. Pérez-Escribano and E. Márquez-Segura, "Synthesis of Dual-Band Bandpass Filters With Short-Circuited Multiconductor Transmission Lines and Shunt Open Stubs," in *IEEE Access*, vol. 7, pp. 24071-24081, 2019, doi: 10.1109/ACCESS.2018.2886657.

Conferences

[1] M. Pérez-Escribano, F. J. Martín-Bayona, E. Márquez-Segura, "Efectos de la Conductividad en la Estimación de los Parámetros de Propagación de una Línea Stripline Fabricada Mediante Impresión de Tintas Conductoras," *Proceedings of*

the XXXVI Simposium Nacional de la Unión Científica Internacional de Radio (URSI), 20-24 septiembre 2021, Vigo, España.

[2] F. J. Martín-Bayona, G. Villalba-Calvillo, M. Pérez-Escribano, J. Oliva, A. Rojas, S. Cobos, E. Márquez-Segura, "Desarrollo e Integración de un Sensor Modular y Flexible en la Banda de Ondas Milimétricas para Aplicaciones de Automoción," *Proceedings of the XXXV Simposium Nacional de la Unión Científica Internacional de Radio (URSI)*, 2-4 septiembre 2020, Málaga, España.

[3] M. Pérez-Escribano, E. Márquez-Segura, "Caracterización en Banda Ancha de la Constante de Propagación de Materiales de Impresión 3D," *Proceedings of the XXXV Simposium Nacional de la Unión Científica Internacional de Radio (URSI)*, 2-4 septiembre 2020, Málaga, España.

[4] M. Pérez-Escribano, E. Márquez-Segura, J. J. Sánchez-Martínez, "Diseño analítico de filtros multibanda con líneas de transmisión multiconductoras y stubs en abierto," *Proceedings of the XXXIV Simposium Nacional de la Unión Científica Internacional de Radio (URSI)*, 4-6 septiembre 2019, Sevilla, España.

[5] M. Pérez-Escribano, J. J. Sanchez-Martínez and E. Márquez-Segura, "Small Size Dual-Band Bandpass Filters with Multiconductor Transmission Lines and Shunt Open Stubs," *2018 48th European Microwave Conference (EuMC)*, 2018, pp. 962-965, Madrid, doi: 10.23919/EuMC.2018.8541421.

Appendix E

Summary in Spanish

E.1   Resumen general

En esta tesis doctoral se han estudiado varias técnicas para la caracterización de líneas de transmisión. A partir de la medida de parámetros S de 2 puertos de líneas de distinta longitud es posible estimar la constante de propagación de dichas líneas. Para cada una de las técnicas de caracterización estudiadas se realiza un análisis de errores que incluye diversas fuentes de error, con el objetivo de poder detectar las causas que provocan inexactitudes en la estimación. A partir de este análisis, se proponen varias formas de mejorar la forma de actuación y el ancho de banda de los métodos estudiados. Posteriormente, estos métodos se utilizan con dos fines: por un lado, caracterizar las propiedades electromagnéticas de varias muestras de materiales elaborados mediante fabricación aditiva. Por otro lado, caracterizar la constante de propagación de los modos par e impar de líneas de microstrip acopladas, utilizando la medida parámetros S en *pure-mode*. Finalmente, un caso especial de líneas acopladas, como son las líneas de transmisión multiconductoras con líneas alternas interconectadas, se utiliza para sintetizar respuestas de filtros paso banda de dos o más bandas. Todos los circuitos y métodos propuestos en esta tesis han sido validados mediante trabajo experimental, el cual muestra una excelente concordancia entre los resultados analíticos, simulados y medidos. Este hecho prueba la fiabilidad del trabajo presentado.

E.2 Introducción

E.2.1 Marco contextual

El mundo está experimentando grandes cambios en los últimos años que afectan nuestro estilo de vida. La tendencia actual en la sociedad es acercar de una u otra forma todos los puntos del mundo, ya sea física o virtualmente. Sin embargo, los avances en movilidad deben ir acompañados de avances en las comunicaciones para que puedan ser efectivos. Estas comunicaciones deben ser accesibles para todos, independientemente del lugar o la situación económica. Para ello se deben producir ciertos cambios, que serán especialmente notables cuando afecten a los sistemas de comunicación.

Más allá de la globalización de las comunicaciones, los sistemas son cada vez más complejos y sus requisitos crecen exponencialmente. Cuando la implementación de la quinta generación de redes de comunicaciones móviles (5G) aún está comenzando en muchas ciudades del mundo, empiezan los estudios preliminares sobre las redes de sexta generación [1]. El principal requisito de las nuevas redes es un aumento considerable de la tasa de bits. Se espera que en 6G se puedan alcanzar tasas de 1 Tb/s. En el campo de la radiofrecuencia, las microondas y las ondas milimétricas, que son el tema principal de esta tesis, un aumento en la tasa de bits se convierte en un aumento considerable en el ancho de banda utilizado. Para lograr esto, no hay más remedio que utilizar frecuencias más altas. Por ejemplo, los sistemas 5G tienen aplicaciones en la banda E (60 GHz). Más allá, se espera que los sistemas 6G utilicen las bandas de THz (por debajo de 300 GHz), incluyendo ondas milimétricas para el acceso móvil. Este es solo un ejemplo de cómo los sistemas de comunicaciones, su ancho de banda y sus especificaciones están creciendo exponencialmente.

Estos nuevos requisitos van acompañados de funcionalidades, como el bajo costo, amplios anchos de banda, ligereza, facilidad de fabricación o fácil integración, que debe cumplir un sistema a comercializar. En este sentido, surgen constantemente nuevos materiales y técnicas de fabricación, que pueden utilizarse en los sistemas de comunicación. De cara a la llegada de estos nuevos materiales, es fundamental contar con una caracterización precisa de sus propiedades, para poder utilizarlos en la implementación de elementos de sistema como filtros, líneas de transmisión, guías de ondas o antenas.

Uno de los problemas a los que se enfrentan los diseñadores es tener un conocimiento exacto del comportamiento electromagnético de las estructuras y sustratos utilizados

para implementar dispositivos. En este sentido, las técnicas de caracterización son necesarias para el diseño de circuitos de microondas con especificaciones de alta exigencia, como acopladores direccionales y filtros de banda ancha. Es por ello que, desde la década de 1960, se han propuesto métodos para la caracterización de la constante de propagación de líneas de transmisión. Las primeras técnicas se basaron en el uso de reflectómetros [2]. Posteriormente, en 1975, Bianco y Parodi propusieron un método para la estimación de la constante de propagación [3] basado en la medición del coeficiente de reflexión a la entrada de cuatro líneas de transmisión, igualmente terminadas, de diferentes longitudes. Esta idea, así como algunas variaciones que incluyen medidas en transmisión, se han utilizado en numerosos estudios para caracterizar la constante de propagación [4, 5]. Además, se han propuesto varias mejoras estadísticas, que generalmente se basan en aumentar el número de longitudes distintas a medir [6].

Volviendo a los nuevos materiales y técnicas de fabricación, en los últimos años, las técnicas de fabricación han destacado en muchos campos científicos. Específicamente, en el área de microondas y ondas milimétricas, dispositivos como líneas de transmisión [7] o antenas [8] han sido fabricados utilizando tecnologías de impresión 3D. Una de las grandes ventajas es la posibilidad de sintetizar diferentes permitividades relativas utilizando el mismo material, variando simplemente el relleno de impresión, lo que determinará la cantidad de aire que queda dentro de la estructura impresa [9]. Sin embargo, estos materiales no están diseñados específicamente para implementar dispositivos de radiofrecuencia. Por ello, es necesario buscar técnicas de caracterización precisas que permitan obtener las propiedades electromagnéticas del material (permitividad relativa y tangente de pérdidas) en banda ancha. Una posible opción es realizar una medición directa de los materiales, como la propuesta en [10]. Otra opción es el uso de medidas indirectas, que hacen uso de un analizador de redes vectorial, como la descrita en [11].

Otra opción en la que centrarse para mejorar el rendimiento de los dispositivos es aumentar el número de conductores. Con esta configuración se pueden lograr respuestas mucho más selectivas, mayores anchos de banda o dispositivos diferenciales [12]. Sin embargo, es muy importante contar una caracterización precisa de los modos que se propagan a través de una estructura de líneas acopladas. Es por eso que también se han utilizado métodos de caracterización para obtener las constantes de propagación y las impedancias de un par de líneas acopladas [13]. Cuando se usan más de dos líneas, la estructura se suelen llamar líneas de transmisión multiconductoras. Con esta topología, aumenta la viabilidad del diseño. En [14], los autores propusieron unas estructura de líneas multiconductoras con líneas alternas interconectadas, que se utiliza

para eliminar resonancias no deseadas en el condensador interdigital tradicional. Los autores lo llamaron *wirebonded interdigital capacitor*. En [15] se presentó un modelo analítico de ese circuito para un número par de líneas, mientras que en [16] se analizó un modelo generalizado para un número par o impar de líneas. En este sentido, los autores demostraron que las líneas de transmisión muticonductoras son aptas para diseñar o mejorar el rendimiento de circuitos de microondas, ya que se puede obtener una gran variedad de factores de acoplamiento e impedancias, y existe un modelo analítico que permite manipular la estructura incluso sin el uso de simulaciones electromagnéticas. Usando líneas de transmisión multiconductores con líneas alternas interconectadas, dispositivos como desfasadores [17], *baluns* [18], *stubs* [19] o filtros cuasi elípticos [20], fueron propuestos por Juan José Sánchez Martínez y Enrique Márquez Segura.

E.2.2   Génesis

El núcleo de esta tesis doctoral surgió en el contexto de un proyecto de investigación cuyo principal objetivo era explorar nuevas técnicas de fabricación de dispositivos de microondas y ondas milimétricas. En este sentido, el laboratorio de investigación contaba con capacidades de fabricación aditiva 2D (Fujifilm Dimatix DMP-2850) y 3D (Ultimaker 3). Sin embargo, se habían realizado pocas investigaciones previas en este ámbito, por lo que uno de los puntos de partida fue poner en funcionamiento los equipos de fabricación.

Cuando comenzaron a desarrollarse los primeros dispositivos, nos dimos cuenta de que el primer paso debía ser conocer y caracterizar las propiedades electromagnéticas de los materiales que teníamos disponibles en el laboratorio. Por eso se inició la investigación de métodos para estimar la constante de propagación que nos permitieran caracterizar las estructuras fabricadas. Para ello, se decidió elegir métodos de banda ancha basados en el propuesto por Biancco y Parodi [3], ya que el grupo de investigación tenía mucha experiencia previa en este tipo de métodos y medidas.

Por otro lado, en base a los excelentes resultados obtenidos en la tesis doctoral de Juan José Sánchez Martínez, se decidió continuar con la línea de investigación de líneas de transmisión multiconductoras para la realización de circuitos de microondas. En este caso, para desarrollar nuevos dispositivos que hagan uso de los modelos analíticos previamente creados en el grupo de investigación. La idea es que, en el futuro, se puedan desarrollar dispositivos de línea multiconductores utilizando tecnologías de fabricación aditiva, combinando así los dos grandes bloques temáticos de esta tesis doctoral.

E.2.3 Objetivos

Como se describió en las secciones anteriores, la caracterización de la constante de propagación es extremadamente importante para el diseño de dispositivos de microondas y de ondas milimétricas. Además, esta caracterización es fundamental cuando se desconocen las propiedades de los sustratos utilizados, ya que estas deben utilizarse para poder llevar a cabo simulaciones electromagnéticas. Considerando la robustez de los métodos para la estimación de la constante de propagación, estos serán el punto de partida de esta tesis doctoral.

En este contexto, el primer objetivo de este trabajo es estudiar y comparar varios métodos, así como posibles fuentes de errores aleatorios que afecten a la exactitud de los mismos. Del mismo modo, se propondrán mejoras que permitan lograr una mayor precisión al aplicar esos métodos. Posteriormente, estos métodos se utilizarán para caracterizar materiales novedosos, hechos a través de la técnica de fabricación aditiva. Por otro lado, se realizará una caracterización de la constante de propagación de los modos que se propagan en un par de líneas acopladas. Finalmente, el uso de estructuras de varios conductores se propondrá para desarrollar nuevas topologías de filtros para sintetizar respuestas de doble banda y multi banda, proporcionando siempre un modelo analítico que permita realizar diseños analíticos sin optimización. Toda la teoría presentada se evaluará con trabajo experimental.

E.2.4 Estructura de contenidos

Esta sección proporciona una explicación del esquema de tesis, incluyendo una breve descripción que destaca las principales contribuciones de cada capítulo.

El **Capítulo 2** comienza con una descripción de tres métodos usados tradicionalmente para caracterizar la constante de propagación de las líneas de transmisión. Estos métodos se basan en el propuesto por Bianco y Parodi en [3], tomando medidas de parámetros S de 2 puertos de dos líneas con diferente longitud. Se aplica un análisis de errores a estos métodos, que incluye 4 posibles fuentes de error: errores del analizador de redes vectorial, errores en la longitud de las líneas, errores de repetibilidad del conector y errores de no homogeneidad del sustrato. Posteriormente, se propone una mejora estadística basada en un estimador de mínimos cuadrados, la cual consiste en incrementar el número de líneas a medir. Con esta mejora es posible reducir la varianza de la constante de propagación obtenida. La principal contribución de este capítulo es

la demostración de que la estrategia basada en autovalores es la menos afectada por los errores aleatorios.

Una vez que se han presentado los métodos, en el **Capítulo 3**, son aplicados a una línea microstrip cargada con una pieza de algunos de los materiales realizados con fabricación aditiva. Posteriormente, se obtiene una estimación de la constante de propagación de la estructura completa. En este caso, dicha constante se verá afectada por las propiedades electromagnéticas (permitividad relativa y tangente de pérdidas) de la parte superior. Sin embargo, conociendo la altura de ambos sustratos y la permitividad relativa inferior, es posible obtener una aproximación bastante precisa de las propiedades del material colocado en la parte superior. Se fabrican varias muestras de material para validar el método modificado presentado. La principal contribución de este capítulo es proponer el HIPS como un muy buen material para construir estructuras como circuitos o antenas, debido a sus bajas pérdidas y su permitividad relativa cercana a 2.4.

En el **Capítulo 4**, el método citado anteriormente se aplica a un par de líneas microstrip acopladas. En este caso, en lugar de medir los parámetros S en modo *single-ended*, se miden en *pure-mode*. Con este tipo de mediciones es posible excitar por separado los modos par e impar de la estructura y extraer los parámetros S correspondientes a cada modo. Posteriormente, estas matrices se consideran como una línea de transmisión de 2 puertos equivalente, a la que se le aplicará el método propuesto. La principal contribución de este capítulo es haber demostrado que reducir el ángulo de los codos en las líneas de alimentación es una forma sencilla de mejorar considerablemente la estimación de la constante de propagación, ya que su radiación limita fuertemente el ancho de banda de las constantes de fase y atenuación obtenidas.

El **Capítulo 5** presenta tres topologías diferentes para diseñar de forma sencilla filtros paso banda de doble banda y multi banda, utilizando líneas de transmisión multiconductoras cortocircuitadas y con líneas alternas interconectadas entre sí y *stubs* en abierto. Utilizando las dos primeras configuraciones propuestas es posible sintetizar funciones de filtrado de tipo Chebyshev, permitiendo además obtener anchos de banda estrechos o moderadamente anchos. La tercera configuración consiste en incrementar el número de *stubs* para lograr respuestas multi banda. Los resultados de los prototipos fabricados muestran una excelente concordancia con el modelo analítico propuesto. Por lo tanto, la principal contribución de este capítulo es haber propuesto una topología novedosa y su modelo analítico para diseñar filtros de doble banda y multi banda sin realizar ninguna optimización o simulación electromagnética, solo usando el conjunto

de ecuaciones propuesto para diseñar los filtros con la respuesta deseada.

Finalmente, el **Capítulo 6** resume los principales resultados y destaca las contribuciones más importantes logradas en cada capítulo de esta tesis doctoral. El manuscrito concluye con la propuesta de algunas ideas para continuar este trabajo en el futuro.

Además, se incluyen tres apéndices para ampliar los contenidos proporcionados. El Apéndice A muestra la influencia de la conductividad en los métodos propuestos para la estimación de la constante de propagación. Se demuestra que el efecto es similar al provocado por los errores en las longitudes de las líneas. El Apéndice B muestra el desarrollo matemático realizado para obtener las funciones de filtrado del primer prototipo del Capítulo 5. El Apéndice C describe la solución analítica de una ecuación genérica de cuarto orden, y luego aplica dicha solución a la función de filtrado del segundo prototipo de filtro presentado en el Capítulo 5. Las publicaciones derivadas de esta tesis se enumeran en el Apéndice D.

E.3 Métodos de caracterización y sus fuentes de error

La determinación experimental de la constante de propagación de líneas de transmisión planas es extremadamente importante en el diseño de circuitos de microondas y de ondas milimétricas. En los últimos años, ante la inminente llegada de nuevos materiales utilizados para fabricar circuitos de microondas, ha habido varios estudios que se han basado en la medición de la constante de propagación para extraer las propiedades electromagnéticas de estos materiales [10, 21, 22]. Los métodos disponibles para obtener la constante de propagación se pueden clasificar en varias categorías dependiendo del tipo de medidas consideradas [23]. La primera clasificación posible distingue entre métodos de banda ancha [3] y métodos resonantes [24]. Por un lado, los primeros métodos permiten caracterizar la constante de propagación en todo el rango de puntos de frecuencia medidos. Su principal inconveniente es su exactitud, que depende de la precisión de las medidas, mostrando un peor comportamiento, precisamente, en las resonancias. Por otro lado, los métodos resonantes permiten una estimación precisa de la constante de propagación en un conjunto discreto de puntos de frecuencia, aquellos en los que se produce una resonancia en la estructura de medida. Sin embargo, no pueden ser útiles cuando se requiere una caracterización de banda ancha. Desde otro punto de vista, otra clasificación distingue entre mediciones de 1 puerto [25] y de 2

puertos [26, 27].

E.3.1   Descripción de los métodos

Los métodos estudiados en esta tesis utilizan una configuración de medición como se muestra en la Fig. 2.1. Se miden los parámetros S de dos líneas de transmisión con diferentes longitudes y se calculan las matrices de parámetros de transmisión, $[M_1]$ y $[M_2]$. Dichas matrices de transmisión se pueden obtener fácilmente a partir de los parámetros S medidos utilizando las transformaciones propuestas en [38]:

$$T_{11} = \frac{1}{S_{21}} \qquad T_{12} = -\frac{S_{22}}{S_{21}}$$
$$T_{21} = \frac{S_{11}}{S_{21}} \qquad T_{22} = \frac{S_{12}S_{21} - S_{11}S_{22}}{S_{21}}. \tag{E.1}$$

Según la información mostrada en la Fig. 2.1, la conexión en cascada de las matrices de ambas líneas se puede expresar como $[M_1] = [R_A][L_1][R_B]$ y $[M_2] = [R_A][L_2][R_B]$. Las matrices $[L_1]$ y $[L_2]$ son las matrices de transmisión de las líneas medidas excluyendo las transiciones, cuyos efectos se consideran en las matrices R_A y R_B. Las matrices L_i para cada línea medida vienen dadas por

$$[L_i] = \begin{bmatrix} e^{\gamma l_i} & 0 \\ 0 & e^{-\gamma l_i} \end{bmatrix}. \tag{E.2}$$

Las matrices medidas $[M]$ se pueden combinar utilizando la expresión

$$[M_1][M_2]^{-1} = [R_A][L_1][L_2]^{-1}[R_A]^{-1}. \tag{E.3}$$

La ecuación (E.3) se puede reescribir como $[M] = [R_A][L][R_A]^{-1}$, donde $[M] = [M_1][M_2]^{-1}$ y $[L] = [L_1][L_2]^{-1}$. $[M]$ y $[L]$ son matrices similares y, en consecuencia, sus autovalores, trazas y determinantes coinciden. Como $[L]$ es una matriz diagonal, $[L] = \mathrm{diag}(e^{+\gamma\Delta l}, e^{-\gamma\Delta l})$, sus autovalores son $e^{+\gamma\Delta l}$ - y $e^{-\gamma\Delta l}$, respectivamente, y su traza es $e^{+\gamma\Delta l} + e^{-\gamma\Delta l}$. Estos valores son los mismos para $[M]$. Para obtener la constante de propagación, se pueden utilizar las invariantes mencionadas anteriormente. En este punto, se deben definir los tres métodos que se utilizarán para obtener la constante de propagación.

Método 1

Por un lado, debido a que la traza no cambia bajo una transformación de similaridad, se cumple la siguiente igualdad

$$\text{traza}([L]) = \text{traza}([M]) = e^{-\gamma\Delta l} + e^{+\gamma\Delta l}, \tag{E.4}$$

siendo $\Delta l = l_2 - l_1$. De esta forma, la constante de propagación se puede calcular como

$$\gamma = \frac{1}{\Delta l}\cosh^{-1}\left(\frac{\text{traza}\left([M_1]\,[M_2]^{-1}\right)}{2}\right). \tag{E.5}$$

Método 2

Por otro lado, los autovalores de $[M]$ son idénticos a los de $[L]$. Por lo tanto, si λ_1 y λ_2 son los autovalores de $[M]$, deben ser iguales a $e^{-\gamma\Delta l}$ y $e^{+\gamma\Delta l}$, respectivamente [39]. Resolviendo estas ecuaciones para γ, se obtiene

$$\gamma = \frac{1}{\Delta l}\ln\left(\frac{1}{\lambda_1}\right) = \frac{1}{\Delta l}\ln(\lambda_2). \tag{E.6}$$

En este caso, se pueden obtener dos valores diferentes para la constante de propagación. Un promedio de los autovalores de $[M]$, $1/2\,(1/\lambda_1 + \lambda_2)$, se puede usar para calcular γ, es decir,

$$\gamma = \frac{1}{\Delta l}\ln\left(\frac{1/\lambda_1 + \lambda_2}{2}\right). \tag{E.7}$$

Método 3

Comenzando de nuevo de una manera diferente [31], la suma de las matrices medidas, $[M_{1+2}] = [M_1] + [M_2]$, en lugar del producto, puede ser considerada y expresada como

$$[M_{1+2}] = R_A\begin{pmatrix} e^{+\gamma l_1}\left(1 + e^{+\gamma\Delta l}\right) & 0 \\ 0 & e^{-\gamma l_1}\left(1 + e^{-\gamma\Delta l}\right) \end{pmatrix}R_B. \tag{E.8}$$

Tomando el determinante de la matriz resultante en (E.8) y dividiéndolo por el determinante de $[M_1]$, el resultado es

$$\frac{\det\left([M_{1+2}]\right)}{\det\left([M_1]\right)} = \left(1 + e^{+\gamma\Delta l}\right)\left(1 + e^{-\gamma\Delta l}\right). \tag{E.9}$$

A partir de (E.9), la constante de propagación se puede obtener como

$$\gamma = \frac{1}{\Delta l}\cosh^{-1}\left(\frac{\det\left([M_{1+2}]\right)}{2\det\left([M_1]\right)} - 1\right). \tag{E.10}$$

Consideraciones de los métodos

Es importante considerar que z_i, el argumento de las funciones del método, es un número complejo definido como $z_i = r_i e^{j\theta_i}$. La función $\cosh^{-1}$ se puede reescribir como una función logarítmica dada por

$$\cosh^{-1}(z_i) = \ln(z_i + \sqrt{z_i - 1}\sqrt{z_i + 1}). \tag{E.11}$$

Por lo tanto, para cada método, la constante de propagación se puede expresar siempre como una función logarítmica que viene dada por

$$\gamma = \frac{1}{\Delta l}\left[\ln(r_i) + j(\theta_i + 2n\pi)\right], \tag{E.12}$$

siendo

$$\begin{aligned}
\alpha &= \frac{1}{\Delta l}\ln(r_i), \\
\beta &= \frac{1}{\Delta l}(\theta_i + 2n\pi).
\end{aligned} \tag{E.13}$$

Estas expresiones serán el punto de partida del análisis de sensibilidad del siguiente apartado, para saber cómo afectan los errores aleatorios a la constante de propagación. Es importante destacar que α tiene una solución única si $r \in R$, mientras que β tiene un número infinito de soluciones. Este hecho jugará un papel muy importante en la implementación de los métodos.

E.3.2   Análisis de sensibilidad con errores del VNA y de longitud de las líneas

Para el primer análisis de sensibilidad, se consideran dos fuentes de error, que son la longitud de las líneas y errores aleatorios del analizador de redes. Para ello, y buscando la covarianza de α y β, las derivadas de (E.13) con respecto a r, θ y Δl se puede expresar como

$$
\begin{aligned}
\frac{\partial \alpha}{\partial r} &= \frac{1}{r\Delta l} \\
\frac{\partial \alpha}{\partial \theta} &= 0 \\
\frac{\partial \alpha}{\partial \Delta l} &= -\frac{\ln(r)}{\Delta l^2} = -\frac{\alpha}{\Delta l} \\
\frac{\partial \beta}{\partial r} &= 0 \\
\frac{\partial \beta}{\partial \theta} &= \frac{1}{\Delta l} \\
\frac{\partial \beta}{\partial \Delta l} &= -\frac{\theta}{\Delta l^2}.
\end{aligned}
\tag{E.14}
$$

A partir de estas expresiones, y asumiendo que no hay covarianza entre los errores del analizador y los de longitud, las varianzas de las constantes de atenuación y fase vienen dadas por

$$
\begin{aligned}
\sigma_\alpha^2 &= \left|\frac{\partial \alpha}{\partial \Delta l}\right|^2 \sigma_{\Delta l}^2 + \left|\frac{\partial \alpha}{\partial r}\right|^2 \sigma_r^2 \\
&= \left|\frac{\alpha}{\Delta l}\right|^2 \sigma_{\Delta l}^2 + \left|\frac{1}{r\Delta l}\right|^2 \sigma_r^2,
\end{aligned}
\tag{E.15}
$$

$$
\begin{aligned}
\sigma_\beta^2 &= \left|\frac{\partial \beta}{\partial \Delta l}\right|^2 \sigma_{\Delta l}^2 + \left|\frac{\partial \beta}{\partial \theta}\right|^2 \sigma_\theta^2 \\
&= \left|\frac{\theta}{\Delta l^2}\right|^2 \sigma_{\Delta l}^2 + \left|\frac{1}{\Delta l}\right|^2 \sigma_\theta^2,
\end{aligned}
\tag{E.16}
$$

respectivamente. Como se ve en las expresiones desarrolladas, elegir un Δl más grande es la forma más sencilla de reducir las varianzas α y β.

Para cubrir todos los casos se ha realizado una simulación de Monte Carlo. Se utilizaron líneas de 10 y 35 mm de longitud, simuladas en RO4350B de 30 mils de altura, con un ancho de línea de 1.65 mm. Las desviaciones estándar se establecieron en

$\sigma_{|S|} = 0.1$ dB, $\sigma_{\phi S} = 5°$ y $\sigma_{\Delta l} = 0.02$ mm y se generaron errores usando una distribución gaussiana [41]. Las figuras 2.3 y 2.4 muestran la influencia de la magnitud y el error de fase para cada uno de los métodos. Como se ve, el Método 2, basado en autovalores es el que mejor comportamiento presenta, ya que no tiene resonancias y σ_α^2 es constante con la frecuencia.

E.3.3   Minimización de errores

Sobredeterminación

Para mejorar la precisión de los métodos, se propone aumentar el número de líneas a medir y utilizar una estimación por mínimos cuadrados. De esta manera, los efectos producidos por errores aleatorios en las mediciones se minimizan ya que el LMS es el estimador de máxima verosimilitud para una distribución normal.

Longitudes óptimas de las líneas

Una de las partes más importantes para reducir los errores aleatorios es la elección de las longitudes de las líneas empleadas. La distribución de la longitud debe elegirse de modo que las diferencias entre los incrementos de longitud sean lo más pequeñas posible. Además, cuanto mayores sean los incrementos, mejor. Los incrementos constantes de longitud entre diferentes líneas concentran las resonancias en un número discreto de puntos de frecuencia. Las longitudes seleccionadas se pueden escoger siguiendo una distribución cuasi lineal, como

$$l_i = l_0 + \Delta L \left(\frac{i-1}{N-1} \right)^q, i = 1, 2, ...N. \tag{E.17}$$

La Fig. 2.6 compara los histogramas de frecuencias donde hay $\pi/2$ de diferencia de fase entre los S_{21} medidos. Como se ve, $q = 1.2$ es la distribución más homogénea en todas las bandas de frecuencia, mientras que $q = 1$ muestra un comportamiento resonante.

E.3.4   Errores de repetibilidad del conector

Se presenta un análisis de la influencia de la repetibilidad del conector en los tres métodos previamente mencionados para estimar la constante de propagación. Para este propósito, se ha probado la repetibilidad de 16 transiciones utilizando conectores

coaxiales de 1.85 mm. Se ha demostrado que el uso del mismo kit de conectores en todas las líneas en lugar de varios kits distintos reduce significativamente la desviación estándar de los parámetros S de la transición transición, los cuales afectan a la estimación final de la constante de propagación, y especialmente la constante de atenuación. Además, se ha validado la hipótesis de que los datos medidos tienen una distribución de probabilidad gaussiana realizando un test de Anderson-Darling sobre los parámetros S de la transición. La desviación estándar obtenida se ha incluido en un análisis de sensibilidad, generando parámetros S a partir de una distribución normal y realizando una simulación de Monte Carlo, con el objetivo de estudiar la desviación estándar de la constante de propagación obtenida mediante los métodos propuestos cuando existen errores relacionados con la repetibilidad del conector. En este caso, a diferencia de los errores aleatorios del analizador, se ha encontrado que todas las estrategias comparadas para la estimación de la constante de propagación (trazas, autovalores y determinantes) funcionan de la misma forma con respecto a los errores de repetibilidad del conector. Además, se ha visto que la constante de propagación obtenida también sigue una distribución normal. Finalmente, para validar la teoría presentada, se han aplicado métodos a varias mediciones de dos líneas en el rango de frecuencia de 0.01 a 67 GHz, utilizando el mismo kit y diferentes combinaciones de conectores. Los resultados muestran que se obtiene una mayor precisión cuando se utiliza el mismo par de conectores, lo que reduce considerablemente el rizado de la constante de atenuación. Esto valida la idoneidad del análisis de error propuesto.

E.4 Caracterización de materiales realizados con fabricación aditiva

En este capítulo se aplica el Método 2 del capítulo anterior, basado en autovalores, para obtener la permitividad relativa de varias piezas de material realizado con la impresora 3D Ultikamer 3. Para ello, se propone una estructura microstrip multicapa que cuenta con un sustrato conocido y una pieza del material a caracterizar que se coloca encima de dicho sustrato. Primeramente se caracteriza el sustrato inferior y posteriormente estos datos se utilizan para caracterizar el sustrato superior.

E.4.1   Caracterización de la línea microstrip

Para caracterizar el sustrato inferior se fabrican 7 líneas microstrip sobre el sustrato Rogers 4350B LoPro, con 30 mil de espesor, $\varepsilon_{\mathrm{r}} = 3.66$, $\tan\delta = 0.0031$, y metalización de cobre de 17.5 μm de espesor. La longitud de las líneas, que se muestra en la leyenda de la Fig. 3.4, se calcula siguiendo el procedimiento cuasi lineal de $q = 1.2$. El ancho de línea se establece en 1.65 mm para obtener obtener una impedancia característica de 50 Ω.

El método de caracterización consiste en medir los parámetros S de las 7 líneas. Posteriormente, se aplica la ecuación

$$\min_{\alpha, \varepsilon_{\mathrm{r,eff}}} \frac{1}{2} \sum_{n=1}^{N} \left| \left(\frac{1/\lambda_1 + \lambda_2}{2} \right) - e^{+\gamma \Delta l} \right|^2, \tag{E.18}$$

para obtener α y $\varepsilon_{\mathrm{r,eff}}$, a partir de la cual se obtiene la permitividad nominal del sustrato, ε_{r}, incluyendo la dispersión, utilizando el modelo de Kirschning y Jansen [68]. Finalmente, la ε_{r} obtenida se importa en el simulador comercial [47] y se obtienen los resultados simulados de la estructura.

La Fig. 3.4 muestra la permitividad efectiva medida y simulada y la constante de atenuación obtenida mediante la aplicación del método al conjunto de 7 líneas. Además, también se muestra la información sobre la dispersión del sustrato proporcionada por el fabricante del material [40] hasta 50 GHz. Como se ve, existe una excelente concordancia entre la permitividad relativa efectiva medida y la obtenida por simulación utilizando datos del fabricante. En este sentido, se debe resaltar que la permitividad relativa, obtenida de la de la Fig. 3.4 (b) utilizando el modelo de Kirschning y Jansen y mostrada en la Fig. 3.4 (c), es bastante similar al dato proporcionado por Rogers, mostrando lo bueno que es el método propuesto para estimar dicho parámetro. Por esta razón, la ε_{r} obtenida se utilizará en la siguiente sección para la simulación de la estructura propuesta, con el fin de caracterizar con mayor precisión, incluida la dispersión del sustrato, las muestras de material.

E.4.2   Estimación de los parámetros del material

El montaje propuesto para la estimación de los parámetros dieléctricos consiste en una línea de microstrip cargada con una pieza hecha del material que se va a caracterizar. El esquema de medición se muestra en la Fig. 3.6. Como se ve, el dieléctrico de la

microstrip tiene una permitividad conocida ε_{r1}, estimada en la sección anterior, y una altura h_1, mientras que el material superior tiene una permitividad desconocida ε_{r2} y una altura conocida, h_2.

El procedimiento consiste en la determinación de la constante de propagación de la estructura completa y, luego, la extracción de la constante de atenuación y fase del material dieléctrico de la parte superior. Se han propuesto varios modelos numéricos para estimar la permitividad relativa efectiva de esta estructura, destacando [63,69]. Ambos modelos se basan en métodos numéricos y provienen de [70].

El problema con estos métodos es que la permitividad relativa estimada se calcula utilizando un modelo cuasi estático. Por eso, no tienen en cuenta la propia dispersión del material. Como se ve en la Fig. 3.4, la permitividad relativa tiene una ligera tendencia descendente con la frecuencia, y esta tendencia también aparecerá en los materiales de impresión. Por eso, se propone usar un modelo matemático que caracteriza esta curva decreciente entre las frecuencias mínima y máxima que el analizador usado permite medir. Este curva modelo se definirá como

$$\varepsilon_{ri} = \varepsilon_{r1} - \left(\varepsilon_{r67} - \varepsilon_{r1}\right) \left(\frac{i-1}{N-1}\right)^p, i = 1, N, \tag{E.19}$$

donde ε_{r1} y ε_{r67} son la permitividad relativa estimada a 1 GHz y 67 GHz respectivamente, y p es un factor cuasi lineal. Este valor puede ser $p = 1$ para un modelo lineal, $p = 2$ para un modelo cuadrático o un valor entre estos valores, que supondrá un modelo cuasi lineal. Después de comparar medidas y simulaciones, el valor $p = 1.5$ muestra que las diferencias que se logran son mínimas. Por lo tanto, se usará dicho parámetro para este modelo de dispersión cuasi lineal.

E.4.3 Consideración sobre las pérdidas obtenidas

Para determinar las pérdidas, el proceso constará de dos partes. Por un lado, será necesario determinar las pérdidas en los conductores. Para este proceso, se utilizará el modelo analítico presentado en [70] y mejorado en [71], que incluye el efecto de la rugosidad superficial. La rugosidad superficial de los conductores provoca que las pérdidas se incrementen ligeramente. Si no se considerara este efecto, la tangente de pérdidas estimada del sustrato superior sería mayor. Para comprobarlo, se han realizado algunas simulaciones. La Fig. 3.7 muestra la diferencia en la constante de atenuación estimada con y sin rugosidad superficial, usando HIPS como sustrato superior. Como

se ve, la rugosidad superficial aumenta la pendiente de la α estimada.

Una vez consideradas estas pérdidas, es necesario determinar las pérdidas en los dieléctricos. Este proceso se basa en encontrar la $\tan \delta_{eq}$ de ambos dieléctricos. Este modelo equivalente se definió en [72]. A partir de ella, conociendo la tangente de pérdidas del sustrato inferior $\tan \delta_1$, es posible obtener la tangente de pérdidas del sustrato superior $\tan \delta_2$. Este método proporciona un valor bastante exacto de la tangente de pérdidas para el sustrato superior. Además, nos permite distinguir entre valores cuya tangente de pérdidas es similar. Por ejemplo, la Fig. 3.8 muestra la constante de atenuación de dos estructuras. La primera tiene una tangente de pérdidas de 0.001, la segunda de 0.004 y la tercera de 0.01. Como se ve, la pendiente de la constante de atenuación es diferente. Es cierto que, a medida que disminuye el valor de la tangente de pérdidas, será más difícil diferenciar los valores, pero el método proporciona un valor bastante preciso.

E.5 Caracterización de líneas acopladas

En este caso, para la caracterización de la constante de propagación de los modos par e impar de líneas acopladas simétricas se vuelve a utilizar el mismo método anteriormente propuesto. Sin embargo, en este caso se toman medidas con el analizador en *pure-mode*, por lo que habrá que primero presentar cómo se hace la descomposición de los modos par e impar de la estructura.

E.5.1 Parámetros S diferenciales

Para medir los parámetros S de cada modo, a partir de los cuales se va a estimar su constante de propagación, se pueden utilizar parámetros S del modo mixto. Fueron introducidos por D. Bockelman y W. Eisenstadt en 1995 [92], para modelar circuitos y dispositivos diferenciales. Con estos parámetros es posible caracterizar más exactamente el comportamiento de los modos común y diferencial de este tipo de dispositivos [87]. Parten de una medición *single-ended* de un dispositivo de cuatro puertos ($[S_{se}]$), que transforman en un dispositivo equivalente con dos puertos que incluyen los modos diferencial y común ($[S_{mm}]$). La Fig. E.1 muestra un diagrama del funcionamiento de la medición de parámetros S en modo mixto, donde los cuatro puertos *single-ended* se convierten en dos puertos equivalentes, que excitan los modos diferencial y común de forma independiente.
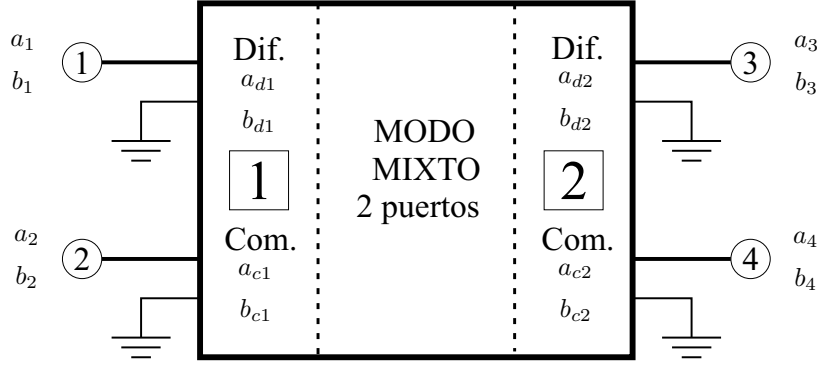
Figura E.1: Diagrama de medida de los parámetros S en modo mixto.

Los parámetros S en *single-mode* vienen dados por

$$
\begin{pmatrix} b_1 \\ b_2 \\ b_3 \\ b_4 \end{pmatrix} = \begin{pmatrix} S_{11} & S_{12} & S_{13} & S_{14} \\ S_{21} & S_{22} & S_{23} & S_{24} \\ S_{31} & S_{32} & S_{33} & S_{34} \\ S_{41} & S_{42} & S_{43} & S_{44} \end{pmatrix} \cdot \begin{pmatrix} a_1 \\ a_2 \\ a_3 \\ a_4 \end{pmatrix},
\tag{E.20}
$$

mientras que los del modo mixto por

$$
\begin{pmatrix} b_{d1} \\ b_{d2} \\ \hline b_{c1} \\ b_{c2} \end{pmatrix} = \left(\begin{array}{cc|cc} S_{dd11} & S_{dd12} & S_{11dc} & S_{12dc} \\ S_{dd21} & S_{dd22} & S_{21dc} & S_{22dc} \\ \hline S_{cd11} & S_{cd22} & S_{11cc} & S_{12cc} \\ S_{cd21} & S_{cd22} & S_{21cc} & S_{22cc} \end{array} \right) \cdot \begin{pmatrix} a_{1d} \\ a_{2d} \\ \hline a_{1c} \\ a_{2c} \end{pmatrix}.
\tag{E.21}
$$

La matriz en (E.21) se puede ver como cuatro submatrices correspondientes al modo diferencial (S_{dd}), el modo común (S_{cc}) y las submatrices S_{dc} y S_{cd}, que representan la transferencia de energía entre los modos diferencial y común. S_{dc} y S_{cd} generalmente se denominan matrices de modos cruzados (*cross-mode*). Las matrices (E.20) y (E.21) se pueden relacionar usando [92]

$$
[S_{mm}] = [M][S_{se}][M]^{-1},
\tag{E.22}
$$

siendo

$$[M] = \frac{1}{\sqrt{2}} \begin{pmatrix} 1 & -1 & 0 & 0 \\ 0 & 0 & 1 & -1 \\ 1 & 1 & 0 & 0 \\ 0 & 0 & 1 & 1 \end{pmatrix}. \tag{E.23}$$

En cierto modo, las líneas acopladas funcionan como dispositivos diferenciales, en los que el modo impar corresponde a una excitación diferencial, mientras que el modo par a una excitación en modo común, como se muestra en la Fig. E.2.
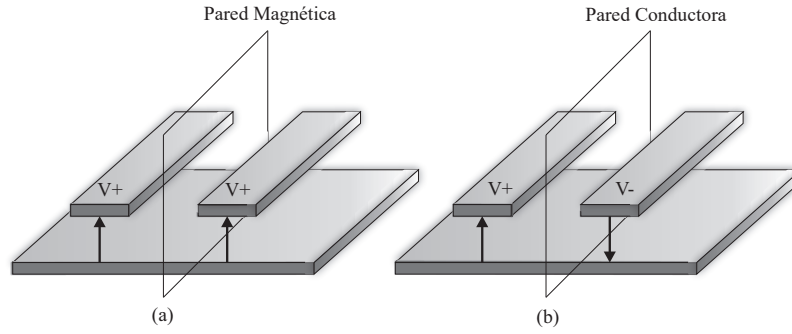
Figura E.2: Configuración de campos de los modos par (a) e impar (b) de las líneas acopladas.

Las matrices de modos cruzados son despreciables en las estructuras de líneas acopladas, por lo que $S_{ijd} = S_{ijdc} = 0 \forall i, j$, y las submatrices se pueden desacoplar como

$$\begin{pmatrix} b_{d1} \\ b_{d2} \end{pmatrix} = \begin{pmatrix} S_{dd11} & S_{dd12} \\ S_{dd21} & S_{dd22} \end{pmatrix} \cdot \begin{pmatrix} a_{1d} \\ a_{2d} \end{pmatrix}, \tag{E.24a}$$

$$\begin{pmatrix} b_{c1} \\ b_{c2} \end{pmatrix} = \begin{pmatrix} S_{cc11} & S_{cc12} \\ S_{cc21} & S_{cc22} \end{pmatrix} \cdot \begin{pmatrix} a_{1c} \\ a_{2c} \end{pmatrix}. \tag{E.24b}$$

Estos parámetros serán el punto de partida del método propuesto para la estimación de la constante de propagación: (E.24a) se utilizará para el modo impar y (E.24b) para el par. Los analizadores de redes actuales permiten medir directamente los parámetros S diferenciales, realizando internamente la transformación propuesta en (E.22), siempre que tengan la opción de realizar medidas en *pure-mode*.

E.5.2 Medidas del analizador en *pure-mode*

Las medidas en *pure-mode* se introdujeron en [94]. Para realizarlas, es necesario disponer de un analizador de redes vectorial que disponga de dicha opción. Para este tipo de medición hay que utilizar los cuatro puertos físicos de dicho analizador. La idea principal es generar los cuatro puertos virtuales que se muestran en la Fig. E.1 (dos para el modo común y dos para el modo diferencial). Para ello, debe asegurarse que entre los puertos físicos 1 y 2, y los puertos 3 y 4, exista una diferencia de fase de 0° y 180°. Si esto sucede, la estructura se excita en modo común o diferencial, respectivamente. A partir de esta excitación, es posible obtener directamente, desde el analizador, la matriz de parámetros S de modo mixto ($[S_{mm}]$). Es importante resaltar la necesidad de que el analizador tenga dos generadores de señales operando independientemente. Se demostró que la incertidumbre de dichas medidas es menor que las de las medidas tradicionales en *single-ended* de cuatro puertos y su posterior transformación cuando se realizan medidas de dispositivos diferenciales [87].

E.5.3 Consideraciones sobre la excitación de los modos

Uno de los problemas a la hora de medir las líneas es que es necesario colocar conectores. Estos conectores no caben en la configuración de dos líneas acopladas, por lo que habrá que buscar una configuración, basada en codos, que posibilite alimentar las líneas. Los codos se utilizan para separar correctamente los conectores y que se puedan conectar al analizador. Se presentan dos posibles configuraciones. Primero, se propone una estructura con dos codos de 90°, como se muestra en la Fig. 4.5 (a). Como todas las líneas de acceso son iguales, se garantiza que las líneas acopladas tendrán una alimentación de modo diferencial o común. Sin embargo, para las mediciones en *pure-mode* es necesario utilizar una calibración SOLT que compense las diferencias entre los puertos del analizador, para garantizar que los puertos puedan tener alimentaciones en modo diferencial o común. Esta es la principal diferencia en comparación con cuando se aplica el método propuesto a líneas de transmisión de 2 puertos.

El principal problema asociado con las codos son las pérdidas por radiación [95]. Estas pérdidas son especialmente significativas cuando el ángulo de las codos aumenta [96] y a altas frecuencias, cuando la longitud de las líneas entre las codos es comparable con la longitud de onda guiada. Por esta razón, se propone una configuración adicional con solo un codo de 30 °. Dicha configuración se muestra en la Fig. 4.5 (b). El codo de

30 ° también permite una correcta conexión con el analizador. Se pueden usar valores más bajos, pero 30° aporta un equilibrio entre los efectos parásitos admisibles y las longitudes razonables en las líneas microstrip de acceso.

Para comparar cómo las dos configuraciones pueden afectar al método presentado, se proponen dos figuras de mérito, que son claves para entender cómo funciona el método. Por un lado, la constante de atenuación depende, en gran medida, del valor absoluto de los parámetros S [50]. Para satisfacer la conservación de energía, la ecuación

$$\sum_{n=1}^{N} |S_{nm}|^2 \leq 1 \ \forall m \tag{E.25}$$

se debe cumplir en cada línea. Así, considerando que la estructura es recíproca, y para evaluar las pérdidas por radiación, el indicador Δ se puede definir como

$$\Delta = |S_{11_i}|^2 + |S_{21_i}|^2 + |S_{31_i}|^2 + |S_{41_i}|^2 \leq 1. \tag{E.26}$$

Por otro lado, la constante de fase depende de la diferencia de fase de dos líneas con diferente longitud. Por esta razón, el indicador δ se puede definir como

$$\delta = \angle S_{31_2} - \angle S_{31_1}. \tag{E.27}$$

Los dos indicadores definidos servirán para evaluar cómo los codos pueden afectar el comportamiento del método propuesto. La Fig. 4.6 muestra los indicadores Δ y δ para 2 líneas de 30° y 90°. El sustrato utilizado es el RO4350B de 20 mils, con líneas de 1.095 mm, un gap de 150 μm y longitudes de 10 y 35 mm respectivamente. Como puede verse, hay una disipación de potencia mucho mayor cuando se utilizan codos de 90°. Este comportamiento irregular hará que la constante de atenuación estimada se deteriore significativamente en alta frecuencia. Además, para esa configuración, la diferencia de fase no tiene un comportamiento lineal con la frecuencia, por lo que la constante de fase no se estimará correctamente en alta frecuencia. Por lo tanto, se espera que la configuración de curvas de 30° haga que el método funcione mejor.

E.6 Diseño de filtros multi banda usando líneas de transmisión multiconductoras

En el último capítulo teórico se proponen y analizan mediante ecuaciones dos topologías de filtros paso banda de doble banda y una toplogía multi banda usando líneas de transmisión multiconductoras cortocircuitadas con *stubs* paralelos en abierto. Mediante el uso de las arquitecturas propuestas, se pueden lograr filtros doble banda o multi banda con uno o dos polos en cada banda.

E.6.1 Filtros de doble banda
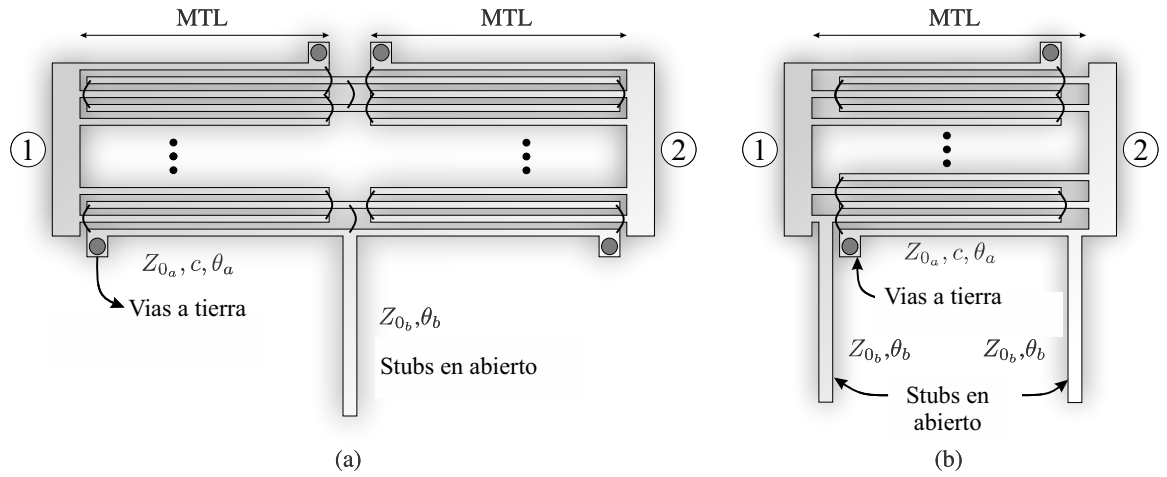
Figura E.3: Esquema circuital de los filtros propuestos: (a) prototipo I y (b) prototipo II.

Las topologías propuestas se muestran en la Fig. E.3. Para analizar estos circuitos se emplea el análisis de modo par e impar. Una vez que se calculan las impedancias de entrada par (Z_{in_e}) y modo impar (Z_{in_o}), los parámetros S de los filtros se determinan como

$$S_{11} = \frac{Z_{in_e}Z_{in_o} - Z_0^2}{\Delta}, \quad S_{21} = \frac{Z_0\left(Z_{in_e} - Z_{in_o}\right)}{\Delta}$$
$$\Delta = Z_0^2 + Z_0\left(Z_{in_e} + Z_{in_o}\right) + Z_{in_e}Z_{in_o}, \tag{E.28}$$

siendo Z_0 la impedancia característica utilizada para terminar los puertos de entrada y salida. Las expresiones se pueden simplificar si se hace que tanto las líneas de transmisión multiconducotras tengan una longitud eléctrica de cuarto de onda a la frecuencia media (f_o) de las dos bandas deseadas. Además, asumiendo propagación

TEM, se puede considerar

$$\theta_a = \theta_b = \theta = \theta_o \frac{f}{f_o} = \frac{\pi}{2} \frac{f}{f_o}.$$
(E.29)

A partir de (E.28) y después de algunas transformaciones algebraicas, la magnitud al cuadrado de los parámetros S_{11} y S_{21} se puede expresar como

Prototipo I

$$|S_{11}|^2 = \frac{F_I^2}{1 + F_I^2}, \quad |S_{21}|^2 = \frac{1}{1 + F_I^2}$$
(E.30a)

$$F_I = \frac{g_4 \tan^4 \theta + g_2 \tan^2 \theta + g_0}{\tan \theta \left(1 + \tan^2 \theta\right)}$$
(E.30b)

$$K_I = \frac{1}{2c^3 \bar{Z}_{0_a} \bar{Z}_{0_b}}$$
(E.30c)

$$g_4 = \bar{Z}_{0_a}^3 c^3 K_I$$
(E.30d)

$$g_2 = \left(\bar{Z}_{0_a} c + 2\bar{Z}_{0_b} c^2 \left(1 - \bar{Z}_{0_a}^2\right)\right) K_I$$
(E.30e)

$$g_0 = -2\bar{Z}_{0_b} \left(1 - c^2\right) K_I$$
(E.30f)

Prototipo II

$$|S_{11}|^2 = \frac{F_{II}^2}{1 + F_{II}^2}, \quad |S_{21}|^2 = \frac{1}{1 + F_{II}^2}$$
(E.31a)

$$F_{II} = \frac{p_4 \tan^4 \theta + p_2 \tan^2 \theta + p_0}{\tan^2 \theta \left(1/\sin \theta\right)}$$
(E.31b)

$$K_{II} = \frac{1}{2c^2 \bar{Z}_{0_a} \bar{Z}_{0_b}^2}$$
(E.31c)

$$p_4 = \bar{Z}_{0_a}^2 c^2 K_{II}$$
(E.31d)

$$p_2 = - \left(2\bar{Z}_{0_a} \bar{Z}_{0_b} c + \bar{Z}_{0_b}^2 c^2 \left(1 - \bar{Z}_{0_a}^2\right)\right) K_{II}$$
(E.31e)

$$p_0 = \bar{Z}_{0_b}^2 \left(1 - c^2\right) K_{II}$$
(E.31f)

donde

$$\bar{Z}_{0_a} = Z_{0_a}/Z_0, \quad \bar{Z}_{0_b} = Z_{0_b}/Z_0. \tag{E.32}$$

La respuesta en frecuencia de ambas estructuras está perfectamente caracterizada por medio de (E.30) y (E.31), y teniendo en cuenta la forma de F_I y F_{II}, diseñar filtros paso banda de doble banda con ceros de transmisión reales en $\theta_z = z\,\frac{\pi}{2}$ y $z = 0,1,2,$ ... es sencillo. Estos ceros de transmisión se utilizan para mejorar tanto el aislamiento entre las dos bandas de paso como el nivel de rechazo de los ceros. Dichos ceros de transmisión en $\theta_z = z\frac{\pi}{2}$, $z=0,2,4,...$ son inherentes a la línea multiconductora, mientras que los ceros en $\theta_z = z\frac{\pi}{2}$, $z=1,3$ ... son causados por los *stubs* en abierto. Además, debido al grado del numerador de F_I y F_{II} es cuatro, ambas estructuras son, a priori, adecuadas para sintetizar filtros paso banda de doble banda y cuarto orden. Añadiendo *stubs* de diferentes longitudes eléctricas, podría ser posible obtener respuestas de paso de banda multi banda, forzando ceros en la banda de paso de las líneas multiconductoras. No obstante, esta factibilidad dependerá de la realizabilidad física de los valores requeridos de Z_{0_a}, Z_{0_b} y c, lo que también condiciona los anchos de banda operativos y el ratio de frecuencias.

E.6.2 Ecuaciones de síntesis

Los parámetros de diseño Z_{0_a}, Z_{0_b} y c pueden calcularse fácilmente equiparando la función de transferencia de los circuitos (F_I, F_{II}) a las funciones de filtrado teóricas (F_n) como

$$\epsilon F_n(\theta) = F_{I,II}(\theta), \tag{E.33}$$

donde ϵ es el factor de rizado dentro de la banda, que viene dado por las pérdidas de retorno L_R deseadas en decibelios [136] y que se puede calcular como

$$\epsilon = \frac{1}{\sqrt{10^{L_R/10} - 1}}. \tag{E.34}$$

Para realizar la síntesis de los filtros se han calculado las siguientes ecuaciones:

Prototipo I

$$\bar{Z}_{0_b} = \frac{1 + b\epsilon}{2a\epsilon} \tag{E.35a}$$

$$c = \frac{1}{\sqrt{1 + b\epsilon}} \tag{E.35b}$$

$$\bar{Z}_{0_a} = 1/c. \tag{E.35c}$$

Prototipo II

$$\bar{Z}_{0_a} = \left(1 + \frac{4ab\sqrt{1 - c^2} - (4ab + 1)(1 - c^2)}{2b^2c^2}\right)^{\frac{1}{2}} \tag{E.36a}$$

$$\bar{Z}_{0_b} = \bar{Z}_{0_a} \frac{c}{\sqrt{1 - c^2}} \frac{b}{a} \tag{E.36b}$$

$$\epsilon = \frac{1 - c^2}{c^2} \frac{1}{4\bar{Z}_{0_a} b^2}, \tag{E.36c}$$

E.6.3   Filtros multi banda

Una posible modificación de la topología anterior podría ser añadir más *stubs* en paralelo para implementar filtros paso banda multi banda compactos. Además, se pueden añadir secciones de tipo *spur-line* para mitigar la primera réplica de la respuesta de frecuencia base de la estructura. La configuración circuital se muestra en la Fig. E.4.

E.7   Conclusiones y líneas futuras

Esta última sección resume el trabajo de investigación desarrollado durante la tesis doctoral y destaca los principales aportes. Por último, señala diferentes perspectivas de trabajo futuro a partir de la investigación desarrollada.
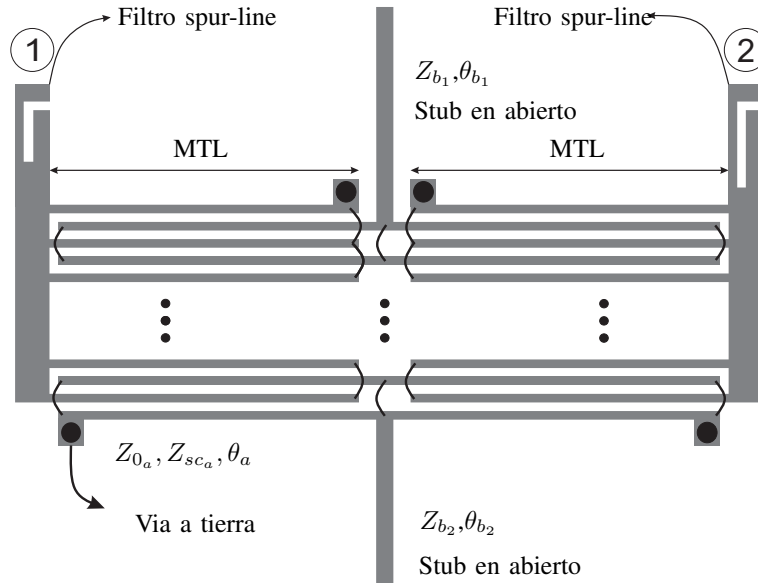
Figura E.4: Esquema del circuito propuesto para implementar filtros multi banda.

E.7.1   Contribuciones originales

A continuación se enumeran la síntesis y las principales aportaciones de esta tesis.

Caracterización de líneas de transmisión

Se han comparado tres métodos diferentes utilizados para la caracterización experimental de la constante de propagación de líneas de transmisión a partir de medidas en dos puertos. Aunque podría pensarse que estos tres métodos funcionan de forma similar, se ha demostrado que tienen un comportamiento totalmente diferente en presencia de errores. En este contexto, las principales aportaciones son:

- En cuanto a los errores aleatorios del analizador de redes, los métodos funcionan de forma totalmente diferente. La mejor estrategia es utilizar el método basado en autovalores, que es el único que no muestra un comportamiento resonante.

- En cuanto a las longitudes de línea y los errores de conductividad, funcionan como una desviación en la solución, siendo más significativos en frecuencias altas.

- En cuanto a los errores de repetibilidad de los conectores, todos los métodos funcionan de la misma manera. Utilizar el mismo kit de conectores para todas las medidas en lugar de varios kits diferentes en cada línea de transmisión es una

forma adecuada de reducir considerablemente la incertidumbre de la estimación final.

- Aumentar el número de líneas y utilizar un estimador de mínimos cuadrados es una buena forma de reducir la incertidumbre en la solución.

Caracterización de materiales de fabricación aditiva

Se ha propuesto una técnica sencilla para determinar las propiedades EM en banda ancha de los materiales de fabricación aditiva. Es muy útil y no se necesita calibración. Los resultados obtenidos muestran una excelente concordancia entre las medidas y las simulaciones, por lo que el procedimiento propuesto puede considerarse una buena y sencilla alternativa a los encontrados en el estado del arte. El modelo incluye los efectos de la dispersión del sustrato y de la rugosidad superficial de los conductores. Las principales contribuciones sobre este tema son:

- Los métodos permiten obtener resultados muy precisos en cuanto a la constante de atenuación y la permitividad dieléctrica efectiva utilizando pocas líneas.

- Se ha propuesto un criterio no lineal para elegir las longitudes de las líneas con el fin de minimizar los errores provocados por las resonancias.

- Se ha propuesto un modelo de dispersión para caracterizar la permitividad relativa de las muestras de material disponibles en todo el ancho de banda del analizador de redes utilizado (0.01-67 GHz).

- El material HIPS ha demostrado tener bajas pérdidas y puede establecerse como candidato para la fabricación de estructuras electromagnéticas debido a su tangente de pérdidas cercana a 0.004.

Caracterización de líneas microstrip acopladas

Se ha presentado un método para obtener en banda ancha la constante de propagación de los modos par e impar de un par de líneas microstrip simétricas acopladas, utilizando líneas de diferente longitud. Para ello se ha utilizado la medida de los parámetros S en *pure-mode* con el fin de obtener la matriz separada de cada modo. El método propuesto se ha validado mediante simulaciones y medidas, fabricando cuatro prototipos diferentes. Las principales aportaciones son:

- Se ha propuesto un método para caracterizar y obtener con precisión la constante de propagación en líneas acopladas, considerando ambos modos por separado.

- Se ha presentado un estudio riguroso y exhaustivo de la excitación de los modos, que muestra que los ángulos de los codos en las líneas de alimentación son críticos para la constante de atenuación. La constante de atenuación estimada es significativamente mejor cuando se utilizan ángulos de curvatura menores.

- Los resultados medidos son muy precisos en todo el ancho de banda del analizador utilizado (0.01-67 GHz), especialmente en la constante de fase. Esto supone un avance significativo en ancho de banda de caracterización para este tipo de estructuras.

Filtros paso banda multi banda

Se ha propuesto el uso de líneas de transmisión multiconductoras cortocircuitadas y *stubs* paralelos en abierto para sintetizar filtros paso banda compactos de doble banda. A partir de las ecuaciones analíticas obtenidas, se realiza un procedimiento de síntesis para obtener los parámetros de un filtro con la respuesta en frecuencia Chebyshev deseada. La teoría presentada se valida mediante el diseño, fabricación y medición de tres prototipos. La excelente concordancia entre el modelo analítico y las mediciones da a los diseñadores la confianza para utilizar el modelo propuesto. Además, se plantea una configuración adicional, que incluye varios *stubs* en abierto, y que permite obtener respuestas multi banda. Las réplicas inherentes a la estructura distribuida propuesta se pueden mitigar utilizando secciones de tipo *spur-line*. Las principales aportaciones sobre este tema son:

- Se ha propuesto una novedosa estructura para el diseño de filtros paso banda compactos, tanto de doble banda como multi banda, con buen rechazo fuera de banda. La teoría se ha evaluado mediante validación experimental.

- Se deriva un conjunto de ecuaciones para el diseño de filtros compactos paso banda de doble banda con una respuesta de tipo Chebyshev utilizando dos prototipos diferentes.

- Se propone una técnica de diseño de filtros que permite obtener fácilmente respuestas paso banda multi banda. Es posible seleccionar tanto el ancho de banda como la frecuencia central de cada banda.

E.7.2   Líneas futuras

A continuación se presentan algunas ideas y directrices breves como trabajo futuro que puede continuar al realizado en esta disertación:

- **Uso de técnicas de aprendizaje automático para la caracterización de líneas de transmisión**

  Las técnicas de aprendizaje automático están en auge en los últimos años en muchos campos de la ciencia, incluyendo las telecomunicaciones. Con ellas podrá ser posible estimar los principales parámetros de una línea de transmisión a partir de la medida de sus parámetros S, si previamente se ha entrenado un modelo con parámetros de otras líneas de transmisión. Con este procedimiento no sería necesario utilizar líneas de diferentes longitudes. Sin embargo, la precisión dependería de lo bien que se haya entrenado el modelo.

- **Caracterización de materiales en el espacio libre**

  El uso de muestras de materiales realizados con fabricación aditiva que se iluminan con una antena transmisora, para estudiar su transmisividad y reflectividad, debe ser explorado en el futuro. Para ello, se debe estudiar la variación de los parámetros S_{11} y S_{21} cuando el material se encuentra en la trayectoria directa entre las antenas emisora y receptora. A partir de esta variación, sería posible extraer las propiedades electromagnéticas del material.

- **Caracterización de las líneas acopladas asimétricas**

  La técnica propuesta en el Capítulo 4 se utiliza para caracterizar las constantes de propagación de las líneas acopladas simétricas. Sin embargo, habría que realizar una ampliación del método para poder explorar los modos C y π de estructuras microstrip acopladas asimétricas o no homogéneas. Para ello, sería necesario asegurar que la excitación de ambos modos se realiza correctamente.

- **Caracterización de líneas de transmisión multiconductoras**

  Otra posible aplicación a la técnica propuesta en el Capítulo 4 es caracterizar los modos de propagación en líneas de transmisión multiconductoras con líneas alternas interconectadas. Se debería realizar otro estudio para asegurar que la excitación de ambos modos se realiza correctamente.

- **Uso de *stubs* diseñados con líneas de transmisión multiconductoras para crear filtros paso banda de orden superior**

El uso de *stubs* basados en líneas de transmisión multiconductoras permite implementar niveles de impedancia que son inabordables con un solo *stub*, y que son de interés para el diseño de filtros. Se pueden utilizar en los filtros paso banda multi banda propuestos para conseguir respuestas más selectivas, ya que los *stubs* simples utilizados limitan el ancho de banda de los ceros de transmisión forzados dentro de la banda ancha de las líneas multiconductoras. El uso de *stubs* basados en líneas multiconductoras permitiría mejorar significativamente el rechazo entre bandas adyacentes.

- **Implementación de líneas de transmisión multiconductoras utilizando fabricación aditiva**
  En esta tesis se ha propuesto un prototipo de línea de transmisión stripline realizada mediante fabricación aditiva. Esta tecnología puede ser muy útil para la fabricación de líneas de transmisión multiconductoras. Sin embargo, será necesario mejorar los problemas encontrados, como la falta de homogeneidad de los sustratos y la conductividad de las tintas impresas. Si se consiguen superar estos problemas, será posible la fabricación e implementación de circuitos de microondas competitivos, como las topologías de filtro basadas en líneas multiconductoras desarrolladas en esta tesis, utilizando tecnologías de fabricación aditiva.

Bibliography

[1] W. Saad, M. Bennis, and M. Chen, "A vision of 6g wireless systems: Applications, trends, technologies, and open research problems," *IEEE Network*, vol. 34, no. 3, pp. 134--142, 2020.

[2] V. L. Carey, T. R. Scott, and W. T. Weeks, "Characterization of multiple parallel transmission lines using time domain reflectometry," *IEEE Transactions on Instrumentation and Measurement*, vol. 18, no. 3, pp. 166--171, 1969.

[3] B. Bianco and M. Parodi, "Measurement of the effective relative permittivities of microstrip," *Electronics Letters*, vol. 11, no. 3, pp. 71--72, February 1975.

[4] J. A. Reynoso-Hernandez, "Unified method for determining the complex propagation constant of reflecting and nonreflecting transmission lines," *IEEE Microwave and Wireless Components Letters*, vol. 13, no. 8, pp. 351--353, 2003.

[5] A. Hernández-Escobar, E. Abdo-Sánchez, J. Esteban, T. M. Martín-Guerrero, and C. Camacho-Peñalosa, "Broadband determination of the even- and odd-mode propagation constants of coupled lines based on two-port measurements," *IEEE Transactions on Microwave Theory and Techniques*, vol. 68, no. 2, pp. 648--654, Feb 2020.

[6] A. Hernández-Escobar, E. Abdo-Sánchez, J. Esteban, T. M. Martín-Guerrero, and C. Camacho-Peñalosa, "Broadband determination of the propagation constant of the slot mode of a rectangular waveguide," *IEEE Antennas and Wireless Propagation Letters*, vol. 19, no. 12, pp. 2423--2427, 2020.

[7] P. I. Deffenbaugh, T. M. Weller, and K. H. Church, "Fabrication and microwave characterization of 3-d printed transmission lines," *IEEE Microwave and Wireless Components Letters*, vol. 25, no. 12, pp. 823--825, Dec 2015.

[8] S. Moscato, R. Bahr, T. Le, M. Pasian, M. Bozzi, L. Perregrini, and M. M. Tentzeris, "Infill-dependent 3-d-printed material based on ninjaflex filament for antenna applications," *IEEE Antennas and Wireless Propagation Letters*, vol. 15, pp. 1506--1509, 2016.

[9] E. Massoni, L. Silvestri, M. Bozzi, L. Perregrini, G. Alaimo, S. Marconi, and F. Auricchio, "Characterization of 3d-printed dielectric substrates with different infill for microwave applications," in *2016 IEEE MTT-S International Microwave Workshop Series on Advanced Materials and Processes for RF and THz Applications (IMWS-AMP)*, 2016, pp. 1--4.

[10] P. I. Deffenbaugh, R. C. Rumpf, and K. H. Church, "Broadband microwave frequency characterization of 3-d printed materials," *IEEE Transactions on Components, Packaging and Manufacturing Technology*, vol. 3, no. 12, pp. 2147--2155, Dec 2013.

[11] G. A. Ramírez Arroyave and J. L. Araque Quijano, "Broadband characterization of 3d printed samples with graded permittivity," in *2018 International Conference on Electromagnetics in Advanced Applications (ICEAA)*, Sep. 2018, pp. 584--588.

[12] J. J. Sánchez-Martínez and E. Márquez-Segura, "Analytical design of wire-bonded multiconductor transmission-line-based ultra-wideband differential bandpass filters," *IEEE Trans. Microw. Theory Tech.*, vol. 62, no. 10, pp. 2308--2315, Oct 2014.

[13] M. Wojnowski, V. Issakov, G. Sommer, and R. Weigel, "Multimode trl calibration technique for characterization of differential devices," *IEEE Transactions on Microwave Theory and Techniques*, vol. 60, no. 7, pp. 2220--2247, 2012.

[14] F. Casares-Miranda, P. Otero, E. Márquez-Segura, and C. Camacho-Peñalosa, "Wire Bonded Interdigital Capacitor," *IEEE Microw. Wireless Compon. Lett.*, vol. 15, no. 10, pp. 700--702, Oct. 2005.

[15] E. Márquez-Segura, F. Casares-Miranda, P. Otero, C. Camacho-Peñalosa, and J. Page, "Analytical Model of the Wire-Bonded Interdigital Capacitor," *IEEE Trans. Microw. Theory Tech.*, vol. 54, no. 2, pp. 748--754, Feb. 2006.

[16] J. Page, E. Márquez-Segura, F. Casares-Miranda, J. Esteban, P. Otero, and C. Camacho-Peñalosa, "Exact Analysis of the Wire-Bonded Multiconductor

Transmission Line," *IEEE Trans. Microw. Theory Tech.*, vol. 55, no. 8, pp. 1585--1592, Aug. 2007.

[17] J. J. Sánchez-Martínez and E. Márquez-Segura, "Analytical Study of Wide-band Bandpass Filters Based on Wire-Bonded Multiconductor Transmission Lines With LH Behaviour," *Progress In Electromagnetics Research Letters*, vol. 31, pp. 1--13, 2012.

[18] ------, "Generalized analytical design of broadband planar baluns based on wire-bonded multiconductor transmission lines," *Progress In Electromagnetics Research*, vol. 134, pp. 169--187, 2013.

[19] J. J. Sánchez-Martínez, E. Márquez-Segura, and C. Camacho-Peñalosa, "Analysis of wire-bonded multiconductor transmission-line-based stubs," *IEEE Trans. Microw. Theory Tech.*, vol. 61, no. 4, pp. 1467--1476, Apr. 2013.

[20] J. J. Sánchez-Martinez, E. Márquez-Segura, and S. Lucyszyn, "Synthesis and design of high-selectivity wideband quasi-elliptic bandpass filters using multiconductor transmission lines," *IEEE Trans. Microw. Theory Tech.*, vol. 63, no. 1, pp. 198--208, Jan 2015.

[21] M. Cauwe and J. De Baets, "Broadband material parameter characterization for practical high-speed interconnects on printed circuit board," *IEEE Transactions on Advanced Packaging*, vol. 31, no. 3, pp. 649--656, 2008.

[22] M. Pérez-Escribano and E. Márquez-Segura, "Parameters characterization of dielectric materials samples in microwave and millimeter-wave bands," *IEEE Transactions on Microwave Theory and Techniques*, vol. 69, no. 3, pp. 1723--1732, 2021.

[23] L. Chen, C. Ong, C. Neo, V. Varadan, and V. Varadan, *Microwave Electronics: Measurement and Materials Characterization.* Wiley, 2004. [Online]. Available: https://books.google.es/books?id=1vmUdUXlBNIC

[24] V. Rizzoli, "Resonance measurement of single- and coupled-microstrip propagation constants," *IEEE Transactions on Microwave Theory and Techniques*, vol. 25, no. 2, pp. 113--120, Feb 1977.

[25] Woopoung Kim, Seock Hee Lee, Man Cheol Seo, M. Swaminathan, and R. R. Tummala, "Determination of propagation constants of transmission lines using

1-port tdr measurements," in *59th ARFTG Conference Digest, Spring 2002.*, 2002, pp. 6 pp.--.

[26] A. M. Nicolson and G. F. Ross, "Measurement of the intrinsic properties of materials by time-domain techniques," *IEEE Transactions on Instrumentation and Measurement*, vol. 19, no. 4, pp. 377--382, 1970.

[27] K. Fuh, "Broadband continuous extraction of complex propagation constants in methods using two-line measurements," *IEEE Microwave and Wireless Components Letters*, vol. 23, no. 12, pp. 671--673, 2013.

[28] G. F. Engen and C. A. Hoer, "Thru-reflect-line: An improved technique for calibrating the dual six-port automatic network analyzer," *IEEE Transactions on Microwave Theory and Techniques*, vol. 27, no. 12, pp. 987--993, 1979.

[29] R. B. Marks, "A multiline method of network analyzer calibration," *IEEE Transactions on Microwave Theory and Techniques*, vol. 39, no. 7, pp. 1205--1215, 1991.

[30] Y. Rodríguez-Velásquez, S. C. Sejas-García, and R. Torres-Torres, "A method of differences for determining the propagation constant from multiline measurements," *IEEE Microwave and Wireless Components Letters*, vol. 30, no. 3, pp. 300--303, 2020.

[31] C. Wan, B. Nauwelaers, W. De Raedt, and M. Van Rossum, "Two new measurement methods for explicit determination of complex permittivity," *IEEE Transactions on Microwave Theory and Techniques*, vol. 46, no. 11, pp. 1614--1619, 1998.

[32] J. van Heuven and T. Rozzi, "The invariance properties of a multivalue n-port in a linear embedding," *IEEE Transactions on Circuit Theory*, vol. 19, no. 2, pp. 176--183, 1972.

[33] P. M. Buff, J. Nath, and M. B. Steer, "Origin of the half-wavelength errors in microwave measurements using through–line calibrations," *IEEE Transactions on Instrumentation and Measurement*, vol. 56, no. 5, pp. 1610--1615, 2007.

[34] J. Juroshek, "A study of measurements of connector repeatability using highly reflecting loads (short paper)," *IEEE Transactions on Microwave Theory and Techniques*, vol. 35, no. 4, pp. 457--460, 1987.

[35] W. Daywitt, "A simple technique for investigating defects in coaxial connectors (short paper)," *IEEE Transactions on Microwave Theory and Techniques*, vol. 35, no. 4, pp. 460--464, 1987.

[36] A. Lewandowski and D. Williams, "Characterization and modeling of random vector network analyzer measurement errors," in *MIKON 2008 - 17th International Conference on Microwaves, Radar and Wireless Communications*, 2008, pp. 1--4.

[37] ------, "Stochastic modeling of coaxial-connector repeatability errors," in *2009 74th ARFTG Microwave Measurement Conference*, 2009, pp. 1--4.

[38] D. Frickey, "Conversions between s, z, y, h, abcd, and t parameters which are valid for complex source and load impedances," *Microwave Theory and Techniques, IEEE Transactions on*, vol. 42, pp. 205 -- 211, 03 1994.

[39] M. D. Janezic and J. A. Jargon, "Complex permittivity determination from propagation constant measurements," *IEEE Microwave and Guided Wave Letters*, vol. 9, no. 2, pp. 76--78, 1999.

[40] "Ro4000 series high frequency circuit materials," https://rogerscorp.com/-/media/project/rogerscorp/documents/advanced-electronics-solutions/english/data-sheets/ro4000-laminates-ro4003c-and-ro4350b---data-sheet.pdf, 2022.

[41] A. Lewandowski, W. Wiatr, and D. Williams, "Multi-frequency approach to vector-network-analyzer scattering-parameter measurements," in *The 40th European Microwave Conference*, 2010, pp. 260--263.

[42] D. F. Williams, C. M. Wang, and U. Arz, "An optimal multiline trl calibration algorithm," in *IEEE MTT-S International Microwave Symposium Digest, 2003*, vol. 3, 2003, pp. 1819--1822 vol.3.

[43] J. E. Zuniga-Juarez, J. A. Reynoso-Hernandez, and M. C. Maya-Sanchez, "An improved multiline trl method," in *2006 67th ARFTG Conference*, 2006, pp. 139--142.

[44] Southwest Microwave, Inc., "Typical test data," 2021. [Online]. Available: https://mpd.southwestmicrowave.com/product/1892-03a-6-end-launch-1-85mm-v-67-ghz-jack-female-standard-block/

[45] D. F. Williams, C. M. Wang, and U. Arz, "In-phase/quadrature covariance-matrix representation of the uncertainty of vectors and complex numbers," in *2006 68th ARFTG Conference: Microwave Measurement*, 2006, pp. 1--4.

[46] T. W. Anderson and D. A. Darling, "A test of goodness of fit," *Journal of the American Statistical Association*, vol. 49, no. 268, pp. 765--769, 1954. [Online]. Available: https://www.tandfonline.com/doi/abs/10.1080/01621459. 1954.10501232

[47] "Ansys hfss software," https://www.ansys.com/products/electronics/ansys-hfss, 2021.

[48] "Keysight 2-port and 4-port pna-x network analyzer," https://literature.cdn.keysight.com/litweb/pdf/N5247-90002.pdf, 2021.

[49] M. Steer, *Microwave and RF Design, Volume 2: Transmission Lines*, ser. Microwave and RF Design. University of North Carolina Press, 2019, no. v. 2. [Online]. Available: https://books.google.es/books?id=J3avxwEACAAJ

[50] M. Pérez-Escribano and E. Márquez-Segura, "Random errors in broadband characterization of the propagation constant of transmission lines using multiple two-port measurements," *IEEE Access*, vol. 9, pp. 59 038--59 047, 2021.

[51] E. Macdonald, R. Salas, D. Espalin, M. Perez, E. Aguilera, D. Muse, and R. B. Wicker, "3d printing for the rapid prototyping of structural electronics," *IEEE Access*, vol. 2, pp. 234--242, Dec 2014.

[52] M. M. Abdin, J. Castro, J. Wang, and T. Weller, "Miniaturized 3d printed balun using high-k composites," in *2015 IEEE 16th Annual Wireless and Microwave Technology Conference (WAMICON)*, April 2015, pp. 1--3.

[53] A. Jones, S. Lucyszyn, E. Márquez-Segura, N. Ridler, J. Skinner, and D. Stokes, "3-d printed primary standards for calibration of microwave network analyzers," *Measurement*, vol. 158, p. 107682, 2020. [Online]. Available: http://www.sciencedirect.com/science/article/pii/S0263224120302207

[54] E. Márquez-Segura, S.-H. Shin, A. Dawood, N. M. Ridler, and S. Lucyszyn, "Microwave characterization of conductive pla and its application to a 12 to 18 ghz 3-d printed rotary vane attenuator," *IEEE Access*, vol. 9, pp. 84 327--84 343, 2021.

[55] L. Catarinucci, R. Colella, P. Coppola, and L. Tarricone, "Microwave characterisation of polylactic acid for 3d-printed dielectrically controlled substrates," *IET Microwaves, Antennas Propagation*, vol. 11, no. 14, pp. 1970--1976, 2017.

[56] A. C. Paolella, C. Corey, D. Foster, J. Desjardins, C. Smith, and L. Walters, "Broadband millimeter wave characterization of 3-d printed materials," in *2018 IEEE/MTT-S International Microwave Symposium - IMS*, June 2018, pp. 1565--1568.

[57] K. Szostak and P. Słobodzian, "Broadband dielectric measurement of pcb and substrate materials by means of a microstrip line of adjustable width," *IEEE Microwave and Wireless Components Letters*, vol. 28, no. 10, pp. 945--947, 2018.

[58] W. Weir, "Automatic measurement of complex dielectric constant and permeability at microwave frequencies," *Proceedings of the IEEE*, vol. 62, no. 1, pp. 33--36, 1974.

[59] K. Andersson and C. Fager, "Statistical estimation of the propagation constant in multiline calibrations," in *2006 67th ARFTG Conference*, 2006, pp. 133--136.

[60] B. T. W. Gillatt, M. D'Auria, W. J. Otter, N. M. Ridler, and S. Lucyszyn, "3-d printed variable phase shifter," *IEEE Microwave and Wireless Components Letters*, vol. 26, no. 10, pp. 822--824, 2016.

[61] S. Lucyszyn, X. Shang, W. J. Otter, C. W. Myant, R. Cheng, and N. M. Ridler, "Polymer-based 3d printed millimeter-wave components for spacecraft payloads," in *2018 IEEE MTT-S International Microwave Workshop Series on Advanced Materials and Processes for RF and THz Applications (IMWS-AMP)*, 2018, pp. 1--3.

[62] E. García-Marín, E. Márquez-Segura, P. Sánchez-Olivares, J. L. Masa-Campos, J. A. Ruiz-Cruz, and C. Camacho-Peñalosa, "Ink-jet implementation of stacked-patch antenna for wireless applications," in *2019 IEEE MTT-S International Microwave Workshop Series on Advanced Materials and Processes for RF and THz Applications (IMWS-AMP)*, 2019, pp. 151--153.

[63] M. A. Couker and L. J. Kushner, "A microstrip phase-trim device using a dielectric overlay," *IEEE Transactions on Microwave Theory and Techniques*, vol. 42, no. 11, pp. 2023--2026, Nov 1994.

[64] R. A. Soares, P. Gouzien, P. Legaud, and G. Follot, "A unified mathematical approach to two-port calibration techniques and some applications," *IEEE Transactions on Microwave Theory and Techniques*, vol. 37, no. 11, pp. 1669--1674, 1989.

[65] R. R. Pantoja, M. J. Howes, J. R. Richardson, and R. D. Pollard, "Improved calibration and measurement of the scattering parameters of microwave integrated circuits," *IEEE Transactions on Microwave Theory and Techniques*, vol. 37, no. 11, pp. 1675--1680, 1989.

[66] Moon-Que Lee and Sangwook Nam, "An accurate broadband measurement of substrate dielectric constant," *IEEE Microwave and Guided Wave Letters*, vol. 6, no. 4, pp. 168--170, 1996.

[67] J. A. Reynoso-Hernandez, "Reliable method for computing the phase shift of multiline lrl calibration technique," *IEEE Microwave and Wireless Components Letters*, vol. 12, no. 10, pp. 395--397, 2002.

[68] M. Kirschning and R. H. Jansen, "Accurate model for effective dielectric constant of microstrip with validity up to millimetre-wave frequencies," *Electronics Letters*, vol. 18, no. 6, pp. 272--273, March 1982.

[69] M. Barbuto, A. Alù, F. Bilotti, and A. Toscano, "Characteristic impedance of a microstrip line with a dielectric overlay," *COMPEL: Int J for Computation and Maths. in Electrical and Electronic Eng.*, vol. 32, 11 2013.

[70] E. Hammerstad and O. Jensen, "Accurate models for microstrip computer-aided design," in *1980 IEEE MTT-S International Microwave symposium Digest*, May 1980, pp. 407--409.

[71] E. Y. Terán-Bahena, S. C. Sejas-García, and R. Torres-Torres, "Permittivity determination considering the metal surface roughness effect on the microstrip line series inductance and shunt capacitance," *IEEE Transactions on Microwave Theory and Techniques*, vol. 68, no. 6, pp. 2428--2434, 2020.

[72] A. K. Verma, Nasimuddin, and E. K. Sharma, "Analysis and circuit model of a multilayer semiconductor slow-wave microstrip line," *IEE Proceedings - Microwaves, Antennas and Propagation*, vol. 151, no. 5, pp. 441--449, 2004.

[73] "Copper foils for high frequency materials,"
www.rogerscorp.cn/documents/749/acs/Copper-Foils-for-High-Frequency-
Circuit-Materials.pdf.

[74] S. Groiss, I. Bardi, O. Biro, K. Preis, and K. R. Richter, "Parameters of lossy
cavity resonators calculated by the finite element method," *IEEE Transactions
on Magnetics*, vol. 32, no. 3, pp. 894--897, 1996.

[75] S. Kim and J. Baker-Jarvis, "An approximate approach to determining the
permittivity and permeability near $\lambda/2$ resonances in transmission/reflection
measurements," *Progress In Electromagnetics Research B*, vol. 58, pp. 95--109, 01
2014.

[76] N. Abdul Malek, A. Mohd Ramly, A. Sidek, and S. Mohamad, "Characterization
of acrylonitrile butadiene styrene for 3d printed patch antenna," *Indonesian
Journal of Electrical Engineering and Computer Science*, vol. 6, p. 116, 04 2017.

[77] C. Dichtl, P. Sippel, and S. Krohns, "Dielectric properties of 3d printed polylactic
acid," *Advances in Materials Science and Engineering*, vol. 2017, pp. 1--10, 07
2017.

[78] M. Gauthier, *Modern Styrenic Polymers: Polystyrenes and Styrenic Copolymers*.
ASM International, 1995.

[79] J. Scheirs and D. Priddy, *Modern Styrenic Polymers: Polystyrenes and Styrenic
Copolymers*. John Wiley and Sons, 2003.

[80] S. Kim, S. Jeon, and J. Jeong, "Compact two-way and four-way power dividers
using multi-conductor coupled lines," *IEEE Microwave and Wireless Components
Letters*, vol. 21, no. 3, pp. 130--132, 2011.

[81] A. R. Djordjević, V. Napijalo, D. I. Olćan, and A. Zajic, "Wideband multilayer
directional coupler with tight coupling and high directivity," *Microwave and
Optical Technology Letters*, vol. 54, pp. 2261--2267, 2012.

[82] R. S. Elliott, *An introduction to guided waves and microwave circuits / Robert S.
Elliott*. London: Prentice-Hall, 1993.

[83] V. Rizzoli, "Resonance measurement of even and odd mode propagation con-
stants in coupled microstrips," in *1975 IEEE-MTT-S International Microwave
Symposium*, 1975, pp. 106--108.

[84] J. Richings and B. Easter, "Measured odd- and even-mode dispersion of coupled microstrip lines (short papers)," *IEEE Transactions on Microwave Theory and Techniques*, vol. 23, no. 10, pp. 826--828, 1975.

[85] T.-M. Winkel, L. Dutta, H. Grabinski, and E. Groteluschen, "Determination of the propagation constant of coupled lines on chips based on high frequency measurements," in *Proceedings 1996 IEEE Multi-Chip Module Conference (Cat. No.96CH35893)*, 1996, pp. 99--104.

[86] K. Murakami, "Systematic mixed even- and odd-mode modeling of parallel tightly coupled transmission lines," in *2010 53rd IEEE International Midwest Symposium on Circuits and Systems*, 2010, pp. 153--156.

[87] D. Bockelman, W. Eisenstadt, and R. Stengel, "Accuracy estimation of mixed-mode scattering parameter measurements," *IEEE Trans. Microw. Theory Tech.*, vol. 47, no. 1, pp. 102--105, Jan. 1999.

[88] C.-C. Huang and Y.-C. Chen, "Differential- and common-mode characterization of coupled interconnect transmission lines using four-port s-parameter measurements," in *2010 5th International Microsystems Packaging Assembly and Circuits Technology Conference*, 2010, pp. 1--4.

[89] D. Williams and R. Marks, "Transmission line capacitance measurement," *IEEE Microwave and Guided Wave Letters*, vol. 1, no. 9, pp. 243--245, 1991.

[90] L. Wan, Q. Li, Z. Wang, and J. Wu, "Improved multimode trl calibration method for characterization of homogeneous differential discontinuities," *IEEE Transactions on Instrumentation and Measurement*, vol. 64, no. 3, pp. 694--703, 2015.

[91] M. Kirschning and R. Jansen, "Accurate Wide-Range Design Equations for the Frequency-Dependent Characteristic of Parallel Coupled Microstrip Lines," *IEEE Trans. Microw. Theory Tech.*, vol. 32, no. 1, pp. 83--90, Jan. 1984.

[92] D. Bockelman and W. Eisenstadt, "Combined differential and common-mode scattering parameters: theory and simulation," *IEEE Trans. Microw. Theory Tech.*, vol. 43, no. 7, pp. 1530--1539, Jul. 1995.

[93] A. Huynh, P. Hakansson, and S. Gong, "Mixed-mode s-parameter conversion for networks with coupled differential signals," in *2007 European Microwave Conference*, 2007, pp. 238--241.

[94] D. Bockelman and W. Eisenstadt, "Pure-mode network analyzer for on-wafer measurements of mixed-mode S-parameters of differential circuits," *IEEE Trans. Microw. Theory Tech.*, vol. 45, no. 7, pp. 1071--1077, Jul. 1997.

[95] A. Sabban and K. Gupta, "Characterization of radiation loss from microstrip discontinuities using a multiport network modeling approach," *IEEE Transactions on Microwave Theory and Techniques*, vol. 39, no. 4, pp. 705--712, 1991.

[96] X. Liu, C. Christopoulos, and D. Thomas, "Prediction of radiation losses and emission from a bent wire by a network model," *IEEE Transactions on Electromagnetic Compatibility*, vol. 48, no. 3, pp. 476--484, 2006.

[97] D. Pozar, *Microwave Engineering*, 2nd ed. New York: Wiley, 1998.

[98] E. Hammerstad and O. Jensen, "Accurate models for microstrip computer-aided design," in *1980 IEEE MTT-S International Microwave symposium Digest*, 1980, pp. 407--409.

[99] L. Kong and X. Xu, "A compact dual-band dual-polarized microstrip antenna array for mimo-sar applications," *IEEE Trans. Antennas Propag.*, vol. 66, no. 5, pp. 2374--2381, May 2018.

[100] A. Toktas and A. Akdagli, "Compact multiple-input multiple-output antenna with low correlation for ultra-wide-band applications," *IET Microw. Antennas Propag.*, vol. 9, no. 8, pp. 822--829, May 2015.

[101] D. Psychogiou, R. Gómez-García, and D. Peroulis, "Fully adaptive multiband bandstop filtering sections and their application to multifunctional components," *IEEE Trans. Microw. Theory Tech.*, vol. 64, no. 12, pp. 4405--4418, Dec 2016.

[102] M. Pal and R. Ghatak, "A distinctive resonance: Multiband bandpass filter design techniques using multimode resonators," *IEEE Microw. Mag.*, vol. 16, no. 11, pp. 36--55, Dec 2015.

[103] H. Miyake, S. Kitazawa, T. Ishizaki, T. Yamada, and Y. Nagatomi, "A miniaturized monolithic dual band filter using ceramic lamination technique for dual mode portable telephones," in *1997 IEEE MTT-S International Microwave Symposium Digest*, vol. 2, June 1997, pp. 789--792 vol.2.

[104] L.-C. Tsai and C.-W. Hsue, "Dual-band bandpass filters using equal-length coupled-serial-shunted lines and z-transform technique," *IEEE Trans. Microw. Theory Tech.*, vol. 52, no. 4, pp. 1111--1117, April 2004.

[105] W. Feng, Y. Zhang, and W. Che, "Tunable dual-band filter and diplexer based on folded open loop ring resonators," *IEEE Trans. Circuits Syst. II*, vol. 64, no. 9, pp. 1047--1051, Sept 2017.

[106] H. Liu, L. Shen, L. Y. Shi, Y. Jiang, X. Guan, and T. Wu, "Dual-mode dual-band bandpass filters design using open-loop slotline resonators," *IET Microw. Antennas Propag.*, vol. 7, no. 12, pp. 1027--1034, Sept 2013.

[107] V. Rathore, S. Awasthi, and A. Biswas, "Design of compact dual-band bandpass filter using frequency transformation and its implementation with split ring resonator dual-band bandpass filter using srr," in *2014 44th European Microwave Conference*, Oct 2014, pp. 949--952.

[108] B. Ren, H. Liu, Z. Ma, M. Ohira, P. Wen, X. Wang, and X. Guan, "Compact dual-band differential bandpass filter using quadruple-mode stepped-impedance square ring loaded resonators," *IEEE Access*, vol. 6, pp. 21 850--21 858, April 2018.

[109] H. Zhu and A. M. Abbosh, "Single- and dual-band bandpass filters using coupled stepped-impedance resonators with embedded coupled-lines," *IEEE Microw. Wireless Compon. Lett.*, vol. 26, no. 9, pp. 675--677, Sept 2016.

[110] W. Jiang, W. Shen, T. Wang, Y. M. Huang, Y. Peng, and G. Wang, "Compact dual-band filter using open/short stub loaded stepped impedance resonators (oslsirs/sslsirs)," *IEEE Microw. Wireless Compon. Lett.*, vol. 26, no. 9, pp. 672--674, Sept 2016.

[111] H. Liu, B. Ren, X. Guan, J. Lei, and S. Li, "Compact dual-band bandpass filter using quadruple-mode square ring loaded resonator (srlr)," *IEEE Microw. Wireless Compon. Lett.*, vol. 23, no. 4, pp. 181--183, April 2013.

[112] H. Y. A. Yim and K. K. M. Cheng, "Novel dual-band planar resonator and admittance inverter for filter design and applications," in *IEEE MTT-S International Microwave Symposium Digest, 2005.*, June 2005, pp. 4 pp.--.

[113] J. Ha and Y. Lee, "Dual-band filter with fully independent passbands based on unequal-length coupled lines and stubs," *IET Microw. Antennas Propag.*, vol. 11, no. 15, pp. 2141--2147, Dec 2017.

[114] C.-W. Tang, S.-F. You, and I.-C. Liu, "Design of a dual-band bandpass filter with low-temperature co-fired ceramic technology," *IEEE Trans. Microw. Theory Tech.*, vol. 54, no. 8, pp. 3327--3332, Aug 2006.

[115] S. Y. Zheng, Z. L. Su, Y. M. Pan, Z. Qamar, and D. Ho, "New dual-/tri-band bandpass filters and diplexer with large frequency ratio," *IEEE Trans. Microw. Theory Tech.*, vol. 66, no. 6, pp. 2978--2992, June 2018.

[116] A. Garcia-Lamperez and M. Salazar-Palma, "Single-Band to Multiband Frequency Transformation for Multiband Filters," *IEEE Trans. Microw. Theory Tech.*, vol. 59, no. 12, pp. 3048--3058, Dec 2011.

[117] D. Guo, K. He, Y. Zhang, and M. Song, "A multiband dual-polarized omnidirectional antenna for indoor wireless communication systems," *IEEE Antennas and Wireless Propagation Letters*, vol. 16, pp. 290--293, 2017.

[118] J. Enomoto, H. Nishizawa, R. Ishikawa, Y. Takayama, and K. Honjo, "Parallel combination of high-efficiency amplifiers with spurious rejection for concurrent multiband operation," in *2016 46th European Microwave Conference (EuMC)*, Oct 2016, pp. 1075--1078.

[119] S. Zhang, L. Qiu, and Q. Chu, "Multiband balanced filters with controllable bandwidths based on slotline coupling feed," *IEEE Microwave and Wireless Components Letters*, vol. 27, no. 11, pp. 974--976, Nov 2017.

[120] D. Psychogiou, R. Gómez-García, and D. Peroulis, "Single and multiband acoustic-wave-lumped-element-resonator (awlr) bandpass filters with reconfigurable transfer function," *IEEE Transactions on Microwave Theory and Techniques*, vol. 64, no. 12, pp. 4394--4404, Dec 2016.

[121] D. Psychogiou, B. Vaughn, R. Gómez-García, and D. Peroulis, "Reconfigurable multiband bandpass filters in evanescent-mode-cavity-resonator technology," *IEEE Microwave and Wireless Components Letters*, vol. 27, no. 3, pp. 248--250, March 2017.

[122] R. Gómez-García, R. Loeches-Sánchez, D. Psychogiou, and D. Peroulis, "Multi-stub-loaded differential-mode planar multiband bandpass filters," *IEEE Transactions on Circuits and Systems II: Express Briefs*, vol. 65, no. 3, pp. 271--275, March 2018.

[123] R. Gómez-García, J. Muñoz-Ferreras, and D. Psychogiou, "Split-type input-reflectionless multiband filters," *IEEE Microwave and Wireless Components Letters*, vol. 28, no. 11, pp. 981--983, Nov 2018.

[124] J. J. Sánchez-Martínez, M. Pérez-Escribano, and E. Márquez-Segura, "Synthesis of dual-band bandpass filters with short-circuited multiconductor transmission lines and shunt open stubs," *IEEE Access*, vol. 7, pp. 24 071--24 081, 2019.

[125] R. Li, S. Sun, and L. Zhu, "Synthesis Design of Ultra-Wideband Bandpass Filters With Composite Series and Shunt Stubs," *IEEE Microw. Wireless Compon. Lett.*, vol. 57, no. 3, pp. 684--692, Mar. 2009.

[126] J.-Y. Li, C.-H. Chi, and C.-Y. Chang, "Synthesis and Design of Generalized Chebyshev Wideband Hybrid Ring Based Bandpass Filters With a Controllable Transmission Zero Pair," *IEEE Trans. Microw. Theory Tech.*, vol. 58, no. 12, pp. 3720--3731, Dec 2010.

[127] R. Zhang and L. Zhu, "Synthesis and Design of Wideband Dual-Band Bandpass Filters With Controllable In-Band Ripple Factor and Dual-Band Isolation," *IEEE Trans. Microw. Theory Tech.*, vol. 61, no. 5, pp. 1820--1828, May 2013.

[128] ------, "Synthesis of Dual-Wideband Bandpass Filters With Source-Load Coupling Network," *IEEE Trans. Microw. Theory Tech.*, vol. 62, no. 3, pp. 441--449, March 2014.

[129] I. C. Hunter, *Theory and Design of Microwave Filters*, Stevenage, Ed. U.K.: IEE Press, 2001.

[130] J. J. Sánchez-Martínez and E. Márquez-Segura, "Analysis of wire-bonded multiconductor transmission line-based phase-shifting sections," *J. Electromagnet. Wave.*, vol. 27, no. 16, pp. 1997--2009, Sep. 2013.

[131] W. Ou, "Design Equations for an Interdigitated Directional Coupler," *IEEE Trans. Microw. Theory Tech.*, vol. 23, no. 2, pp. 253--255, Feb. 1975.

[132] G. L. Mattahei, L. Young, and E. M. T. Jones, *Microwave Filters, Impedance-Matching Networks, and Coupling Structures*, M. A. House, Ed. Norwood, 1985.

[133] R. J. Cameron, "General coupling matrix synthesis methods for Chebyshev filtering functions," *IEEE Trans. Microw. Theory Tech.*, vol. 47, no. 4, pp. 433--442, Apr 1999.

[134] G. Macchiarella and S. Tamiazzo, "Design techniques for dual-passband filters," *IEEE Trans. Microw. Theory Tech.*, vol. 53, no. 11, pp. 3265--3271, Nov 2005.

[135] S. Amari, F. Seyfert, and M. Bekheit, "Theory of Coupled Resonator Microwave Bandpass Filters of Arbitrary Bandwidth," *IEEE Trans. Microw. Theory Tech.*, vol. 58, no. 8, pp. 2188--2203, Aug 2010.

[136] J.-S. Hong and M. J. Lancaster, *Microstrip Filters for RF/Microwave Applications*, K. Chang, Ed. Wiley-Interscience, 2001.

[137] M. Mahmood, S. Hammad, and I. Mahmood, "An efficient algorithm for computing the roots of general quadratic, cubic and quartic equations," *International Journal of Mathematical Education in Science and Technology*, vol. 45, no. 7, pp. 1095--1103, April 2014.

[138] R. N. Bates, "Design of microstrip spur-line band-stop filters," *IEE Journal on Microwaves, Optics and Acoustics*, vol. 1, no. 6, pp. 209--214, November 1977.

[139] M. Kirschning, R. H. Jansen, and N. H. L. Koster, "Accurate model for open end effect of microstrip lines," *Electronics Letters*, vol. 17, no. 3, pp. 123--125, February 1981.

[140] Y. Lo, L. Chen, and K. Lin, "Design of dual-band bandpass filter using stub-loaded resonator with source-load coupling and spur-line at 2.45/5.5 ghz for wlan applications," in *2014 IEEE International Workshop on Electromagnetics (iWEM)*, Aug 2014, pp. 193--194.

[141] H. Zhang, W. Kang, and W. Wu, "Miniaturized dual-band siw filters using e-shaped slotlines with controllable center frequencies," *IEEE Microw. Wireless Compon. Lett.*, vol. 28, no. 4, pp. 311--313, April 2018.

[142] M. Kirschning, R. Jansen, and N. Koster, "Measurement and Computer-Aided Modeling of Microstrip Discontinuities by an Improved Resonator Method," in

IEEE MTT-S International Microwave Symposium Digest, Jun. 1983, pp. 495--497.

[143] P. Ketkuntod, P. Chomtong, S. Meesomklin, and P. Akkaraekthalin, "A multiband bandpass filter using interdigital and step-impedance techniques for 4g, wimax and wlan systems," in *2015 12th International Conference on Electrical Engineering/Electronics, Computer, Telecommunications and Information Technology (ECTI-CON)*, June 2015, pp. 1--4.

[144] "Silver nanoparticle inkjet ink datasheet," https://www.sigmaaldrich.com/ES/es/product/aldrich/900190, 2021.